Dynamics of a Spin 1 Ferromagnetic Condensate

by

Lorraine Elizabeth Sadler

B.S. (University of California, Berkeley) 1999
M.A. (University of California, Berkeley) 2004

A dissertation submitted in partial satisfaction
of the requirements for the degree of

Doctor of Philosophy

in

Physics

in the

GRADUATE DIVISION

of the

UNIVERSITY OF CALIFORNIA, BERKELEY

Committee in charge:

Professor Dan Stamper-Kurn, Chair
Professor Dmitry Budker
Professor Daniel Neumark

Fall 2006

The dissertation of Lorraine Elizabeth Sadler is approved.

Chair Date

Date

Date

University of California, Berkeley

Fall 2006

Dynamics of a Spin 1 Ferromagnetic Condensate

by

Lorraine Elizabeth Sadler

Abstract

Dynamics of a Spin 1 Ferromagnetic Condensate

by

Lorraine Elizabeth Sadler

Doctor of Philosophy in Physics

University of California, Berkeley

Professor Dan Stamper-Kurn, Chair

Bose Einstein condensates in a dilute gas of ^{87}Rb are explored experimentally. Two new imaging methods are developed to directly probe the coherence properties of the gas. First, we develop coherence-enhanced imaging, an *in-situ* technique, which relies on a non-linear optical property, superradiance enhanced absorption, distinguishing between the condensed and non-condensed portion of the gas. With this method, we are able to derive high resolution spatial maps of the condensate number and obtain a spatially resolved measure of the first-order correlation function. With coherence-enhanced imaging we are able to study the spatial development of extended sample superradiance in which inhomogeneous scattering is observed. Second, we develop a method that enables us to measure the magnetization of an F=1 dilute gas through the direct imaging of Larmor precession within the cloud. With this technique, we make high spatial resolution maps of the vector magnetization and observe inhomogeneous ferromagnetic regions separated by unmagne-

tized defects. We also observe polar-core spin vortices, a type of topological defect.

Professor Dan Stamper-Kurn
Dissertation Committee Chair

To Steven

Contents

List of Figures

List of Tables

Acknowledgements

There are many people who I would like to acknowledge and thank for their support during my tenure at Berkeley. Thanks to my advisor, Dan Stamper-Kurn from whom I've learned how to build a successful lab and do good science. Thanks to James Higbie, who was a great lab mate and constantly challenged me. Thanks to the rest of those who worked on E1: Mukund who I wish I got to work closer with as I transitioned out of the lab, Shin who always gave great advice, Ananth who pushed hard on the experiment and always had great nicknames, Veronique who was patient and taught me much, Sabrina who takes over the helm on the project, Jennie who will be the long-term future of the project, and Fabien who mastered much of our imaging software. Thanks to the rest of the members in the lab who were always around to discuss science: Kevin who always appreciated the fresh King-Pin donut, Tom who is a whiz in the lab, Kater who provided the most succulent treats, Curly Dan who put up with me hogging all the chair space, Ed and Ryan who I wish good luck in their soon to be new roles as graduate students, and Tony as he begins to enjoy Berkeley.

I would also like to thank the academic mentors in my life that have helped me get to this point. Thanks to Young-Kee Kim who always believed in me. Thanks to Bob Jacobsen who gave great advice from the time of my undergraduate career to the present. Thanks to Dima Budker for instilling in me much atomic physics knowledge and reading my thesis. Thanks to Dan Neumark for reading my thesis.

As any experimentalist knows, a working machine is hard to build. Both the electronics shop and machine shop deserve much credit for the success of my project. Thanks to John Davis in the e-shop who was so ever patient with his teaching. Thanks to the rest of the e-shop shop crew, for always taking time to answer questions. Thanks to Joseph Kant who taught me how to machine. Thanks to David Murai

for his friendship and welding skills. Thanks to Peter Thuesen for believing in my machining skills.

Thanks to others in the department who have been helpful over the years. Thanks to Anne Takizawa for always lending an ear. Thanks to Donna Sakima for her friendship and candy. Thanks to Claudia Trujillo for being a wonderful person and planning two great graduation ceremonies. Thanks Daniel for cutting through administrative red tape.

Thanks to all my friends who supported me. Thanks to Mia who allowed me to understand more about gender and science. Thanks to Lindley for needed girls nights. Thanks to Nathan for coffee and lunch.

Lastly, but most importantly, I would like to thank my family for their support and love. Thanks to Mom and Dad for making me who I am. Thanks to Kat for being a great sister and pushing me to finish. Thanks to Jason for the many English and math classes we navigated together and being a great brother-in-law. Thanks to Hannah, my new niece, for just being cute. Thanks to my in-laws, Cathy and Bob for being supportive and feeding me during the writing of this document. Thanks to my puppies that have given me much emotional support through graduate school. Finally, thanks to Steven, who has been my rock. I love you!

Chapter 1

Introduction

The interest in ultra-cold atomic physics has exploded over the past decade with the Bose-Einstein condensation of dilute atomic gases. The techniques used to realize a Bose-Einstein condensate (BEC) are now standard tools used by many atomic physicists. However, the scientific questions that can be addressed using a BEC interest a diverse group of scientists from many different subfields of physics. Unique properties of a condensate, which include the macroscopic occupation of a single quantum state, long-range off-diagonal order, and superfluidity, allow for an extensive array of study of new phenomena including matter-wave coherence, vortices, quantum phase transitions, and topological defect formation.

1.1 Bose-Einstein condensation

Bose-Einstein condensates have been realized in many systems including liquids [1, 2], solid-state systems [3, 4, 5], and dilute atomic gases [6, 7]. Regardless of the system in which this state of matter is realized, many similarities and descriptions of these systems exist that solely rely on the macroscopic occupation of a single quantum

state. In the following section, a brief phenomenological description of a BEC will be given sufficient for the understanding of work presented here. For a more in-depth mathematical description of BEC in dilute gases, Dalfovo, *et.al* [8] is a good reference.

Phenomenologically, a BEC is best described initially by examining arise a statistical distribution of identical bosons, a type of particle with integer spin, that are allowed to occupy the same quantum state. These statistics were first predicted by Bose in 1924 [9] regarding photons in black-body radiation and expanded on by Einstein [10] who describe the distribution of N indistinguishable particles. At a given temperature T, the system distributes its particles in the most entropically favorable way by

$$N = \Sigma_i \frac{1}{Exp[(\epsilon_i - \mu)/kT] - 1} \tag{1.1}$$

where the sum ranges over all states i, ϵ_i is the energy of the i state, μ is the chemical potential of the system and k is the Boltzmann constant. The remarkable property of this distribution is that as the temperature drops, the particles preferentially occupy the lowest, ground state energy. For a uniform collection of bosonic particles in a BEC, we can write down a wavefunction for this ground state into which the particles condense

$$\psi(r) = \psi_0 Exp(i\theta(r)) \tag{1.2}$$

where ψ_0 is the amplitude of the BEC and $\theta(r)$ is the spatially varying phase of the system. For most experimental implementations, this simple wavefunction can be generalized to include a spatially varying amplitude $\psi_0(r)$.

1.1.1 Dilute gases

Although a macroscopic occupation of the ground state is present in each system that realizes a BEC, there are many advantages to studying this phenomena in a dilute atomic gas. Most importantly, compared to strongly interacting liquids and solids,

dilute atomic gas systems have weak interatomic interactions allowing the use of perturbation theory in analytical calculations. These perturbative calculations allow for theoretical studies of large systems, which have previously been studied in strongly interacting liquids and solids with numerical methods due to the complexity of the calculation. With simplified calculations, close collaborations between experimentalist and theorists have evolved (for example see [11, 12]) and detailed descriptions of the observed phenomena are presented.

One simple theory in which calculations are done in dilute gas BEC to make predictions is a mean-field approximation. In these calculations we assume that all N particles are condensed into the ground state, at which point we can use a Hartree solution to solve the system's Hamiltonian. This solution is a product of identical single particle states $\phi(\mathbf{r})$

$$\Psi(\mathbf{r}_1 ... \mathbf{r}_N) = \prod_{i=1}^{N} \phi(\mathbf{r}_i). \tag{1.3}$$

At these low energies, we can approximate any interactions between particles as a point interaction, $U_0\delta(r_i - r_j)$ between two atoms. Here, the strength of the interaction is $U_0 = 4\pi\hbar^2 a/m$ where m is the particles mass and a is the s-wave scattering length. The Hamiltonian for these atoms in the mean-field picture is given by

$$H = \sum_{i=1}^{N} \left[\frac{\mathbf{p}_i^2}{2m} + V(\mathbf{r}_i) \right] + U_0 \sum_{i<j} \delta(r_i - r_j) \tag{1.4}$$

where $\mathbf{p}_i$ is the momentum of the particle, $V(\mathbf{r}_i)$ is an arbitrary confining potential specific to the system.

We can determine the minimum distance ξ required to make a change in the condensate, i.e. the healing length. Here, there is a competition between the interaction potential nU_0 and the kinetic energy due to the change. Setting these two energies

equal, we find that

$$\frac{\hbar^2}{2m\xi^2} = nU_0 \tag{1.5}$$

$$\xi = \sqrt{\frac{1}{8\pi na}}$$

We see that ξ is inversely proportional to the square-root of the interaction strength.

The relative size in healing length is important when comparing a strongly interacting system such as liquid helium to a weakly interacting system such as dilute atomic gas. In the dilute system, $\xi \sim 1$ μm, which is optically resolvable compared to that of a liquid $\sim$100 $\mathring{A}$. Besides the ease of analytical calculation, this difference in healing length grants access to experimentalists in dilute systems to spatially resolve variations in the wavefunction.

In order to see these variations in the wavefunctions, it is important to have a variety of imaging and analysis tools available to probe the system. Many of the previous techniques such as expansion imaging, obscure fine spatial features. Therefore, as experimentalist studying these system, we must develop new tools to search for and understand the phenomena inherent in BECs.

1.2 Overview of work

The description of the work done in this document can be broken into two distinct pieces that follow, more or less, the chronology of my time spent in this lab. The first portion of this document will focus directly on the design and construction of an apparatus used to explore, in the second phase of my research, some interesting phenomena in BECs. The initial work for the project began in January 2001 with initial meetings between Dan Stamper-Kurn, James Higbie, and me in which we divided the major responsibilities on the project. My contribution during this initial construction phase was to build an atomic oven to provide a source of atoms that

could be cooled and condensed. Inherent in this project was the design and assembly of a vacuum system capable of reaching pressures around 10^{-11} torr. While this source was being built, I laid out the optics needed to have a flexible imaging system with high spatial resolution. Once the vacuum, source, and imaging systems were built, I fabricated control electronics that allowed for precise timing of the multiple systems needed to cool and trap atoms. Finally, as the achievement of a BEC was close, I spent a significant amount of time reducing electronic noise that was prevalent in the room, which without proper experimental shielding, hampered our final cooling process.

Once we achieved a BEC, the second phase of the project began. During this phase, we characterized the properties of our BEC. From here, we undertook four main projects in our laboratory. In the first project, we developed a new type of non-destructive imaging system that characterized the magnetization of optically trapped gas. For this work, I optimized the machine and took a variety of images to show the effectiveness of the imaging method. The second project that used this apparatus developed another type of imaging that directly measured the coherence of a trapped gas. For this work, I collected the necessary images to show how this imaging method work. I built the analysis tools that were used to analyzed the images. Finally, I did some brief calculations that justified some unexpect anomalies with regards to collective atom-atom scattering that were seen in the data. In the third project, we used the magnetization sensitive imaging to probe a phase transition between a non-magnetic and ferromagnetic ground state in a spinor BEC. For this project, I helped with the initial data collection. From there, I studied the topological defects that were formed when the gas was quenched through the transition. This portion of the analysis included increasing the signal to noise in the data, numerically modeling the appearance of these vortices, and applying a robust search algorithm that identified vortices in the collected data. Finally, the last project that was undertaken during my

tenure in this lab was the development of a spatially-resolved precision magnetometer. For this project, I helped reduce some of the technical noise on the signal along with providing reliable normalization algorithms for post-processing the data.

1.2.1 Outline

The rest of this dissertation will provide more details regarding experiments done in our lab. I will begin in Chapter 2, by describing in detail portions of the experiment that I built giving technical information on systems and products. Next, in Chapter 3, I will discuss different imaging methods that were used to extract information from our system. Then, in Chapter 4, I will discuss the method and results from coherence-enhanced imaging. Finally, in Chapter 5, I will discuss the dynamics of a spinor BEC as it is quenched across a ferromagnetic phase transition.

Chapter 2

Apparatus

In this Chapter, I will give detailed technical information about the experimental apparatus that was built in order to study those endeavors in the proceeding chapters. A brief overview of the entire apparatus will be given along with details on the experimental sequence necessary to reach quantum degeneracy. Finally, portions of the machine that were directly my responsibility to build/maintain will be described. Other parts of the system are describe in the thesis of James Higbie [13].

2.1 Overview of experimental apparatus

For the work described in this document, we choose to the alkali atom rubidium whose natural abundance is 72.2 % ^{85}Rb and 27.8 % ^{87}Rb. Although less abundant naturally, we choose ^{87}Rb (Fig. 2.1) for its advantageous properties such as its positive s-wave scattering length and the availability of diode lasers whose light is resonant with the atomic transitions. In order to study atoms that are quantum degenerate, the temperature of the atomic samples that we use must be cold, $\sim$ 100 nK. At this temperature, bulk rubidium is a solid and has no interesting long-range coherence

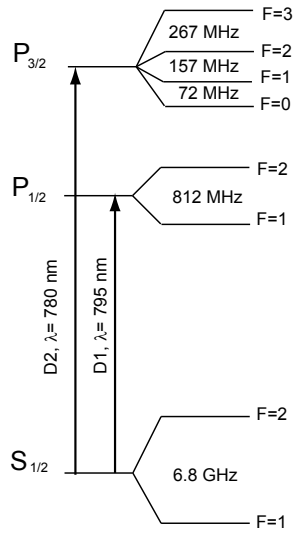

Figure 2.1. D1 and D2 lines for ^{87}Rb.

or macroscopic quantum state occupation. Thus, in order to access the interesting physics of BEC, one must vaporize the solid rubidium to create a dilute gas such that the interactions between atoms are weak and then cool and compress the dilute cloud.

The experimental apparatus needed in order to produce a BEC is comprised of four main parts, a vacuum system in which to execute the experiment, magnetic coils used to trap atoms, lasers used to manipulate and probe the system, and finally computer control needed to run the process. When building the apparatus, it is necessary to consider each part of the system and optimize its performance while considering how this part fits into the overall experiment. The most effective way to describe the overall apparatus is to follow an atom from its source to its condensation (Fig. 2.2).

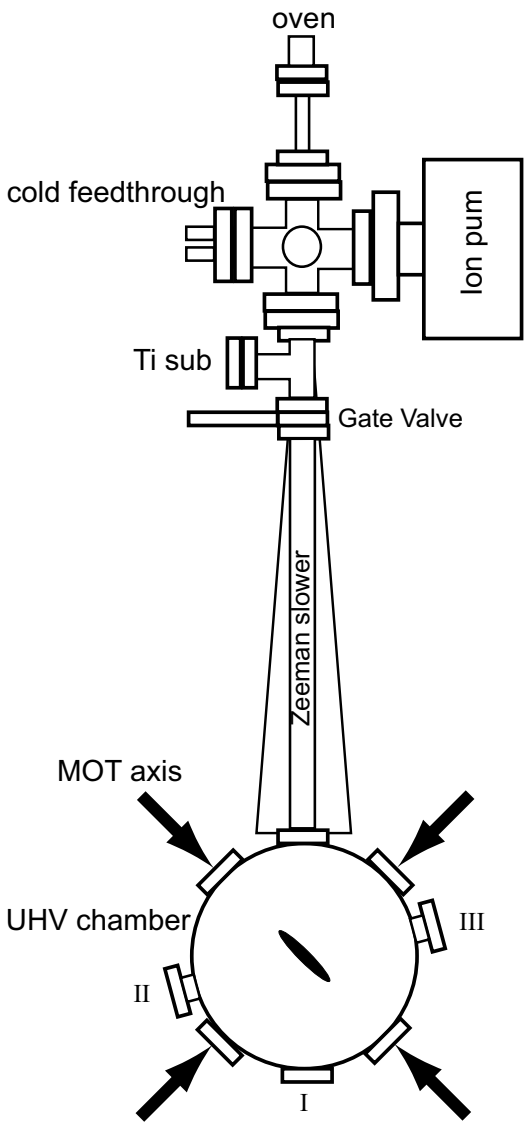

Figure 2.2. Top down diagram of the apparatus. A high temperature atomic beam is produced from an oven. These atoms travel through the Zeeman slower to the UHV chamber. Light used for Zeeman slowing is inserted into the vacuum system through the vacuum port on the UHV system labeled I. Once these atoms are in the UHV chamber they are caught in a MOT. Four of the six MOT laser beams are shown with arrows with the remaining two beams aligned into and out of the page. Once caught in the MOT, the atoms are transferred into a magnetic trap whose fields are created by copper coils located inside of the vacuum system. From here, the atoms are compressed by a cylindrically symmetric trap whose orientation is shown by the cigar shaped ellipse in the center of the UHV chamber and cooled using an forced RF evaporative cooling. One port of the UHV system, labeled II is used as a MOT florescence monitor. This monitor is a photodiode which measures the amount of light atoms in the MOT scatter and is proportional to the number of atoms that are captured by the MOT. Another port of the UHV system, labeled by III, is used as a m=1/3 imaging system (see Sec. 3.2.)

Oven

Our atomic oven (described in detail in Section 2.2) is used to vaporize liquid rubidium and allow for a collimated beam of atoms to be formed. The rubidium is heated in a reservoir to a temperature range between 85 °C and 120 °C whose temperature is chosen such that an adequate flux of atoms reaches the UHV portion of the experiment. In this temperature range, the mean velocity of atoms is $\bar{v} = \sqrt{8k_BT/m\pi} \sim$ 300 m/s.

Zeeman slower

The Zeeman slower for our experiment is used to slow and cool the atomic beam that is emitted from the oven. This apparatus is used to increase the efficiency of loading atoms into a magneto-optical trap (MOT). Typically, MOTs are able to capture atoms that are traveling with a velocity up to $\sim$ 20 m/s, significantly slower than the mean velocity of atoms in the atomic beam. In this first stage of laser cooling, atoms are exposed to light that is counter-propagating, red-detuned with respect to atoms at rest. Since the atoms are moving, the light appears Doppler shifted and is resonant to fast moving atoms at the oven opening. As atoms absorb these photons, they receive a momentum kick opposite in direction in which they are moving resulting in a diminished velocity. This reduction in velocity, which changes the Doppler shift, causes the light to be off resonance, reducing the number of photons that can be absorbed. In order to have efficient slowing and cooling, a magnetic bias field is applied that compensates for the changing Doppler shift through the atomic Zeeman shift.

For our slower, we use a 1.5 meter tube wrapped in square, hollow-core copper tubing. The light that slows the atoms is 520 MHz detuned from the $F = 2 \rightarrow F' = 3$ transition. The laser beam has 20 mW of power and is focused at the oven nozzle.

Simultaneous to the slowing light, we use an 8 mW laser beam that pumps atoms from the $F = 1 \rightarrow F' = 2$, allowing for the $F = 2$ hyperfine ground state to be populated.

MOT

The MOT for our system is created from three sets of one-inch diameter counter-propagating laser beams along orthogonal axes. The light, 20 MHz detuned from the $F = 2 \rightarrow F' = 3$ transition, is derived from a tapered amplifier (for details on the mount and chip see [13]), which produces 270 mW of power after an optical isolator. This light travels through an acoustic-opto modulator (AOM) (Fig. 2.3), which acts as an attenuator and quick switch. From there, it is coupled with $\sim 60\%$ efficiency into a single-mode fiber used to clean up the spatial mode of the beam (for alignment procedures, see appendix 2.3). After the fiber, we have 100 mW to 140 mW of power that is split into six MOT beams with ~ 20 mW each. On four of the MOT beams, we combine re-pump light that places atoms that have been optically pumped into the $F = 1$ ground state back into the $F = 2$ ground state.

The strength of the magnetic field gradients in the MOT is up to 25 G/cm. There are three distinct stages during the MOT process for our experiment, loading, moving the position of the center of the MOT with respect to the magnetic trap, and compressing. The first stage, used for efficient loading of slow atoms from the atomic beam is characterized by full power in each laser beam, 6 mW of power for re-pump light and magnetic field gradients of ~ 15 G/cm, whose exact value is often changed to give the most efficient atom capture. We optimize the MOT loading such that $\sim 6 \times 10^9$ atoms are caught. The position of the MOT, i.e. the zero of the magnetic field, is optimized using external Helmholtz coils that can apply a few Gauss bias field. For the second MOT stage, we decrease the strength of the magnetic field gradients by half for 30 ms during which time we move the MOT with the external

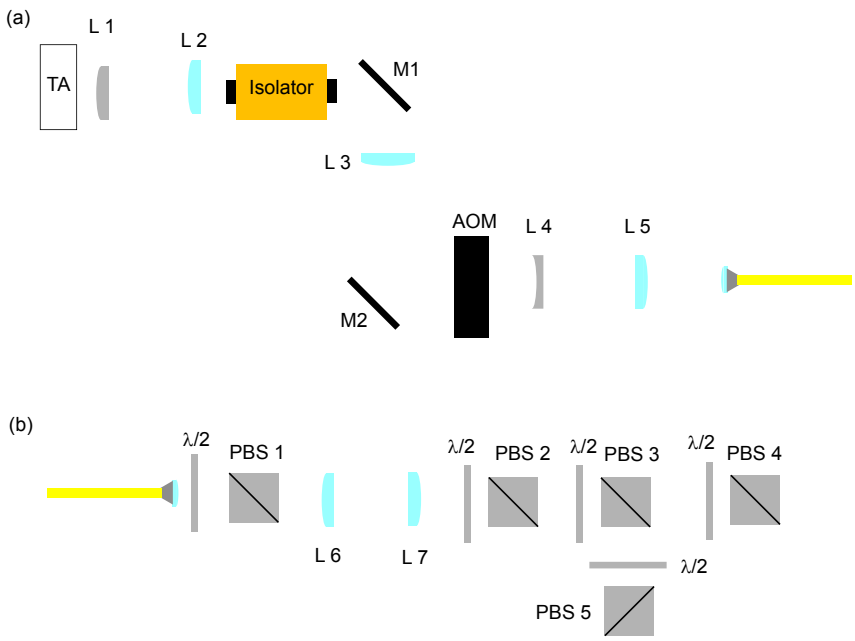

Figure 2.3. Diagram of the taper amplifier optics (a) before coupling into a single mode fiber and (b) being split into the six MOT beams (not to scale). (a) Light travels from the tapered amplifier (TA) through L1 (100 mm cylindrical lens) that corrects the astigmatism of the laser beam. From this point, the light is focused by L2 (200 mm plano-convex lens) with the beam waist coinciding with the optical isolator. L3 (75.6 mm plano-convex lens) is placed to make a small, parallel beam that travels into the AOM. The first order diffracted beam is then coupled into the optical fiber through L4 (-200 mm plano-concave lens) and L5 (300 mm plano-convex lens) which are place to optimize the power through the fiber. Mirrors M1 and M2 adjust the position of the beam through the optics for daily power optimization. The zeroth order beam from the AOM (not shown) is coupled into a Fabry-Perot cavity whose interference signal we use to confirm that the laser light is at the correct frequency. We also use some of the zeroth order light to optically pump atoms into the $|F = 1, m_F = -1\rangle$ state when loading the magnetic trap. (b) After the fiber, polarization of the laser beam is purified (PBS 1) and then expanded by L6 (100 mm plano-convex lens) and L7 (400 mm plano-convex lens). The beam is then broken into 6 MOT beams with PBS 2-5 with each beam's intensity individually controllable with the $\lambda/2$ waveplates place in-front of the splitters.

Helmholtz coils such that the center of the atoms is directly aligned to the center of the magnetic trap. During this stage, we also turn off the Zeeman slower's magnetic field and close the atomic beam shutter. Finally, during the last stage we create a compressed MOT (CMOT) by reducing the the re-pump light to 100 μW such that the MOT compresses into a spherical ball with high densities. Once the atoms are in the CMOT, a 8 ms stage of polarization gradient (PG) cooling [14] is performed. Atoms at this stage have a temperature $T \sim 120\mu$K.

Magnetic traps

Once the atoms have been collected in the UHV chamber by the MOT, they are transferred into a magnetic trap. This experiment uses a Ioffe-Pritchard type magnetic trap [15] whose magnetic fields are created by coils made from copper tubing wrapped in Kapton tape. These coils are bolted inside of the UHV chamber and are connected to vacuum feedthrough that allow both current and chilled water to flow through the coil. Much detail on this trap is given in [13] and will not be further discussed. However, it is good to note, that this trap is flexible and reliable. The magnetic trapping frequency used in these experiments vary from $(\omega_x, \omega_y, \omega_z)$=$2\pi$(10,10,15) Hz, $(\omega_x, \omega_y, \omega_z)$=$2\pi$(120,120,5) Hz and $(\omega_x, \omega_y, \omega_z)$=$2\pi$(48,48,5) Hz.

Evaporative cooling

Once atoms are transferred into the magnetic trap, they are compressed and held in a trap characterized by frequencies $(\omega_x, \omega_y, \omega_z)$=$2\pi$(120,120,5) and cooled using a force radio-frequency (RF) evaporation [16]. In the forced evaporation, atoms are selectively driven from a weak-field seeking, magnetically trapable state, i.e. $|F = 1, m_F = -1\rangle$, to a high-field seeking state that is magnetically untrapable, i.e. $|F =$

$1, m_F = +1\rangle$. Once an atom is transferred to an untrapable state, it is expelled from the trap at which time the sample thermalizes to a new average temperature. If the atom that leaves has a higher average temperature then the rest of ensemble, the average temperature of the sample will decrease. Those atoms that undergo a transition are resonant with the driving RF field at $g\mu_B B = \hbar\omega_{RF}$ where ω_{RF} is the driving frequency, g is the Lande factor and B is the magnetic field that the atom experiences. By setting the RF frequency to correspond to larger magnetic fields, atoms with large temperatures are selectively removed from the trap.

One major background that this apparatus is constantly fighting is spurious RF noise. This noise can affect the efficiency of RF evaporation if it is resonant with the coldest atoms in the trap. Here, the coldest atoms from the trap would be removed, and after thermalization, the average temperature of the sample would increase, driving the sample away from quantum degeneracy. We find many sources of this noise in our laboratory. First, we find that the bias field in the magnetic trap needed to be placed between 2.2-3 MHz (1.5-2 G) because the spurious noise due to the building and laboratory equipment is the least intense. Second, we find that the RF source used for evaporation is important. We attempted to use an Stanford Research Systems (SRS) 30 MHz function generator to produce the RF fields. However, due to the way that the SRS generates frequencies between 10-30 MHz (through mixing and doubling), significant sub-harmonics are present (suppressed by only 20 dB from the carrier). Thus, while using this generator, the atoms receive the appropriate high RF frequency fields, which effectively remove the hottest atoms, but they also feel the effects of low RF frequency fields, which removes the coldest atoms from the sample. This causes the evaporation process to be less efficient and BEC is unattainable with this source. At present we use a 2-GHz function generator from IFR. This generator has no spurious subharmonics.

2.2 Recirculating rubidium oven

An atomic oven is an emissive source of atoms that can be collimated to make a directed atomic beam. This source contains a reservoir that is partially filled with the desired atoms, which is generally either solid or liquid. This material is heated such that an atomic vapor fills the reservoir from which a beam is formed by a collimating aperture.

This type of source is typically inefficient due to the broad output angular distribution of atoms from the oven aperture for which an experiment has a small acceptance angle from the beam source to the target destination. For example, if the collimating aperture at the opening of the reservoir is 5 mm in diameter but the interrogation region (or MOT capture) is 2 m away (as is the case for this apparatus), the acceptance angle θ_c for the experiment is .00125 radians. If we assume that the density distribution of the atoms out of the oven goes as $\cos\theta$, then only those atoms that are in a cone define by θ_c reach the experimental region. For the above example, only only one out of every million atoms that leave the oven actually reaches the experiment. The rest of the atoms are deposited onto the apparatus walls or removed from the system via vacuum pumps.

One way to increase the efficiency of the atomic source is to create an oven that recirculates those atoms that are outside the cone defined by θ_c. The first recirculating ovens [17] used cold plates that surrounded the oven's collimating aperture to which atoms would stick. At pre-defined intervals, these plates were heated to liquify the capture material. This liquid would flow back into the oven and be able to be reused. Although simple, this required the user to remember to re-charge the oven. More user friendly designs [18, 19, 20] were subsequently develop, which relied on a wicking mechanism based on a heat pipe [21]. For this type of recirculator, capillary tubes surround the collimating aperture, which are filled with a liquid atomic source. A

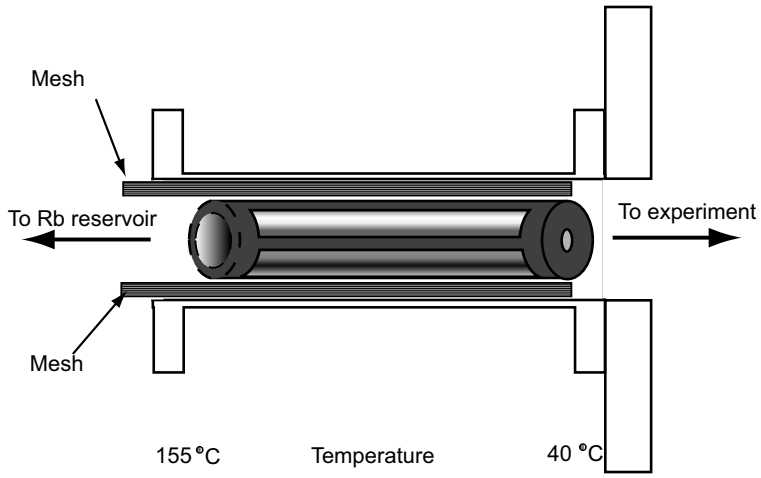

Figure 2.4. Diagram of the oven nozzle. The of the oven is a conflat nipple one inch in diameter. Inside, a stainless steel tube acts as a collimator for the atoms with a 5 mm hole at the far end. The tube, with slots such that the unused rubidium vapor is allowed to hit the stainless steel mesh is kept at a temperature gradient by a large resistive heater wrapped around the outside of the vacuum on the flange closest to the rubidium reservoir.

temperature gradient is established across the tube so that liquid can be wicked from the cold to the hot region and redeposited into the holding reservoir. This wicking occurs due to a resulting force on the liquid caused by the difference in surface tension, which is inversely proportional to the temperature.

2.2.1 Nozzle

At the heart of the oven is the nozzle that acts as the collimating aperture for the reservoir and allows for the recirculation of rubidium. The nozzle, based on a design from the Aspect group [22], is made from three separate parts, the outside vacuum flange, the mesh, and the support tubing (Fig. 2.4). The outside vacuum piece is a custom nipple, three inches in length made from 304 stainless steel. This piece is used to control the heat gradients necessary to cause the wicking of liquid rubidium in the oven. A piece of insulated heating wire is wrapped around the flange closest to the reservoir to create the high-temperature end of the capillary tube. This temperature

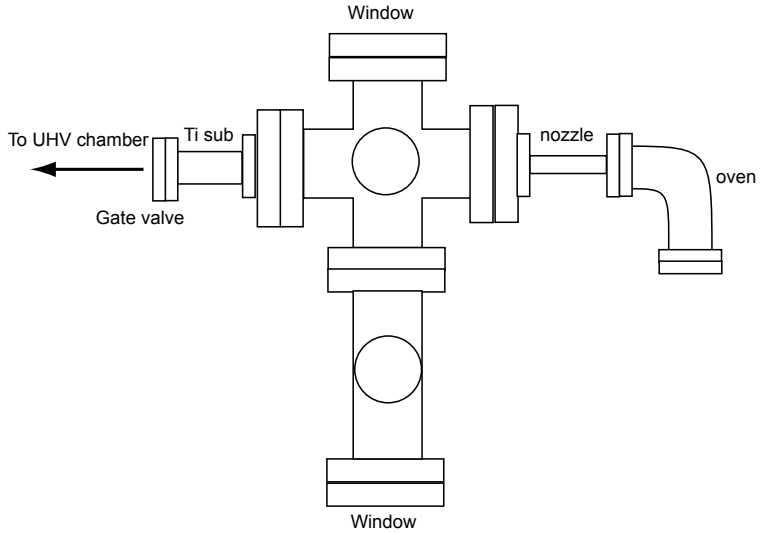

Figure 2.5. Side view diagram of the oven region. The vacuum system is made of stock 4.5 inch and 2 3/4 inch conflat vacuum flanges. The key features of the oven include windows on the top and bottom of the middle chamber to allow for optical access to the atomic beam.

is measured with a thermocouple placed in the sniffer port of the vacuum flange. The measured temperature of the outside of the vacuum is $\sim$ 150 °C, and it is assumed to be the temperature of the hot end of the wick. The cold end of the nozzle is measured to be $\sim$ 40 °C, the melting point of rubidium. This temperature grating is established across the vacuum tube due to the poor conductivity of the stainless steel. The nozzle connects to the rubidium reservoir (Fig. 2.5), which is held between $\sim$ 85 °C and $\sim$ 120 °C depending on the desired atomic flux.

The mesh used in this oven is 250 micron, 316 stainless steel mesh manufactured by TWP (p/n 250X250S0016W48T) consisting of .0016 inch diameter wire with a .0024 inch opening. The mesh is the most crucial part of the oven and can be the most difficult portion to control. As discussed above, the rubidium needs small capillary channels that act as a pipe for the rubidium to flow. The mesh provides this channel for the rubidium. However, through empirical tests, it is not sufficient to place the mesh around the collimating aperture and turn the oven on. This mesh needs to be

wetted such that the capillary tubes are filled with rubidium and thus can act as heat pipes. This wetting is a five hour process, which begins by heating the hot part of the nozzle to 60°C and then, at about 20 °C an hour, increasing both the nozzle and reservoir temperature until the desired running temperature is reached, keeping a difference in temperature of ∼60°C. It was suggested in [19] that covering the mesh with a nickel strike and gold allows for a more complete wetting of the steel due to the formation of an gold-rubidium alloy. However, after trying this coating, we found no significant difference in the oven properties between the gold-coated mesh and the bare, stainless steel mesh.

The support tubing is a piece of 304 stainless steel pipe that was machined to have a 5 mm hole at one end that sets the collimation of the rubidium beam out of the reservoir. The rest of the tube supports the mesh, allows it to be in thermal contact with the vacuum nipple. Slots were cut in the tubing such that rubidium that travels on the inside of the tube can hit the mesh and have access to the wicking channels. Although this design limits the rubidium's access to the mesh, it is an essential part. A previous attempt of this nozzle did not have the support tube allowing the mesh to collapse. This catastrophic failure mode blocked the collimating aperture such that it stopped the rubidium atoms from leaving as a directed source.

2.2.2 Rubidium vapor control

The control of the rubidium vapor and atomic beam is essential in the ultimate attainment of a BEC. The oven chamber connects to the UHV chamber by a tube that is 1.5 meters long and 1 3/8 inch in diameter. This tube provides excellent differential pumping between the two regions allowing us to keep a difference in pressure of ~ 1000 between the regions. Thus, if we require a pressure of 10^{-11} torr in the UHV portion of the chamber we require 10^{-8} torr in the oven region. This region is primarily served

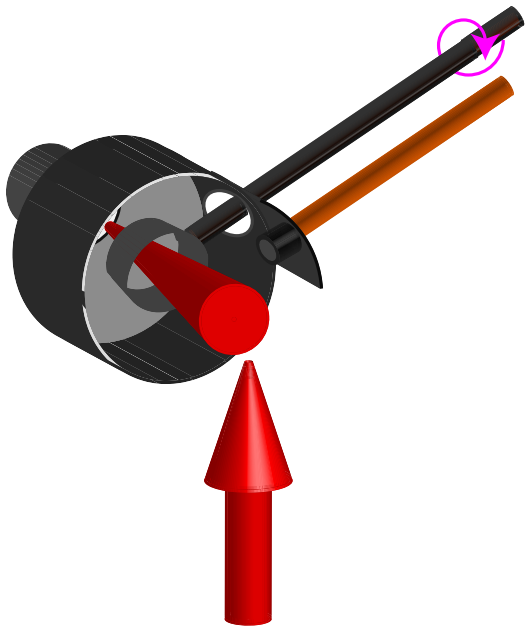

Figure 2.6. Diagram of the oven cold catcher. This integrated system provides rubidium vapor control when cooled below 0 °C by an external TEC. The main piece, made from aluminium, is supported by a cooled copper feed through to which it is in thermal contact. A rotational feedthrough, threaded through the cold catcher allows for the rubidium beam to be blocked during the experiment. At the far end of the system, part of the cold catcher is removed such that optical access for beam diagnostics and slower alignment is available.

by an ion pump. It is known that ion pumps age in the presence of a large load of alkali vapor like our oven. It is thus advantageous to have a second pump for the rubidium such that this ion pump, difficult to refresh or replace, is not destroyed. A cold plate, kept below 0 °C, is sufficient to catch and hold rubidium on its surface and prevent it from moving into the UHV chamber [23].

We installed into the oven chamber a cold catcher, a plate, externally cooled to -18 °C with thermal-electric coolers (TEC) that acts as a pump for the rubidium. The catcher surrounds the atomic beam and is placed directly outside of the nozzle (Fig. 2.6). This cold catcher in the oven provides no collimation for the atomic beam and is placed .25 inch from the end of the nozzle. It is supported by a thin, steel centering ring, which it touches at three points. Even with this small contact, no appreciable thermal contact is noticed. This quarter inch distance between the end of the nozzle and beginning of cold catcher is too small. We designed the cold catcher to be as close to the oven as possible to allow as much rubidium to stick on this portion of the catcher. However, we find that as the oven ages (6-10 months), a bridge of rubidium is built between the end of the cold catcher and the cooler tip of the nozzle. This eventually leads to a plug of rubidium forming in the nozzle hole, clogging the oven and requiring oven replacement. In a redesign, it would be advantageous to at least double this distance. Integrated into this cold catcher is an atomic beam shutter. A slot is cut into this cylinder in which a shutter is inserted. The shutter is composed of a rotatable feedthrough with a 1 inch diameter by .25 inch length tube screwed onto the end. This tube rotates to either allow or block the atomic beams path to the UHV chamber.

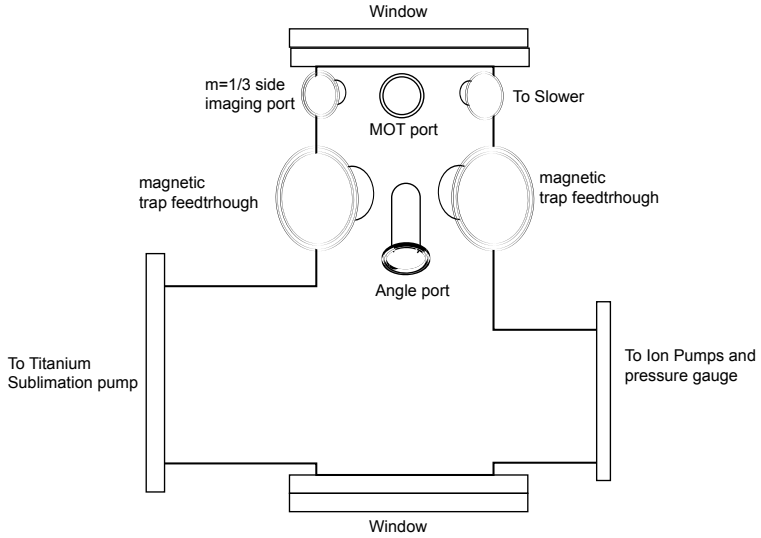

Figure 2.7. Side view of the UHV chamber.

2.3 Ultra-High vacuum system

2.3.1 Design/components

The UHV system is based around a custom designed 316 stainless steel experimental chamber (Fig. 2.7). The material choice of 316 stainless steel was made to reduce excess magnetic fields from being in close proximity to the atoms. The chamber consists of multiple ports fitted with conflat flanges of varying size in order to accommodate optical access, magnetic coil feedthroughs and vacuum pumps. The most unique part of this design are two ports that are cut with a 30° angle to the horizontal such that a diagonal laser beam or viewing axis is allowed for the chamber. The optical access in the system is expansive and different types of windows were mounted onto the chamber while considering optical quality and price. High quality windows, made of optical grade, anti-reflection coated optics are used for each port that a MOT beam enters through i.e. top, bottom, and four side ports. These special windows allow for maximal power transmission and low birefringence important

for the implementation of a MOT. The other optical ports i.e 30° angled ports and slower beam entrance, have regular glass window installed to minimize the cost of the experiment.

The entire vacuum system is mounted using a support system made from 80/20, an aluminum based system of rods and connecters that have varying size and connecters. We cover each piece of aluminum with insulating ceramic fiber strips (McMaster) such that the metal vacuum pieces can be heated for bakeout but the mounting frame and optical table stay relatively cool.

2.3.2 Achievement of pressure

UHV is a time consuming and often frustrating requirement for many different types of experiments. In order to achieve low pressures, it is essential to consider component materials, handling and cleaning, and finally baking and pumping. Once the air is evacuated from the system, the remaining gas in the chamber is the result of material outgassing. Knowing the type and quantity of gas that is released is very useful. There is extensive data on the outgassing of materials [24], which includes materials that are useful for adhesion, electronic components, and structure. In this experiment, we used a variety of material that is usually known for its low outgassing properties including aluminum, 304 and 316 stainless steel, glass, oxygen-free high-conductivity (OFHC) copper, and alumina. We also used teflon, polyimide (Kapton), and torr-seal sparingly.

After choosing materials judiciously, we still need appropriate cleaning and handling procedures for all vacuum pieces. Since organic compounds typically have large outgassing rates, it is essential to keep oils from the human skin and other sources out of the system. Thus, when handling any vacuum part, powder-free latex gloves are used. When it was impossible to keep organic materials off of those parts that

Solution	**Time**	**Ultrasonic Instructions**	**action**
Simple Green + distilled water	1 hour	hot water bath	degreaser
distilled water	1 hour	hot water bath	removes soap
acetone	30 min	cool water bath	removes water
methanol	30 min	cool water bath	removes acetone

Table 2.1. UHV cleaning procedure

will reside in the vacuum system, i.e. machine oil on newly machined parts, a specific cleaning procedure is necessary (see table 2.1). This cleaning procedure has four distinct steps, which follow are typical to vacuum cleaning procedure. The first step in this process differs from many typical cleaning protocals. Although most cleaning begins with a degreaser, we choose to use a solution of Simple Green Clear (McMaster-Carr) diluted 1:1 with distilled water used in a heated ultra-sonic cleaner. This degreaser was chosen over the more traditional degreaser, trichloroethelene because 1) it is non-carcinogenic 2) it is environmentally friendly 3) it can be disposed down the sink with extra dilution and 4) it does not require a fume hood. This substitution has not proved to be detrimental to the achievement of UHV.

Once the system is closed, the vacuum pumps are turned on and the atmospheric air is evacuated from the system. However, the pumps are constantly fighting the outgassing of the materials in the system. In order to assist this process, reducing the amount of gas available to leech from the material is advantageous. Thus, by baking the system, i.e. heating the material to high temperature while pumping out the gas and subsequently cooling the system, the steady-state rate for which gas is released from the surfaces can be substantially reduced. Depending on the type of materials in the system, the temperature of a bakeout can vary dramatically. For a bakeout, the higher the material temperature, the quicker this process takes. The material that one needs to worry about most is stainless steel (either 304 or 316). Here, during

the manufacturing of the steel, hydrogen gas is trapped in the interstitial sites in the material it is slowly released into the vacuum counting from more than 99% of the outgassed material from a cleaned piece [25]. Ideally, a steel vacuum piece would be baked between 350-1500 °C in an external vacuum with pressures less than 10^{-6} torr. The time that the material needs to remain at the high temperature to attain the maximal hydrogen depletion depends on the temperature of the bake i.e. 950°C, need 2 hours. Unfortunately this temperature to time ratio is not linear. It takes approximately an order of magnitude shorter to achieve similar results for every 100 °C higher the material is baked [25]. Also, it is important to note that baking steel above 500 °C may change the magnetic properties of the material and if any of the vacuum flanges are connected, galling of the material is possible lending to a difficult removal.

For this system, the main, UHV chamber was pre-baked at 500°C with each vacuum flange connected. The steel was kept at this high temperature for approximately one week and then cooled. We experienced a significant problem with the galling between flange and cover requiring the removal of flange covers with hammer and chisel. However, due to the high bakeout, once the entire chamber was assembled including windows and magnetic trap, a low-temperature bakeout of approximately one week was all that was needed to attain UHV.

2.4 Experimental control

Due to the complex nature of the experiment, a precise timing mechanism for the machine is essential. The nature of the experiment demands synchronous control of digital switches, analog signals that control multiple valued components, e.g. laser beam intensities and current through the magnetic trap coils, and RF radiation frequency and amplitude. In order to simultaneous direct all equipment, the control

system uses a computer, digital and analog control boards, software, isolation circuits to electrically isolate and protect the computer from the experiment.

The basic hardware that is used to control the apparatus is a Pentium 4 computer processer (Dell) with multiple expansion slots. It is capable of running a GPIB protocol. The digital and analog control boards were bought from National Instruments including PCI-6533 for the digital boards and PCI sb6713 for the analog control. The system contains 32 digital channels (we have the ability to have 64 channels) and 16 analog channels.

2.4.1 Brief description of word generator

The software for the system was graciously given to our group by the Ketterle group at MIT. The original version of this program was written by D. Stamper-Kurn and improved upon after his departure from the group. Although the code for the application is difficult to navigate, minor modifications allowed us to make the software work remarkably well as a control software. The description that follows is a users end guide to the word generator that hopefully shows were some modifications can/have been made to customize the system. It will also illuminate some of the quirks in the timing of the system that the user should acknowledge.

The software contains two panels, one that controls the digital channels and a second that controls the analog and RF output. The digital panel consists of a sequence of words of user specified lengths from 50 μs to 30 s. Unfortunately, if the experiment needs quicker timing than 50 μs, a pulse generator is required to prevent the crash of this software. In each word, 32 digital channels can be specified as being on or off through a user interfaced mouse. For each digital word, an analog and RF sequence can also be specified. The analog panel consists of 16 analog channels whose outputs can be updated every 50 μs and whose input values can be changed with a

linear, sigmoidal, exponential, or step values. Along with the analog output, the RF for the experiment is controlled from this panel. The user has the ability to control the RF with the same types of ramps as in the analog output and individually control the frequency and amplitude. This signal is transmitted using the GPIB protocol to a IFR frequency generator. Due to the slow nature of GPIB, only one change, either frequency or amplitude, can be made every 70 ms. Demanding faster updates of the RF values will create a time lag on the output such that the system will not be in-sync with the rest of the word generator. Also, in order to start a new RF group, the digital word must be at least 70 ms or the computer software will crash.

2.4.2 Digital isolation boards

The digital isolation boards are the conduit for the precise digital TTL signals coming from the computer to the experiment. They are designed in order to protect both the computer and experiment from any electrical spikes that may occur during normal operation if the two are connected. These boards allow TTL signals to control different pieces of equipment in one of two modes: either by the computer or from an external user. The circuit can be seen in figure 2.8 and was produced onto integrated circuit boards that included up to eight digital channels. The boards receive power and transmit their signals over molex connectors.

The main features of this circuit include optical isolation between the computer and the experiment, switching with both manual and computer control, and a 50 ohm line driver. The isolation for these boards are controlled at three main points. First, each active component that connects to the computer receives power from one 15 V power supply whereas active components that connect to the experiment have a separate 15 V supply. Second, the grounds for the two parts are separated with a broken ground plane. Finally, the signal from the computer is passed to the

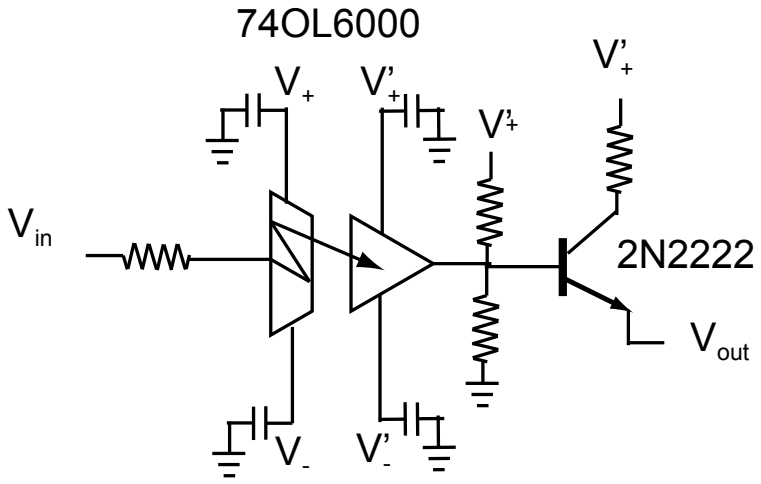

Figure 2.8. Circuit diagram for the digital isolation boards

experimental side by an optical isolator (74OL6000), which, using an optical diode and detector allows for the TTL signal to pass without electrical connection.

The isolation boards were designed to be impedance matched to a BNC cable, which is a 50 ohm component. Without the match, a long cable (used in a cable highway to route signals throughout the lab) causes a large ringing when the signal level is switched, which at best could reduce the level of synchronization of the experiment, and worse, could lead to significant damage to either switches on the components or to the expensive lab equipment. However, when the impedance is matched switching times of less than 1 μs are achieved without ringing. In order to drive a 50 ohm load at 5 V, each line needs to source 100 mA, too much current for a typical integrated circuit chip. Thus, we use a transistor (2N2222) as a line driver that acts as a current source for the line.

2.5 Optical dipole trap

The use of optical dipole forces to manipulate objects is not a new technique nor is it unique to atomic physics. For example, the use of optical tweezers [26] on biological samples have revolutionized many aspects of biology. These optical tweezers are used in a large fraction of the work being done in the biophysics and provides new understanding of forces on such things as DNA and RNA. The optical dipole trap (ODT) has also opened up new physics in the atomic physics community, first realized for a BEC at MIT [27] it has been used to study multi-component condensates [28] and degenerate Fermi gases [29, 30]. Optical dipole forces have also been implemented for optical lattices to further study quantum phase transitions [31] and for quick compression and evaporation of a thermal gas to a BEC [32].

The energy shift of the atom (AC stark shift) arises from the real part of the polarizability and is given by

$$U_{dip}(r,z) = \frac{3\pi c^2}{2\omega_0^3}\left(\frac{\Gamma}{\omega_0-\omega}+\frac{\Gamma}{\omega_0+\omega}\right)I(r,z) = U(\omega_0,\omega)I(r,z) \tag{2.1}$$

where the only spatial variation of the potential comes from the variation in laser intensity. This can be further simplified for small detunings in the rotating wave approximation to be

$$U_{dip}(r,z) = \frac{3\pi c^2}{2\omega_0^3}\left(\frac{\Gamma}{\omega_0-\omega}\right)I(r,z) \tag{2.2}$$

For the simplest ODT, we take a single focused Gaussian laser with beam waist w_0 with an intensity profile

$$I(r,z) = \frac{2P}{\pi w^2(w_0,z)} exp\left[\frac{-2r^2}{w^2(w_0,z)}\right] \tag{2.3}$$

where P is the power in the beam and $w(w_0,z) = w_0\sqrt{1+z/z_R}$ where z_R is the Rayleigh range of the focused beam.

This formula gives a simple expression for the potential of an idealized two-level

atom. However, in order to make calculations on a multi-level atom (such as rubidium) we must take into account the different levels. We can rewrite the energy shift for the two level atom due to the laser light as

$$\Delta E = \pm \frac{|\langle g|\mu|e\rangle|^2}{\omega_0 - \omega} |E|^2 \tag{2.4}$$

where μ is the electric dipole operator that connects the ground g and excited e atomic states and E is the electric field [33]. From this equation, a simple extension is needed to go from the two level atom to a multiple level atom by knowing the diploe matrix operator $\langle e_j|\mu|g_i\rangle$ between all $|g_i\rangle$ ground and $|e_j\rangle$ excited states.

For all work done in an optical trap in our lab, we detuned the laser light such that we can ignore the hyperfine splitting of the atom. Although the light is far detuned compared to the hyperfine structure (Fig. 2.1), the effects of the different transitions due to the fine structure must be considered. The fine structure splits the energy levels in rubidium giving a D-line doublet, i.e. the D1 ($\lambda_{D1} = 795$ nm) and D2 ($\lambda_{D1} = 780$ nm) transitions. We can modify Eq. 2.2 for this multiple level system as

$$U_{dip}(r,z) = \frac{\pi c^2 \Gamma}{2\omega_0^3} \left(\frac{2 + P g_F m_F}{(\omega_0 - \omega)_2} + \frac{1 - P g_F m_F}{(\omega_0 - \omega)_1} \right) I(r,z) \tag{2.5}$$

where $P = 0, \pm 1$ for linearly, circularly polarized light, $(\omega_0 - \omega)_2$ is the detuning of the laser light from the D2 line, and $(\omega_0 - \omega)_1$ is the detuning of the laser light from the D1 line. In order for the trapping potential to be state independent, we choose to work with linearly polarized trap light. Finally, to most easily work with the multiple transitions, we define an averaged wavelength and frequency with each transitions effective contribution $\lambda_{eff} = 1/3\lambda_{D1} + 2/3\lambda_{D2}$ and $\omega_{eff} = 1/3\omega_{D1} + 2/3\omega_{D2}$.

As with most confining potentials, it is important to characterize their trapping frequencies. For small deviations from the center of the trap, we can expand equation 2.1 resulting in a harmonic trap with frequencies $\omega_{x,y} = \sqrt{4U(\omega, \omega_{eff})/(mw_0^2)}$ and $\omega_z = \sqrt{2U(\omega, \omega_{eff})/(mz_R^2)}$.

2.5.1 Elliptical ODT

Although cylindrically symmetric traps are useful and simple to construct, their use with heavy atoms makes them difficult due to the gravitational potential in the $\hat{y}$ direction. Therefore, these traps must be implemented with high trapping frequencies in this direction. However, because of the cylindrical symmetry, this tight confinement enforces high trapping frequencies in the other transverse ($\hat{x}$) direction. Although this is not *a priori* a bad consequence, tight transverse optical confinement of a condensate can lead to large three-body losses and the reduction in the effective dimensionality of the overall gas from three to one. To circumvent this problem, we can form an elliptically focused beam where there is a tight Gaussian focus in the $\hat{y}$ direction but a looser Gaussian focus in the $\hat{x}$ direction. The new intensity profile for the beam is

$$I(x,y,z) = \frac{2P}{\pi w_x(w_{0x},z)w_y(w_{0y},z)} exp\left[\frac{-2x^2}{w_x^2(w_{0x},z)} - \frac{-2y^2}{w_y^2(w_{0y},z)}\right] \tag{2.6}$$

where w_{0x} and w_{0y} are the beam waists in the $(\hat{x},\hat{y})$ directions.

Optical implementation

We implement an ODT using a 825 nm 150 mW free-running diode laser, which we send through a acousto-optic modulator that both stabilizes and changes the intensity of the laser. We then send the laser through a single-mode fiber to clean up the spatial mode of the beam. From here, we shape this cylindrically symmetric beam into an elliptical ODT with an aspect ratio that is appropriate for the current study. The work done for this document (Chapter 5) was done in a trap with a 6:1 aspect ratio . The main features of this implementation of the trap is that both the size and position of the focus of the beam in the $\hat{x}$ and $\hat{y}$ direction can be changed independently.

At the atoms, the ODT has a maximum power of 30 mW with beam waists

of (67,11) μm in the transverse $(\hat{x}, \hat{y})$ directions leading to trap depth of 15 μK at full power. Once we have successfully captured atoms into the trap, we quickly ramp down the power to 2.5 mW leading to measured trapping frequencies of $(\omega_x, \omega_y, \omega_z) = 2\pi(56,350,4.3)$ Hz.

2.5.2 Future prospects: crossed-dipole and 1064 nm traps

Optical traps made from a single focused Gaussian beam have small longitudinal confinement compared to the transverse confinement due to the weak change in beam intensity over the laser's Rayleigh range. This allows the dimensions of gaseous samples to have large asymmetries and can lead to traps that are more one-dimensional in nature. In future studies, it may be advantageous to implement a pancake-like trap that is cylindrically symmetric in the (x,z) plane and has significant confinement in the gravity direction. This can be useful for studying vortices in a trapped gas [34].

One way crate a pancake like trap is by implementing a crossed-dipole trap [33] where two single focus Gaussian laser beams cross at their foci where each come in the horizontal plane. This has two particular advantages, first if the two foci are the same, the symmetry in the system enforces a cylindrical trap and second, due to the geometry of the implementation, the confinement against gravity is twice as strong as a single beam, important for a large mass atom.

Although not implemented in our group at this time, it is possible to make such a cross-dipole trap that is appropriate for work that examines the spontaneous symmetry breaking in a spinor condensate (Chapter 5). The requirements for this trap are that a condensate of $\sim 2 \times 10^6$ atoms is two-dimensional to the spin physics, i.e that the Thomas-Fermi radius in the $\hat{y}$ direction is under 2 μm and that the other dimensions (x,z) are at least ~ 40 μm in dimension.

This is a difficult task to accomplish with one 825 nm 30 mW laser because

this laser would need to be split and the trap depth would decrease significantly. However, we propose to implement this trap with a 1064 nm 20 W fiber laser that will eventually be used for experiments with optical lattices. In order to keep each beam from interfering with the other, the frequency of one beam can be shifted by 10's of MHz. We can calculate the expected trap frequencies of a crossed-dipole trap with elliptical beams in which laser light from laser 1 travels in the $\hat{z}$ direction with intensity at the focus $I_1(0,0,0)$ and beam waists w_1^x and w_1^y and laser light from laser 2 propagates in the $\hat{x}$ direction with intensity at the focus of $I_2(0,0,0)$ and beam waists w_2^z and w_2^y

$$\omega_x = \sqrt{\frac{4U_{dip}(\omega,\omega_{eff})I_1(0,0,0)}{m(w_1^x)^2}} \tag{2.7}$$

$$\omega_z = \sqrt{\frac{4U_{dip}(\omega,\omega_{eff})I_2(0,0,0)}{m(w_2^z)^2}} \tag{2.8}$$

$$\omega_y = \sqrt{\frac{4U_{dip}(\omega,\omega_{eff})I_2(0,0,0)}{m(w_2^y)^2} + \frac{4U_{dip}(\omega,\omega_{eff})I_1(0,0,0)}{m(w_1^y)^2}} \tag{2.9}$$

We can ignore the small contributions to ω_x and ω_z from the weak focus in the direction of propagation. We find that the two-dimensional requirements are met for a trap of two laser beams, each with 1 W of power and beam waists of (100,20). With these lasers, we expect trapping frequencies $(\omega_x,\omega_y,\omega_z)$=$2\pi$(5,168,5) Hz with Thomas-Fermi radii (r_x,r_y,r_z)=(80,2,80) μm.

Chapter 3

Imaging

This chapter describes the variety of ways in which we measure our experimental system through multiple imaging techniques. Some portions of the chapter have been published in

- *J. M. Higbie, L. E. Sadler, S. Inouye, A. P. Chikkatur, S. R. Leslie, K. L. Moore, V. Savalli, and D. M. Stamper-Kurn, Direct non-destructive imaging of magnetization in a spin-1 Bose-Einstein condensate gas, Physical Review Letters 95 050401*

One incredible property of a Bose-Einstein condensate, an object that reaches into the quantum mechanical world, is that it is visible with the eye and comparable to the size of a strand of hair. In order to probe this quantum mechanical object, we illuminate it with light and measure its properties through images taken with a camera. The resulting images are often noisy and significant post-processing and data analysis is necessary to understand many of the phenomena we wish to study.

In this chapter, I will present many details that are often either taken for granted or ignored when imaging a BEC. I will begin this chapter by describing the hardware

involved in imaging, including details about both the lenses and camera. I will then discuss the myriad techniques that we use to extract quantitative information on the system including expansion and *in-situ* imaging. Finally, some of the more tedious portions of noise reduction and image analysis will be described.

3.1 Imaging system and characterization

3.1.1 Pi-Max Camera

The imaging system is made up of three distinct parts, the camera, the optics and the readout software. The camera, made by Princeton Instruments, has a variety of properties that characterize the charge coupled device (CCD) chip, readout, noise and mode of operation. The heart of the camera, the CCD chip is located behind a window, and is cooled to -40 °C by a TEC to reduce the dark current. The chip is kept under rough vacuum to prevent water condensation that could damage the chip when cooled. The CCD chip contains 1024 x 512 pixels, which are 13 μm by 13 μm in size, with half of the pixels in the long direction optically masked from the camera opening. When an image is captured onto the camera, the accumulated charge on the chip can be downloaded to the computer software.

The camera can be used in a variety of ways, each useful for different applications including a free-run focus mode, single frame acquisition mode, and kinetics mode. The free-run focus mode allows the camera to act like a bad video camera. Although this mode displays images in real time, there is a significant lag between movement in real life and recording in the image. This mode is useful when positioning laser beams in precise locations and the user has patience to wait for the lag time. The second acquisition mode, that of a single 512 x 512 pixel still frame is used in most atom cloud diagnostics. At this setting, the camera is used in a typical imaging sequence

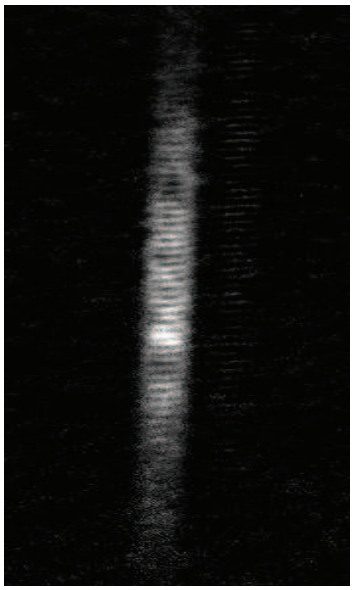

Figure 3.1. Interference effects in an image. A phase contrast image (Sec. 3.2.2) of a BEC in our optical trap. The spatial structure seen in the BEC and the reflective image to the right is due an etalon created by the CCD chip and front window. By coating the front window with an anti-reflective optical coating, the abberation was removed.

containing three data frames. These frames can be processed to make both absorption and phase-contrast images [35]. The third mode of acquisition, kinetics mode [36, 37], solves one particular drawback to most cameras: the inability to image fast system dynamics on the order of tens of microseconds. This task is difficult due to the long download time of the CCD chip onto a computer. The concept of kinetics mode is that the camera is much faster at shifting the charge accumulated in one column of pixels to another column (~ 1 μs/column) than downloading the entire CCD. We can divide the 1024 x 512 pixel chip into smaller regions by providing an optical mask for the entire chip to block the probe light leaving only a enough pixels exposed to view the atoms. Typically this is a 50 x 512 pixel region with magnification of 12.8. Thus, this allows an interrogation of the system every 50 μs acquiring $\sim$20 images in as fast as one millisecond.

The camera we use for this experiment has many advantages including kinetics

mode, low dark count, and low read-out noise. However, we find three main faults with the camera. First, initial images showed large spatial stripes with periodicity of 5 pixels. This obscured most images and was unacceptable to the overall goals of the experiment. We determined that this was caused by interference in the imaging light due to an etalon created by the front window of the camera and the partially reflective CCD chip. (Fig. 3.1). These stripes were significantly reduced by replacing the front window with one that has an anti-reflection coating. Second, we find small amounts of these interference fringes due to an etalon set up within the CCD chip itself. This is a well known problem [38] of silicon devices used with light in the near infra-red. However, the overall effect is small compared to the signal and may be neglected. Finally, we find that the quantum efficiency of the camera at a medium gain setting is only .33, a miserably low number. This is a particular problem for many of our experiments because we necessarily need low light level interrogation of the system. The result of this low efficiency increases the photon shot noise.

3.1.2 Optics

The imaging of the atoms consists of three separate optics systems that have differing magnification, image resolutions, field of view, and modes of use. Described below are the m=1/3 side axis imaging, m=4 MOT axis imaging, and m=1.8 and m=12.8 up/down imaging system. One note: an optics layout is an organic process, which grows and changes with the needs of the experiment. At the time of this document, these were the working imaging systems; however, previous systems have also been used in the course of this work and new ones are sure to be added. I have included those imaging systems who have stayed reasonably stable over more than a year.

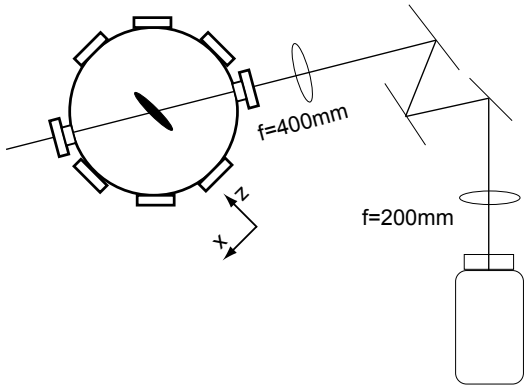

Figure 3.2. M=1/3 side imaging schematic. Top view of the side imaging system at a 60 ° angle to the MOT axis. This imaging setup is threaded through many optics including the MOT and m=4 imaging setup. The second mirror after the first lens is mounted on a kinematic mount such that the camera and last mirror is compatible with the m=4 imaging system. This imaging system is used to optimize the system parameters including CMOT position, magnetic trap loading and efficient early evaporation sequencing. The MOT axis is defined to be the $\hat{z}$ and gravity is in the $\hat{y}$ direction.

Side axis imaging

The side axis imaging system is located at an angle of 60 ° from the MOT axis and images atomic clouds perpendicular to gravity (Fig. 3.2). This system is characterized by a magnification of m=1/3 measured by the acceleration of a cold cloud under gravity once released from a magnetic trap. The field of view is 3/4 inch by one inch and is not limited by the size of the CCD chip but by the size of the imaging aperture, a 2 3/4 inch flange whose clear axis is blocked by trapping coils separated by 3/4 inch. With this expansive view and because this axis is not used as a MOT axis, both the line of sight needed to image and thread a MOT beam into the atoms do not compete allowing for the direct imaging of the CMOT, PG cooling, uncompressed trap, and all stages of the evaporative cooling. When imaging along this axis, one must be aware of the 30° yaw of the atoms with respect to the imaging axis and take this into account when analyzing images. This axis was used to image the first BEC in TOF imaging on January 12, 2004 (Fig. 3.3). The major drawback to this imaging system

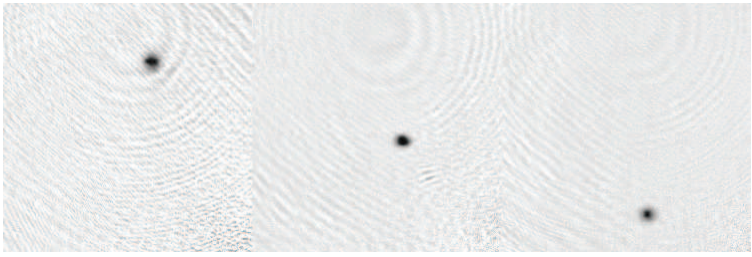

Figure 3.3. First BEC seen from m=1/3 side imaging (1/12/2004). In order to confirm the presence of a degenerate gas, multiple images were taken from the side. In this sequence, the time of expansion is varied and we see at 4 ms that there is a dense center that is elongated in the horizontal direction surrounded by a isotropic wing of gas. As the hold time is increased the at 34 ms the cloud is larger in the vertical direction. Although we were able to confirm the existence of a BEC, it was impossible to measure quantitative properties of this gas.

is the low resolution in the system of $\sim 20\mu$m. Thus, seeing the first BEC *in-situ* was impossible and an expansion method was used with this side imaging system. The second drawback for large, hot clouds imaged in this system is a limitation on the amount of time a cloud can expand before probing because the atoms will fall/expand out of the view of the system. Thus accurate measures on number and temperature for these large systems is less accurate than for smaller clouds.

MOT axis imaging

The MOT axis imaging system is located on the MOT axis and characterized by a magnification m=4 measured similar to the imaging described above. The main purpose of this imaging system is to measure and align the optical dipole trap described in section 2.5. This includes measuring the appropriate beam waists in the $\hat{x}$ and $\hat{y}$ direction and the position of the focus. Thus, a higher resolution system than the m=1/3 system is desirable. This system (Fig. 3.4), is diffraction limited to ~ 6 μm, sufficient to resolve the smallest ODT beam waist of 12 μm. The desire for this system is to image both the BEC at 780 nm and the focus of the ODT at

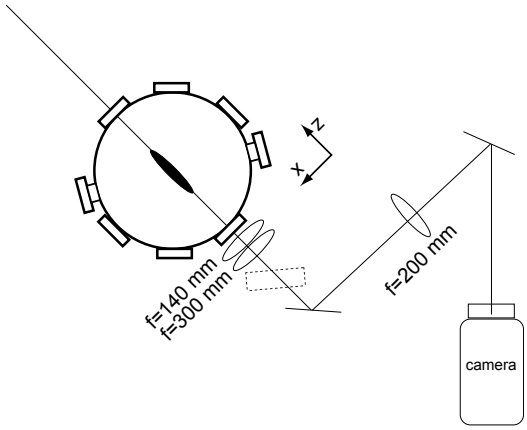

Figure 3.4. M=4 side imaging schematic. Top view of $\hat{z}$ MOT axis imaging system where the atom cloud is measured head on. The lenses in this system are achromatic doublets to allow imaging at both the probe and ODT detuning. The camera is protected by a 780 nm line filter placed directly in front of the shutter to eliminate any intense light from the ODT. The system is focused by changing the one inch translation stage that holds the camera. The dashed box represents a two inch flipper mirror that flips in the MOT beam along that axis.

825 nm. Therefore, it is important to design the system with the smallest amount of chromatic abberation. For normal fused silica, the percent difference in image points for these two wavelengths is $\sim$ 200 μm, about half of the Raleigh range of a laser focused to a beam waist of 12 μm.

This shift can be minimized by using an achromatic doublet, made from two different materials glued together, each having a different chromatic shift that are designed to cancel with one another. It is important to point out that damage to the camera can occur in this imaging system if the ODT light is imaged at full power including taking an *in-situ* optical trap image of atoms. This mistake would allow for over 30 mW of power to be focused onto the CCD camera, burning the chip. To help avoid this we have placed a 780 nm line filter directly in front of the camera, which allows the transmission of light at 780 nm but attenuates by a factor of 10^6 light that is more than ± 2 nm in wavelength from this central value. This reduces the maximum intensity of the focused beam to $\sim$ 1 mW/cm.

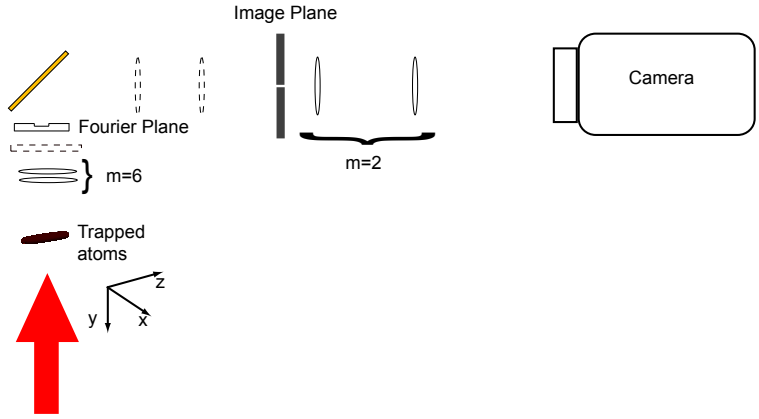

Figure 3.5. Top imaging schematic for both m=12.8 and m=1.8 magnification. The m=12.8 imaging system consists of two separate imaging stages, m=6 stage placed directly on top of the vacuum chamber that focuses the image 750 mm away at the image plane and a m=2 stage before the CCD camera. We place an mask at the intermediate image plane when we use kinetics imaging. We also place a phase plate at the Fourier plane when using the system for phase contrast imaging. Due to geometrical constraints, a bare gold mirror is placed after the phase plate to allow the entire imaging system. For the m=1.8 imaging system the two dashed lenses are place into the system after the mirror and can be easily removed. Finally, the dashed box represents an automated flipper mirror that allows this up/down axis to be both an imaging and MOT axis.

Top imaging

The top imaging system is the main source for analyzed images. We have two magnification settings, m=12.8 and m=1.8 (Fig. 3.5), each having different applications. We will consider first the m=12.8 imaging system. This setting has the highest resolution and is the basis for the top imaging system. This method is only used for *in-situ* imaging either with off-resonant light with Raman absorption or phase-contrast imaging.

This imaging system, unlike the others described makes all measurements along the gravity direction. Thus, only details in the (x,z) plane are visible. For this imaging axis, the light that interrogates the system travels against the gravity direction from the bottom of the chamber to the top. From here, precision optics are placed to gain

the highest resolution possible. In order to achieve this, the first optic in the system is a laser diode doublet with focal length f=140 mm having an f/#=3.5. This is the crucial optic that determines the resolution of the system that leads to a theoretical diffraction limit of 6.6 μm. This lens is placed on a one inch vertical translation stage used to focus the imaging system such that atoms in either the optical or magnetic trap are at the focus of the system. The second optic, placed directly on top of the first when the translation stage is fully extended, is a plano-convex lens with a focal length of 750 nm and with f/#=15. Due to the high f/#, an achromatic lens is unnecessary. The combination of these two lenses leads to an effective focal length of 120 mm. This lens combination has two effects. First, it forms an image of the original system at an image distance of $\sim$ 750 mm from the second lens giving an initial magnification $\sim$ 6. This intermediate image is important in order to optically mask the atom cloud for use in kinetics imaging. Second, it establishes a Fourier plane for unscattered, parallel light at a distance of 120 mm from the lens combination. The difference in length between the Fourier plane and the image plane is important in order to place a phase plate, integral for phase contrast imaging, and a mirror, necessary due to the geometry of the system. To finish this m=12.8 magnification system, we add an m=2 imaging system that re-images the intermediate image onto the CCD camera. This is done with an expanding telescope made of two achromatic lenses with f=140 mm and f=300 mm.

The characterization of this system was done with a test pattern from Edmund Optics (p/n NT58-198) consisting of a variety of dark lines with varying size. This was placed, with some contortions, outside the vacuum system but the identical distance from the first lens as the condensate. By shinning light onto the test pattern, the absorption image is captured onto the CCD, and both the magnification and resolving power of the entire imaging system is determined. A secondary method

using magnetization sensitive imaging confirmed the overall resolution of the system to have a modulation transfer function equal to one-half at 6 μm [13].

The m=1.8 imaging system was designed around the diffraction limited m=12.8 imaging by inserting two lenses before the intermediate focal point. The first lens has a focal length of 100 mm and is closely followed by a lens with focal length 80 mm. We make every effort to mount these lenses such that their height and angle are constrained; however, these lenses are taken in and out of the system repeatedly, and images taken at this magnification have poorer resolution, ~ 20 μm, making this configuration unsuitable for *in-situ* imaging. However, due to the small magnification, this is the ideal imaging system to measure clouds with on-resonant absorption after release from the trap with the only constraint that the cloud can be at most 3.7 mm in diameter. This constraint is met for thermal clouds later in the evaporation system and BECs. This imaging system is used primarily as a diagnostic to determine if the experiment is producing BECs.

3.2 Imaging techniques

The subject of imaging atomic clouds has been extensively written about in many references [39]; however, a brief description will be given here. If we assume that the atomic sample is made up of scatterers with only two levels and that the cloud that we want to image is thin, e.g.. the thin lens approximation is applicable, we can wrap up any microscopic physics into the effective index of refraction given by

$$n_{ref} = 1 + \frac{\sigma_0 n \lambda}{4\pi}\left[\frac{i}{1+\delta^2} - \frac{\delta}{1+\delta^2}\right] \tag{3.1}$$

where σ_0 is the resonant cross-section, n is the density of atoms, λ is the wavelength of the imaging light, and $\delta = \omega - \omega_L/(\Gamma/2)$ is the detuning of the laser with frequency ω_L from resonance frequency ω in half-linewidths $(\Gamma/2)$. This index of refraction

will vary with spatial dependence of the density, and corrections for more than one resonance will need to be reconciled for atoms with more than two levels.

Due to the complex index of refraction, any electric field $\vec{E}$ that travels through the sample has the potential to be both attenuated and shifted in phase. Consider light traveling in the $\hat{y}$ direction through a spatially varying density. The transmitted light and phase shift accumulated by traveling through the system is given by

$$t = Exp\left[-\tilde{D}(x,z)/2\right] \tag{3.2}$$

$$\phi = exp\left[-\delta\tilde{D}(x,z)/2\right] \tag{3.3}$$

where $\tilde{D}(x,z)$ is the off-resonant optical density given by

$$\tilde{D}(x,z) = \frac{\sigma_0}{1+\delta^2}\int n(x,y,z)dy \tag{3.4}$$

This off-resonant density is given here integrated in the $\hat{y}$ direction to give the correct form for up/down imaging. This expression changes in integration direction for either side imaging schemes.

Typical on-resonant optical densities, i.e. $\delta \to 0$, are ~ 400 for our BECs in the trap and ~ 40 for cold thermal clouds. For direct in trap imaging of a BEC, the intensity of light transmitted is on the order of 1×10^{-174}, an absurdly small amount of light to be measured. Thus, in order to actually have a measurable signal, the optical density should be on the order of unity. This can be accomplished by either decreasing the density of the gas through expansion or by increasing the detuning δ for which the optical density would decrease by δ^2.

In the following sections different types of imaging will be discussed, first concentrating on the absorptive, imaginary part of the index of refraction and second, looking at what information can be gained from the real part of the index of refraction, the phase.

3.2.1 Time-of-flight imaging

The first technique we use to interrogate our system is time-of-flight (TOF) imaging, a typically on-resonant absorption image that examines atoms after being released from their trap and expanding for a time τ. TOF imaging is extremely useful to measure number and temperature of hot clouds. However, as the density increases, longer expansion times are needed. For example, the time needed for a condensate's peak density to decrease to the order unity is over 200 ms, after which time the cloud has dropped almost half a meter, well outside the focus of our imaging system. These atoms would also typically slam into the bottom of our vacuum chamber. Thus, as will be discussed in future sections, different imaging tools should be used to characterize a BEC.

Stern-Gerlach analysis

Extracting number and temperatures from images of a gas still does not fully characterize the trapped gas, giving no information on the gas's internal spin state. One way to circumvent this problem is to instigate a Stern-Gerlach analysis in conjunction with the TOF imaging. For a magnetic trap, this is not overly useful because these trap types can only trap the week-field seeking state. However, in an ODT we are able trap all spin states, and this type of analysis is invaluable in diagnosing our manipulation of different spin states.

Different Zeeman sublevels in atoms with total spin F experience different forces due to magnetic field gradients as

$$\vec{F} = \mu_B g_F m_F \nabla \vec{B} \tag{3.5}$$

where μ_B is the Bohr magneton, g_F is the Landé factor, and m_F is the spin projection. We notice that the force is proportional to the spin projection and is signed such that

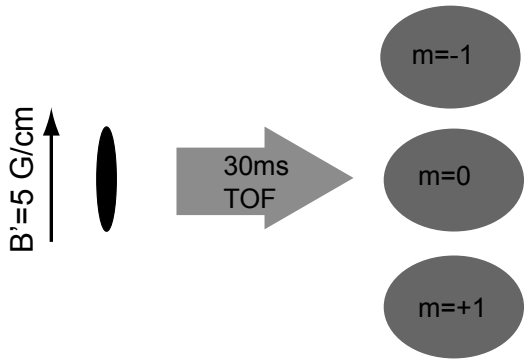

Figure 3.6. Diagram of time-of-flight imaging with a Stern-Gerlach analysis. A magnetic field gradient is pulsed on for 5 ms after a BEC is released from an optical trap. After expansion atoms in each spin projection are separated and each population is a able to be separately measured.

atoms with negative projections experience a force opposite to those with positive projections. Thus, for our work with F=1 atoms, an unpolarized sample will split into three clouds in a significant gradient and appropriate expansion time (Fig. 3.6). Our implementation of this technique is done using our MOT coils. After releasing the atoms for 2 ms to reduce the density of the cloud and minimize collisions, we pulse on a 5 G/cm field for $\sim$ 5 ms and continue to let the atoms expand before imaging. During the separation pulse, the atoms experience a couple hundred milligauss bias field in order to avoid spin flips due to the applied gradient.

3.2.2 *In-situ* imaging

In-situ imaging is a powerful tool that allows for the direct study of the atoms in the trap and enabling the imaging of atoms multiple times many milliseconds apart without having the atoms expand and fall out of view. This allows for the study of the dynamics of atoms in a trap [36, 37]. Due to the high density of atoms in the trap, absorption imaging is an inappropriate probing technique. Spatial structure would be obscured due to the high optical density. Thus, in order to have in-trap imaging,

these atoms must be probed using off-resonant light. However, a detuned laser gains a phase shift ϕ proportional to the detuning when interacting with a gas (Eq. 3.3) causing small objects, like a BEC in a trap, to act as a lens. The imaging light is refracted off the system causing significant imaging abberations. With a judicious choice of laser frequency or the manipulation of the phase shift, powerful imaging techniques emerge. In the following sections, two techniques for *in-situ* imaging will be discussed along with some of their practical applications.

Dispersion-free off-resonant imaging

Off-resonant absorption imaging would be a useful tool if the dispersive effects that obscure small dense objects could be eliminated. In order for this to happen, the total phase shift ϕ of the light would need to be zero. With the correct choice of both laser light polarization and detuning, the total phase shift can be zero. A simple example of the elimination of the phase shift occurs on the D1 line in Rubidium. Let us assume that we have atoms in an $|F = 1, m_F = -1\rangle$ state oriented along a magnetic bias field, which points in the $\hat{z}$ direction. We illuminate these atoms with light on the D1 transition with π polarization, detuned δ, in MHz from the $F = 1 \rightarrow F' = 1$ transition. In order to calculate the total phase shift, we must consider transitions to both the $F' = 1$ and $F' = 2$ excited states, separated by 812 MHz (Fig. 2.1)

$$\phi = \phi_{1\rightarrow 1} + \phi_{1\rightarrow 2} = \frac{OD_{1\rightarrow 1}}{\delta} + \frac{OD_{1\rightarrow 2}}{\delta - 812} = 0 \tag{3.6}$$

where $OD_{1\rightarrow 1}$= $1/24 \times OD_{2\rightarrow 3}$, which is the weighted on-resonant optical density for the $F = 1 \rightarrow F' = 1$ transitions and $OD_{1\rightarrow 2}$ $7/24 \times OD_{2\rightarrow 3}$, which is the weighted on-resonant optical density for the $F = 1 \rightarrow F' = 2$ transitions. Thus, at $\delta = 102$ MHz, these two phases are exactly equal and opposite setting the total phase shift to zero. The overall absorption at this detuning is about 2% for a BEC in the trap, too small to be useful for linear scattering [40].

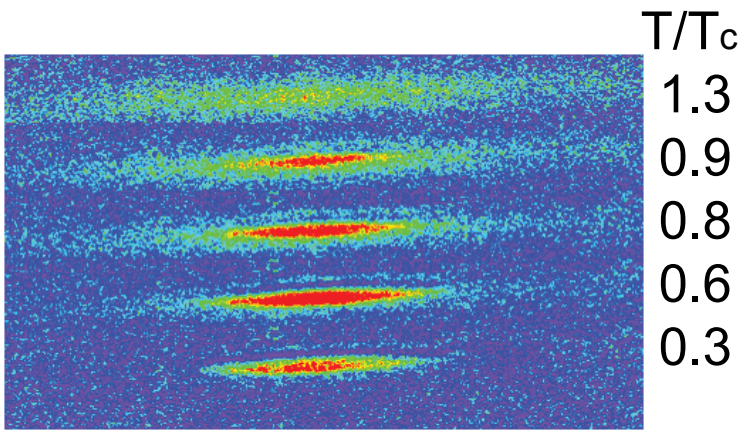

Figure 3.7. Dispersive free imaging with light on the D2 line. Off-resonance images are shown as a function of T/T_c with light detuned $\delta = 150$ MHz from the $F = 1 \rightarrow F' = 0$ state. At this detuning, for a dense, pure condensate, the effective optical density is ~ 1 allowing for complete spatial resolution of the gas *in-situ*.

However, this dispersion free point is not unique to the D1 line of rubidium. There also exist detunings on the D2 line in rubidium where the phase shift cancels, which occur at 150 MHz and 29.2 MHz above the D2 F=1$\rightarrow F'$=0 transition. We choose to use the 150 MHz detuning due to the ease of obtaining the correct frequency of light on our optics table. This method leads to a peak optical density of the BEC of ~ 1 (Fig. 3.7).

Magnetization sensitive phase contrast imaging

The dispersive free linear absorption is a powerful tool that can be used for *in-situ* imaging but, due to the large number of photons scattered, it is destructive in nature by both heating and transferring atoms into magnetically untrapable states. Thus, any hope for repeat images to determine the dynamics of the gas are difficult with this off-resonant absorption imaging. In order to take many images without destroying the sample, it is necessary to go vary far off-resonance to reduce the absorption. At the same time, this also reduces the signal and increases the phase of the scattered light.

Thus, it would be advantageous to image the phase of the scattered light with the camera. This is accomplished in phase-contrast imaging [41], a homodyne detection method in which scattered light is beat against phase shifted unscattered probe light leading to a camera signal that is proportional to the imparted phase shift.

We choose to implement a phase contrast imaging method with the placement of a plate at the Fourier plane of the imaging system that retards or advances the unscattered light by a phase of $\pi/2$ but leaves the light that interacts with the atoms unchanged. Here, unscattered light with the same $\vec{k}$ is focused to a diffraction limited point whereas the position of the scattered light varies with varying $\vec{k}$. The retardation plate is an optical flat with a small circle of excess material placed at the position of the unscattered light's focus that retards the phase by $\pi/2$ relative to the scattered light. Our plate, a 2 inch optical flat made of fused silica was made by Reynard where the center 100 μm has material missing such that the unscattered light is advance by $3\pi/2$. Making a plate with missing material (dimple) in the center was easier for the vendor to fabricate than making a plate with excess material (dot). When choosing the size of the dimple, one must take into consideration the ease of alignment and the distortion to the image. First, if the phase dimple is too small, it is impossible to align, thus 100μm is about the smallest realistic phase dot one would want to incorporate. Second, it is important to realize that the phase plate acts as a spatial filter for the image. A dimple of size D will shift not only the unscattered light by $\pi/2$ but any scattered light that passes through the spot, distorting the image that has characteristic size greater than $d = 2F\lambda/D$ where F is the focal length of the lens. For D=100 μm, this corresponds to d=1.5 mm, i.e. any feature large than 1.5 mm will be unresolved. However, considering the condensate itself is only 300 μm, this is not an issue.

Moreover, phase contrast imaging can be adapted to characterize atoms in multiple spin states by using the bi-refringent interactions of polarized light with the gas

[42]. Consider a collection of atoms in a gas with spin F=1. We probe the system on the D1 transition with σ^+ light. The phase-shift of the interacting light will be

$$1/4\tilde{n}\sigma_0(\Gamma/(2\delta))(1 + 5/6\langle F_y\rangle + 1/6\langle F_y^2\rangle) \tag{3.7}$$

where $\tilde{n}$ is the column density, and F_y is the unitless projection of the spin along the $\hat{y}$ imaging axis. Thus, the birefringent strength of the signal depends on the alignment and sublevel of the atomic spin. The majority of the phase-contrast signal is given by $\langle F_y\rangle$, which gives the magnetization of the sample. The $\langle F_y^2\rangle$ portion of the gas is small and will be neglected, but ultimately gives the "nematicity", which one can extract to fully characterize the density matrix of an atomic ensemble [43].

This type of imaging is extremely useful in characterizing the wave-function of a multicomponent gas. By manipulating the direction of the magnetic field in relation to the imaging axis, this polarization sensitive imaging can be used in two distinct ways. The first method allows the extraction of the atomic population in each magnetic sublevel by the measurement of the longitudinal magnetization. This gives the same information that can be derived from a Stern-Gerlach analysis, but it is non-destructive in nature. For these images, a magnetic bias field in turned on pointing in the direction of the imaging axis. The Clebsch-Gordon coefficients for atoms in the $|F = 1, m_F = -1\rangle$ state is 1/6 as strong as atoms in the $|F = 1, m_F = +1\rangle$ state. Thus the signal will vary by a factor of six depending on the longitudinal component of the magnetization (Fig. 3.8).

The second type of imaging allows for the quantification of the transverse magnetization in the system, which gives the $\Delta m = 1$ coherences in the system. Here, a weak magnetic bias field, B is pointed transverse to the imaging axis. Atoms, initially aligned to this bias field in the $|F = 1, m_F = 1\rangle$ are exposed to a $\pi/2$ pulse effectively tilting the orientation of their spins perpendicular to the bias field. Like any magnet, these atoms will precess with Larmor frequency $\omega_L = 1/2\mu_B|B|/\hbar$. If we consider

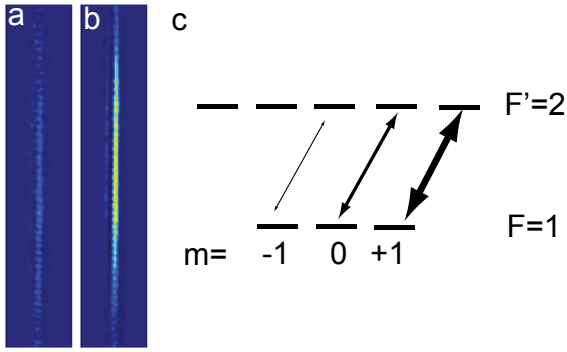

Figure 3.8. Longitudinal imaging of a BEC. (a) Phase contrast image of atoms in the $|F = 1, m_F = -1\rangle$ state with σ^+ light. (b) Phase contrast image of atoms in the $|F = 1, m_F = -1\rangle$ state with σ^-light. (c) The strength of the transitions for F=1 to F'=2 atoms for σ^+ polarized light. Here, atoms in the $|F = 1, m_F = +1\rangle$ state have a transition six times stronger than atoms in the $|F = 1, m_F = -1\rangle$ state whereas these transition strengths are reversed for imaging with σ^- light.

the quantization axis the imaging axis, as the atoms precess, their effective spin state changes from the $|m_F = +1\rangle$ to the $|m_F = -1\rangle$ state. Thus if we use the kinetic mode of the camera, we can interrogate the dynamics of the system with short pulses of σ^+ light. Atoms in the $|m_F = +1\rangle$ state will have a maximal interaction giving a large phase shift and atoms in the $|m_F = -1\rangle$ will have a minimal interaction. If the precessing cloud is sampled quickly (or aliased), an oscillation in the phase-contrast signal is seen (Fig. 3.9). From these images, we can extract the amplitude A and phase ϕ of Larmor precession, which can reconstruct the full transverse magnetization. Finally it is worth noting that atoms in the $|m_F = 0\rangle$ state show no precession signal.

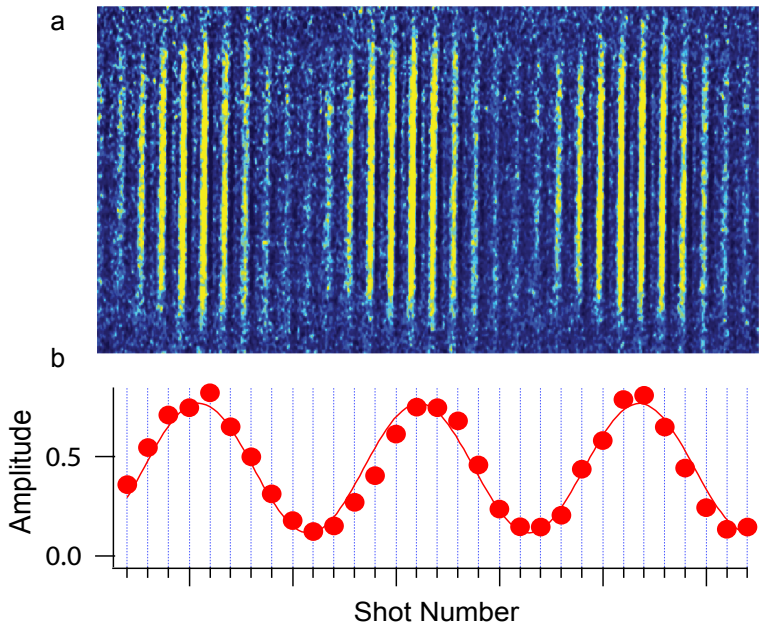

Figure 3.9. Direct, non-destructive imaging of the transverse magnetization

3.3 Image analysis

The projects described in the upcoming sections used extensive image analysis in order to extract quantitative information about different physical systems. The typical analysis for a kinetics mode image required a fit of each pixel in the system to either extract the amount of off-resonant absorption per pixel per kinetics frame (Chapter. 4) or the amplitude and phase of each pixel of Larmor precession (Chapter. 5). These two analysis had low-light level signals and shared some similar noise reduction measures. Some of the more useful measures are described below.

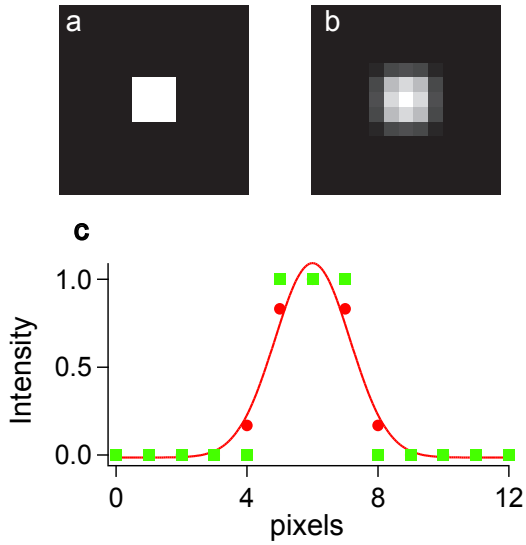

Figure 3.10. Gaussian blur in Igor of 3 pixels. A 3x3 perfect square (a) models a sample pixel in an image with sharp edges. This image is blurred using the convolution imaging panel in Igor with 3 pixels (b). A cross-section of each is shown (c) with the unblurred (green squares) and blurred (red circles) shown. The red line is a fit to the blurred data giving a width of 1.6 pixels. Notice that the amplitude of the fit is slightly greater than the true intensity of the pixels.

3.3.1 Gaussian blur

The first noise reduction technique that we use is a Gaussian blur; i.e. convolving a Gaussian kernel at each image pixel. This ends up blurring each pixel and a loss of information occurs for a perfect imaging system (Fig. 3.10). However, our imaging system is diffraction limited to $\sim$ 6 μm which at m=12.8 is about 6 pixels. Thus we over-sample our system and smearing signal at this level does not damage the collected information.

3.3.2 Bright-field noise reduction

The second major noise reduction that we use to improve our image quality is to average multiple bright field images. The bright field image is the second image taken in which no atoms are present. The purpose of the bright field is to show

the light intensity at each pixel on the camera. Due to the low light levels for our non-destructive imaging techniques, one major source of noise in the image is photon shot noise. This is a dominant noise source when 1) the number of atoms imaged at each pixel is more than the number of photons recorded at each pixel and 2) when the technical noise in the image is small. First, for our system, assuming a constant density of atoms in the condensate to be $n = 2 \times 10^{14}$ cm-1, each pixel images $\sim$ 5000 atoms. However, only $\sim$ 800 photons illuminate each pixel. Thus, the statistical fluctuations in the photons dominates the statistical fluctuations in the atoms. Second, we can define technical noise in our images as noise introduced due to imperfections in the imaging. Here that would include variations in the probe beam across the image and relative movement of the probe beam between images due to air currents or vibrations on the camera or table.

Assuming that the photon shot noise is the dominant source, we average four bright fields closest to one another in time. For example, for experimental run two, we average the bright fields from experimental run one, two, three, and four. From this bright field average, we expect a $\sqrt{2}$ reduction in the shot noise in the absorption image. We find a 20-30 % reduction in noise for the absorption image. We do not meet the expected noise reduction because we are not only shot noise limited. The technical noise after a few averages does dominate the system. In future studies, one way we can decrease this technical noise is by eliminating the air currents that move the laser light by enclosing the beam path. We can also try to damp out vibrations on the table that may move the camera.

Chapter 4

Coherence-enhanced imaging

This chapter discusses a non-linear property of coherent systems, superradiance and its applications for coherence-enhanced imaging. This work was published in:

- *L. E. Sadler, J. M. Higbie, S. R. Lisle, M. Ventilators, and D. M. Stamper-Kurd, Coherence-enhanced imaging of a degenerate Bosie gas, contd-mat/0609007 [submitted to Phys. Rev. Lett., Aug 2006]*

Since the realization of degenerate gases, ultra-cold atoms have been used to model more complex condensed-matter systems and study the long-range off-diagonal order inherent in the systems. Along with the novel engineering of increasingly complex systems, ultra-cold gases are able to access systems far from equilibrium and study the dynamics of the system. These studies could lead to new understanding of spontaneous symmetry breaking occurring while a system traverses either a quantum or thermal phase transition [44, 45, 46].

The popularity of cold atom systems for studies of these complex systems is due in part to the simplicity found in the interactions, thus leading to accessible modeling. However, even with simplified theoretical models, experimental signatures of the

interesting phenomena that would appear in these systems, such as coherence, can be difficult to access and measure. In previous studies where ultra-cold gases were used to study coherence and superfluidity, the scope of exploration has been limited due to existing measurement techniques.

This chapter presents a novel imaging technique, coherence-enhanced imaging, which probes those portions of a gas that display long-range off-diagonal order. This chapter is separated into two main sections. The first section 4.1, I describe superradiance, the seminal tool that enables this new method. The second section 4.2, I describe the experiment that was performed and results that were obtained in our laboratory.

4.1 Superradiance

4.1.1 Rayleigh superradiance

To understand the new imaging method of coherence-enhanced imaging, superradiance, the tool that probes the coherent portion of the gas, needs to be understood. This process, originally describe by Dicke in 1954 [47], has been studied and observed for many years in a variety of systems including solid crystals [48], plasmas [49], and gases [50]. The general experimental setup for superradiant experiments is as follows. Off-resonant light illuminates a sample, pumping all scatterers to an excited state. From here, the excited scatterers optically decay back to the ground state emitting highly directional photons. The experimental signature for these processes is this directed emission, detected on a photodetector. Recently, with the advent of laser-cooling of atoms below the recoil velocity of the system, an additional signature of superradiance has been seen, namely studying the directed atoms recoiling from the initial sample opposite the emitted light [51].

Collective scattering, is most easily understood from the point of Rayleigh superradiance in a gas. In this system, incident, off-resonance laser light pump all atoms to an excited state, in which they receive a momentum kick, $\hbar\mathbf{q} = \hbar\mathbf{k}_i - \hbar\mathbf{k}_s$, which is the difference between the incident $\mathbf{k}_i$ and scattered $\mathbf{k}_s$ photons when they decay back to their original internal state. Due to spatial coherence in the sample, the recoiling atoms interfere with those atoms that are stationary, leading to a periodic density grating. This grating acts as a partial mirror, reflecting incident photons to create the highly directed emission. The amount of reflectivity is proportional to the depth of the grating, i.e. the local density in the recoiling and stationary atoms.

This process can be modeled mathematically by the set of coupled equations

$$\begin{aligned} \dot{N}_c &= -gN_c(N_j + 1) \\ \dot{N}_j &= (g - L)N_c(N_j + 1) \end{aligned} \tag{4.1}$$

where N_c is the number of stationary atoms, N_j is the number of atoms in the j recoiling state, L is the loss and g is the gain in the system. The gain in this system is only dependent on the single particle properties combined with the geometry of the system and is given by $g = R_j f_j A_\Omega$. Here, R_j is the linear scattering rate to final state j, $f_j = sin^2\theta_j/(8\pi/3)$ is the single atom dipole emission, and $A_\Omega = \int d\Omega' |\int d^3\vec{r}\rho(\vec{r})exp[i(k_i - q)\cdot\vec{r}]|^2$, is a phase matching integral giving the overlap between initial and final state. In an extended sample, the maximal gain occurs when light is emitted in a mode along one of the long axes of the gas, or the end-fire mode (EFM). Ignoring the loss in the system, we solve the coupled equations 4.1 and find the occupation rate of the recoiling modes as a function of time is

$$N_j = \frac{1 + N_0 Exp[gt + gN_0 t]}{Exp[gt + GN_0 t] - 1} \tag{4.2}$$

where N_0 is the total number of atoms in the BEC. We note at short times, when

$N_j \ll N_c$, the system has an exponential rise in the scattering rate to state j, which dominates the dynamics of the system. However, due to the finite number of atoms, this growth is damped and declines when the sample is depleted. The maximal scattering rate occurs when half the atoms have scattered. Previous studies of Rayleigh superradiance [51] have measured the gain of the system along with studying the light emitted from the EFM and produced beautiful images of single and multiple scattering superradiance.

4.1.2 Loss Mechanism

In the above discussion, we ignored all sources of loss to the system except sample depletion that occurs when atoms are transferred into the moving state. However, the strength of the superradiant scattering depends on the competition between the stimulated emission into the EFMs and any position-dependent loss that degrades the quality of the grating. Loss from the system can be caused by many phenomena including Doppler dephasing and collisional loss. Here we concentrate solely on the Doppler dephasing leaving discussions of collisional loss for later (Sec. 4.2.4. The grating, a property of interference between coherent atoms, will lose its reflectivity and decay when the recoiling atoms travel farther than their coherence length, λ. The time it takes for this to happen is $\tau_c \sim (q\Delta v)^{-1}$ with Δv being the local atomic rms velocity. As a result, gratings in samples with long coherence lengths such as BECs last much longer than in thermal samples where the coherence length is temperature (T) dependent $\lambda_{dB} = \sqrt{2\pi\hbar^2/mk_BT}$.

4.1.3 Raman superradiance

Raman superradiance is a natural extension of the previous theoretical model that describes Rayleigh superradiance. These two processes are identical except that the

final internal state to which atoms scatter is different than the initial internal state. The consequence of this difference is that a *polarization* grating instead of a density grating is formed in the gas when the recoiling and stationary atoms interfere. Also, depending on the preferred final state of the atoms, multiple scattering events by a single atom (available in Rayleigh superradiance) is energetically unfavorable due to large hyperfine splitting. Previous studies of Raman superradiance [52, 53, 54] have studied this process with detailed studies on the gain in the system and have applied it to a matter-wave amplifier.

4.1.4 Multiple pulse superradiance

As described in the previous sections, coherent matter scatters light uniquely. With a single pulse of light that illuminates the sample, the non-linear interactions can be studied including the gain of the system. However, in order to directly probe the coherence of a sample, a multi-pulse pump/probe experiment is advantageous. This probe method (Fig. 4.1), illuminates the sample with short, weak light pulses separated by a delay time, τ such that any collective scattering in the system is built over more than one pulse. This method provides a direct measurement of the first-order spatial correlation function. Atoms, transferred into one of the recoiling modes propagate in the dark during the delay. The subsequent pulse of light interrogates the quality of the grating, a measure of the interference between the particles two wavefunctions at $\vec{r}$ and $\delta\vec{r} = \hbar\vec{q}\tau/m$ or more specifically $< \Psi^*(\vec{r})\Psi(\vec{r} + \delta\vec{r}) >$. This method can be used to map out the correlations over all $\vec{r}$ by varying τ and ultimately probe the off-diagonal long-range order in the system. Similar to other measures of a first-order correlation function, a reduction in the "visibility" in interference indicates a reduction in the coherence between the two interfering points. For superradiance, this corresponds to a reduction in the amount of collective scattering. Many previous

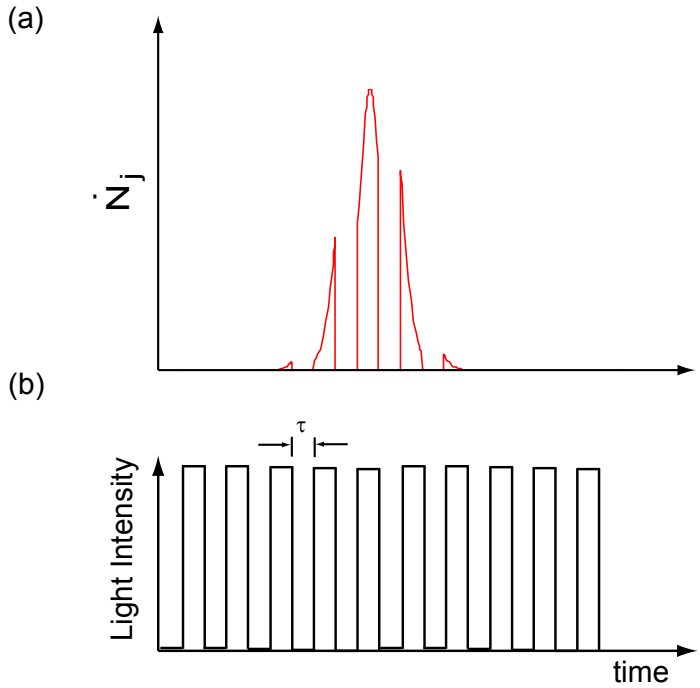

Figure 4.1. Multiple pulse superradiant experiments where (a) gives the theoretical scattering rate integrated over the entire sample for atoms exposed to light pulses seen in (b). During the initial pulses, separated by time τ, collective scattering, occurring in the coherent portion of the gas, increases exponentially, but is damped due to the transfer of atoms from the stationary to the recoiling state.

experiments have used a pump/probe method to measure the coherence in samples. One such experiment [54] uses the directionally scattered light collected on a photodetector to compare the amount of light scattered immediately before one light pulse turns to light scattered when the next pulse turns on. As the grating decays the amount of light scattered at the beginning of the second pulse will not retain the full effect of the buildup of collective scattering from previous pulses and have a reduction in scattering amplitude.

4.2 Demonstration experiment

4.2.1 Experimental setup

Superradiance is a well used tool that has provided useful insights into coherence. In the remainder of this chapter a new, spatially resolved measurement of the coherence in a gas will be presented. Here, instead of solely using the scattered atoms or photons as our signal, we directly image the light used to induce collective scattering onto our CCD camera.

In this experiment we trap atoms in the $|F = 1, m_F = -1\rangle$ state in a magnetic trap characterized by frequencies of $\omega = 2\pi(48, 48, 5)$ s^{-1} in the transverse (x, y) and axial z directions and by a four Gauss bias field directed along the $\hat{z}$ axis. By varying the value of the final RF frequency during evaporation, we are able to examine both thermal and condensed atoms where we have 15×10^6 atoms at $T_c = 250$ nK and pure condensate of 1.6×10^6 atoms.

In order to induce superradiance we illuminate the condensate with off-resonant light along a transverse axis in either the $\hat{x}$ or $\hat{y}$ direction, perpendicular to the long axis of the condensate. For this experiment, we explored a variety of detunings of the light in order to maximize the effectiveness of the imaging technique.

First, the Rayleigh scattering rate for this system must be zero in order to reduce any imaging aberration due to the dispersive effects of the thin, dense gas. As mention in Chapter 3, this cancelation of the Rayleigh scattering rate occurs for detunings on both the D1 (Fig. 4.2) and on the D2 (Fig. 4.3) transitions. For the D1 line, at 102.2 MHz red detuned from the $F = 1 \rightarrow F' = 1$ transition, the calculated off-resonant optical density of the condensate is 0.02. Although the optical density is small, an increase in the effective scattering rate due to superradiance will allow for a spatially resolved absorption image. Also, at this detuning, the off-resonant optical density of

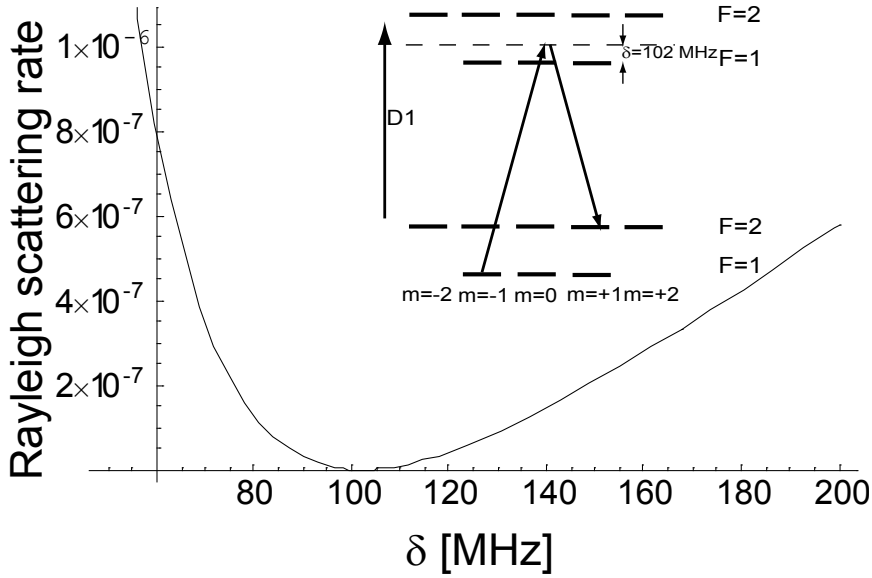

Figure 4.2. Rayleigh scattering rate vs. laser detuning from the $F = 1 \rightarrow F' = 1$ transition for the D1 transition. The Rayleigh scattering rate goes to zero at a detuning δ=102.2 MHz red of the transition.

the thermal cloud, directly above T_c, is .009. A signal at this intensity is too small to distinguish above the noise in the images.

In contrast, for the D2 transitions, at $\delta = 29.2$ MHz red of the $F = 1 \rightarrow F' = 0$, the off-resonant optical density is 2.2. Even with linear Raman scattering the absorption of light by the sample is too large to be used for spatially resolve *in-situ* imaging. At the other dispersive free imaging frequency on the D2 line, $\delta = 150$ MHz, the off-resonant optical density is 0.6. Although this detuning is ideal for off-resonant Raman-absorption imaging (ORLA, Sec. 3.2.2), any large enhancement due to coherence will increase the absorption such that any spatial structure that may be in the gas will be lost and the extraction of the number of coherent atoms will be obscured. Thus, we choose to work with the weak D1 transition.

At this dispersion-free imaging point on the D1 line, it is important to understand the final state to which the atoms will scatter. A plot of the superradiant scattering rate as a function of time is plotted (Fig. 4.4) for different final states. For each trace,

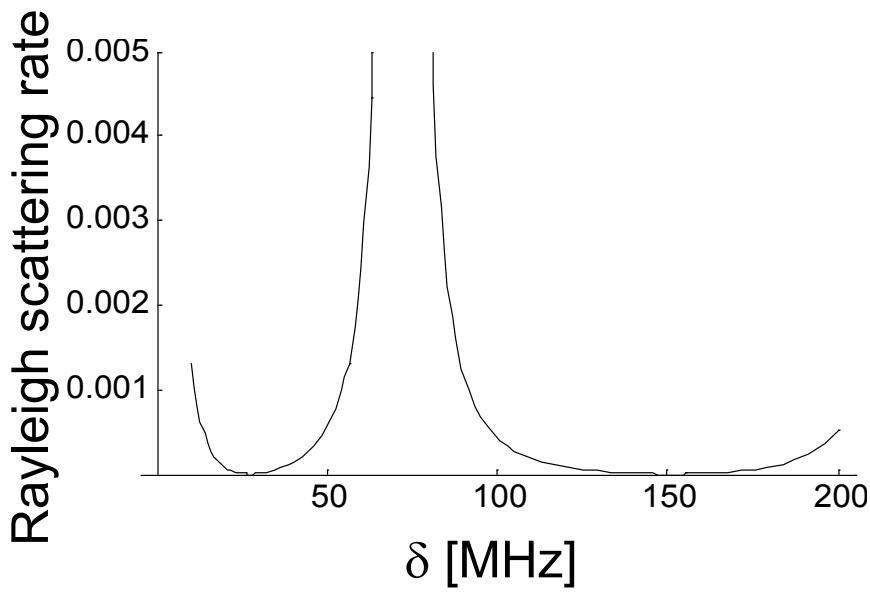

Figure 4.3. Rayleigh scattering rate vs. laser detuning from the $F = 1 \rightarrow F' = 0$ transition for the D2 transition. The Rayleigh scattering rate goes to zero for two detunings δ=27.2 MHz and δ= 151 MHz red of the transition.

we assume that all atoms go into only one final state. The state with the largest gain at this detuning is the $|F = 2, m_F = 1\rangle$ final state (blue). The magnetic moment of this preferred state is nearly equal to the initial state, allowing for simultaneous magnetic trapping, and the relative s-wave scattering length of each trapped state is nearly identical. Also in this plot, we find that Rayleigh superradiance (green) is suppressed. It is interesting to note that the scattering rate of atoms into the $|F = 2, m_F = -1\rangle$ is less due to interference among the excited states.

Before directly imaging the probe light, we examined the Raman superradiance through time-of-flight imaging in our system to gain basic insight on how this process works in both the thermal and condensed gas at the specified detuning. With the geometry of our experiment (Fig. 4.5(a)), the off-resonant superradiance light was required to be along the $\hat{x}$ axis so that first, the light is perpendicular to the extended axis and second, we were able to image with on-resonant light along the $\hat{y}$ axis once atoms were released from the trap. Simultaneous to the on-resonant imaging from

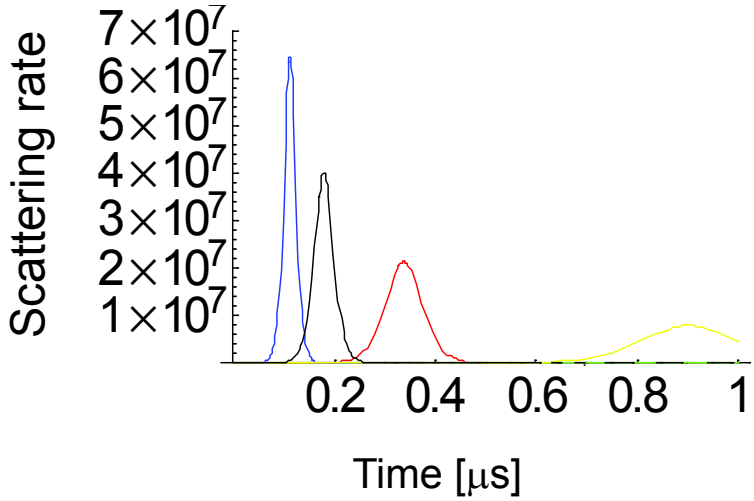

Figure 4.4. Superradiant scattering rate on the D1 line to different final states. For a detuning 102.2 MHz red from the $F = 1 \rightarrow F' = 1$ transition, the calculated scattering rate (assuming no loss) to the $|F = 2, m_F = 1\rangle$ is shown in blue, $|F = 2, m_F = -1\rangle$ is shown in black, $|F = 1, m_F = 1\rangle$ is shown in red, $|F = 2, m_F = -2\rangle$ is shown in yellow, and $|F = 1, m_F = 1\rangle$ is shown in green. The $|F = 2, m_F = 1\rangle$ state is the dominant state thus allowing all atoms to be scattered into this state.

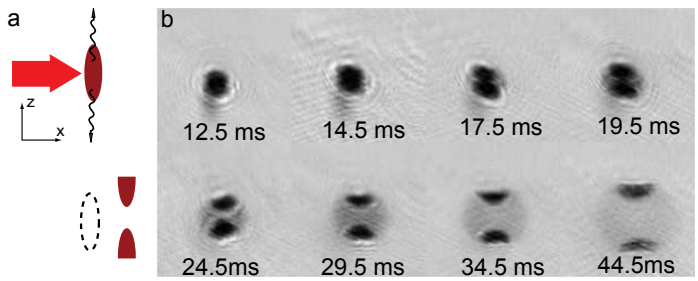

Figure 4.5. Time-of-flight imaging of Raman superradiance. (a) Diagram of the experiment in which detuned light illuminates the gas in the perpendicular $\hat{x}$ direction. Once the atoms are released from the trap, the recoiling atoms expand from the original cloud. (b) A sequence of TOF images taken on different pure BECs with varying expansion times. As the cloud expands and separates, significant spatial structure, i.e. sharp edges, are seen in the recoiling atoms. All atoms from the original BEC scatter light.

above, we collect the directed emission along the $\hat{z}$ axis from one EFM on a photomultiplier tube (PMT). Our initial results confirm two qualitative properties. By applying a magnetic field gradient after releasing the atoms from the trap, we find the final state of the system to indeed be the $|F = 2, m_F = 1\rangle$. Also, for this system, we find that the majority of atoms in the condensate are transferred to the recoiling EFMs.

Using the TOF imaging, we find that the recoiling atoms do not superradiate isotropically, but have a significant structure; one side of each recoiling mode has a sharp linear edge (Fig. 4.5). This structure has been seen in other Raman superradiant studies [52, 54]. We take a number of images on separate samples, but vary the amount of time for which we let the atoms expand. We find that this structure is found even at the earliest times with the two sharp edges originating from the center of the condensate. This feature is not overly surprising. During the superradiant process, atoms are transferred to one of two modes $|r\rangle$ or $|l\rangle$ in which atoms in state $|r\rangle(|l\rangle)$ are propagating to the right (left) and emit into the opposite end-fire mode. The modes are independent and spatially dependent (see Sec. 4.2.2) and consequently retain their shape once they have expanded from the trap.

Once the collective scattering endstate was confirmed using the Stern-Gerlach analysis, we changed the direction of the superradiant light pulses to be along the $\hat{y}$, imaging axis and proceeded to image these probe pulses while also collecting the light along the EFM on a PMT. As an initial proof of principle experiment to show that there is an enhancement of the absorption due to collective behavior, we used a single pulse of light (Fig. 4.6). We imaged both Rayleigh and Raman superradiant processes and indeed found that for Rayleigh superradiance, image abberations, even at large detunings, were prevalent. However, we also concluded that enhanced absorption is possible, and that using Raman superradiance was a superior method.

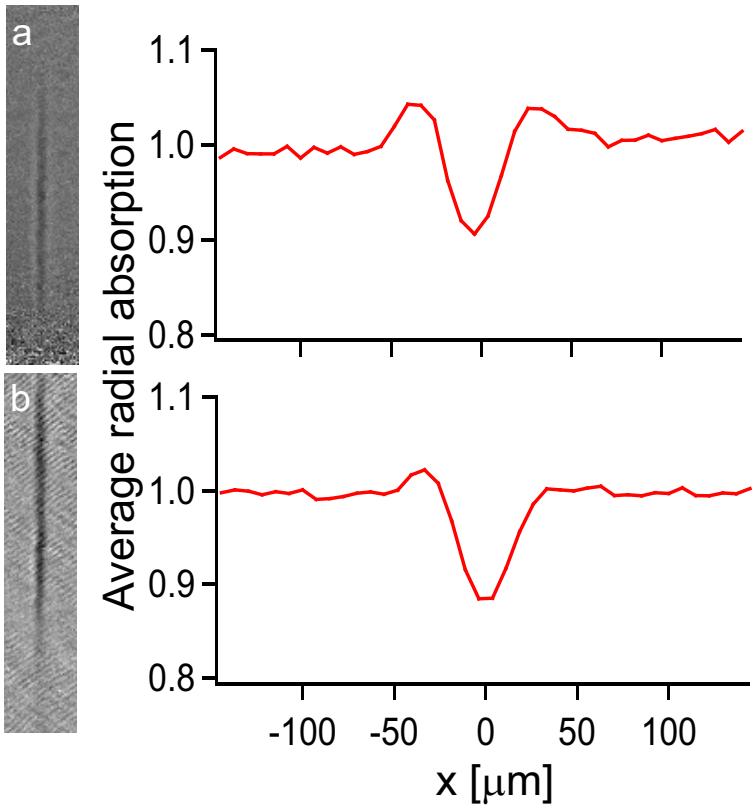

Figure 4.6. Rayleigh and Raman superradiant-enhanced absorption. (a) Coherence-enhanced absorption image with probe light 600 MHz red-detuned from the $F = 1 \rightarrow F' = 1$ transition on the D1 line. (b) Coherence-enhanced absorption image with probe light 102 MHz blue-detuned from the $F = 1 \rightarrow F' = 1$.

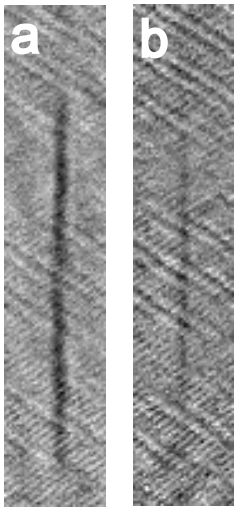

Figure 4.7. Comparison of absorption images with and without spin-grating destruction. (a) Single pulse coherence-enhanced image with a peak absorption of 12%. (b) Single pulse coherence-enhanced image with on-resonant $F = 2 \rightarrow F' = 3$ transitions. Here the peak absorption is 2% due to the destruction of the coherence by the on-resonant light.

We also confirmed that the scattering enhancement was due to atoms scattering into the $F = 2$ final state. During the single pulse, we illuminated the atoms with light resonant with the $F = 2 \rightarrow F' = 3$ transition to disrupt the coherent spin grating. This light, being 6.8 MHz detuned from the $F = 1$ atoms, does not pump the stationary atoms. We found a significant reduction in the absorption enhancement (Fig. 4.7) and any superradiance that occurred was due to atoms scattering into the $|F = 1, m_F = +1\rangle$ state with a significantly lower gain.

Although we were able to spatially resolve the condensate with a single pulse, we could not guarantee that the thermal cloud did not also experience an enhanced scattering. In order to circumvent this problem, we implemented coherence-enhanced imaging in a multiple pulse regimes. With the first light pulse atoms are superradiated from both the thermal and condensed atoms. However, after the first pulse of light is extinguished, those atoms with $\tau_c < \tau$ have any collective scattering effect negated.

Thus, with the second pulse of light, only atoms with $\tau_c > \tau$ will have an enhanced absorption.

To set the delay time between pulses, we first measured the first-order spatial correlations of a thermal gas at T = 1 mK > T_c using a two pulse experiment. Using light collected on the PMT, we measure the ratio of scattered light from the first two pulses as described earlier (Fig. 4.8). For these thermal atoms we find that any effect due to collective scattering decays within $\tau_c^{thermal}$= 20 ± 3 μs. For a 1 mK cloud, we expect the decay time to be 23 μs. The measured decay time of the thermal cloud above T_C matched well with the experimental study.

For multiple pulse coherence-enhance imaging, we induce Raman superradiance with multiple short pulses of light, 100 μs in duration separated by 68 μs delay (Fig. 4.9). This delay time was chosen empirically to be shorter than τ_c^{BEC} = 1.6 ms but larger than $\tau_c^{thermal}$ = 45 μs at T=250 nK. We chose the intensity of the light pulses such that the non-linear scattering rate does not peak during the first pulse. This light level was chosen for two reasons. First, as stated earlier, after the first light pulse only coherent atoms experience an enhanced absorption, eliminating any relevant signal from the thermal atoms. Second, we gain an increase in the signal to noise in later frames that allows for better analysis conditions. Superradiance is an exponential process, which at early times, produces a small photon flux to scattering ratio. As the collective scattering becomes dominant, the rate of scattering increases. By separating these two distinct regions in time through separate image frames, frames with maximal photon scattering can be separated from frames with low photon scattering leading to a large signal in later frames.

Similar to previous *in-situ* imaging techniques discussed in the previous chapter, we record three separate images, each with 20 frames, 50 pixels wide, to gain the most amount of information on an experimental run. Depending on the intensity of

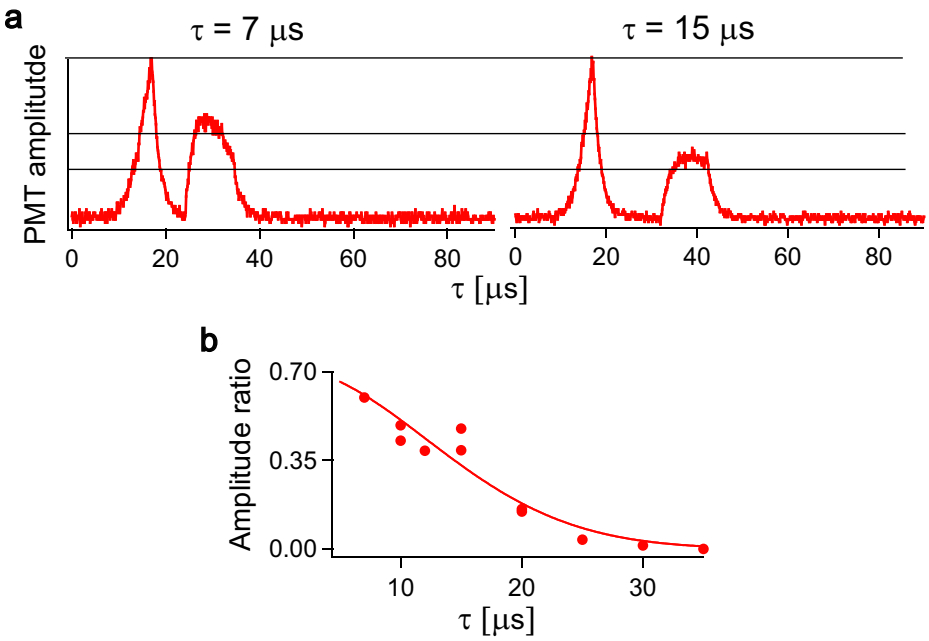

Figure 4.8. Decay time of the spin grating in a thermal gas. We analyze the superradiated light from the EFM collected onto a PMT of a thermal gas above T_c. It was illuminated it with two short pulses of detuned light whose intensity is sufficient that after the second pulse over half of the atoms have superradiated. (a) PMT traces of light scattered down the EFM for a delay time of $\tau = 7$ μs (left) and $\tau = 15$ μs (right). During the first pulse, an exponential rise in the scattering rate is seen as an increase in light on the PMT. It reaches a final scattering shown by the top line. During the beginning of the second pulse, the scattering rate has dropped relative to the end of the first light pulse indicated by the bottom two lines. The ratio of the height of the beginning of the second pulse to the height of the end of the first, measures the loss in the system. This value is plotted in (b) as a function of τ. The solid line is a Gaussian fit determining the spin grating decay time, τ_c=20 μs.

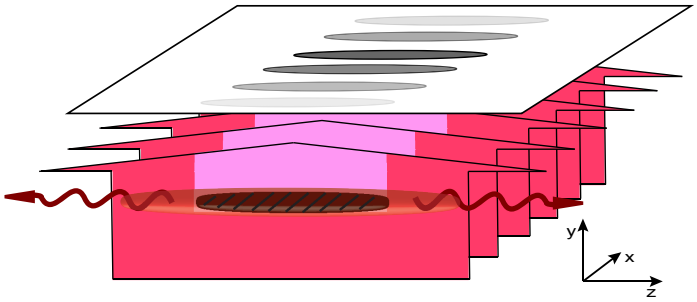

Figure 4.9. Experimental scheme for coherence-enhanced imaging. Short-pulses of light illuminate a prolate gas perpendicular to the magnetic field axis ($\hat{z}$). Superradiance establishes a coherent polarization grating in spatially coherent portions of the gas, causing collective absorption of probe light and its re-emission along the end-fire modes. Each incident pulse is imaged separately, yielding images such as shown in Figure 2.

probe light, the number of frames with discernable absorption will vary because the atoms become dark to the probe beam once they scatter light. The overall goal of the image processing is to extract the number of missing photons as a function of position to give the total number of coherent atoms per pixel. There are a variety of noise sources in the image including photon shot noise, structure in the probe beam, fluctuations in the probe intensity, and jitter in the probe position. For this data set, we used some of the previous noise reduction techniques discussed in the imaging chapter including a gaussian blur smaller than our image resolution. Once this was completed, we found that the dominant noise source came from the jitter in the probe position that occurred during the seven second camera download. Thus, in order detect the structure of the probe beam, we used the average of the last five frames in the first image to represent a "bright field". This normalization has a second advantage that any absorption due to the thermal cloud will be subtracted from the original image.

The second significant hurdle in extracting reliable numbers for absorbed photons per pixel is that the intensity between pulses varies. Thus, a reliable pulse-by-pulse normalization is required. This process occurs by first, excluding the region of each

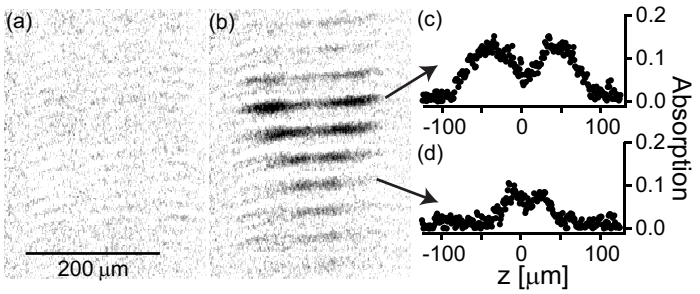

Figure 4.10. Direct, *in situ* imaging of coherence in a BEC. (a) Normalized, multiple-pulse coherence-enhanced image for a single gas at $T/T_c > 1$ in which no absorption is seen. (b) Normalized, multiple-pulse coherence-enhanced image for a gas at T/T_c=.3. A peak absorption of 15% is achieved. (c) Cross-sections of the gas at T/T_c=.3 for pulse 4 and 6 showing significant spatial structure in the gas.

frame that contains atoms and any pixels along the chip mask. This excludes about one-half of the frame. With the remaining region, we use a least squares fit of each frame to the bright field to find an overall offset, due to dark current in the chip, and multiplicative scaling, due to probe beam intensity, for the overall normalization. The typical multiplicative values for the difference in intensity fall between 0.9 to 1.1.

4.2.2 Spatial structure

Once the signal to noise level was increased, we obtained spatially resolved coherence-enhanced images to demonstrate the effectiveness of this technique (Fig. 4.10). These images show a progression of absorption with multiple probe pulses culminating in an overall peak absorption of 15%, an enhancement of ~ 10. Once the peak absorption is reached, the level of enhancement decreases due to the depletion of the condensate as atoms are optically pumped from the initial to far off-resonant final state. These images show a distinctive pattern of scattering in which the ends of the extended sample darken first compared to the denser cloud center. This inhomogeneous scattering has been discussed in references [55, 56]. Previous studies of superradiance in extended BECs have indirectly observed spatial structure [53, 54],

coherence-enhanced imaging gives both temporal and spatial resolution of the entire superradiant process.

4.2.3 Determination of condensate number

The determination of the condensate number from this method can be found in reference [40]. A few key points that should be pointed out is that above T_c, no discernable absorption is seen. However, as the temperature was lowered, the coherent portion of the gas showed an enhanced absorption. This imaging method's major achievement is to spatially resolve the coherent portion of the gas. However, this imaging method has a major drawback, namely that the center of the condensate does not fully superradiate. This effect can be seen both in the multiple pulse image (Fig. 4.10) and in the single pulse Raman image (Fig. 4.6(b)). This incomplete scattering is due to the reduction in the gain that occurs when the condensate experiences inhomogeneous scattering. As the ends of the sample complete their scattering, the sample becomes effectively shorter, decreasing the value of the overlap integral, A_Ω. Thus, before the center of the cloud completes its superradiant scattering, the gain is too low to have efficient enhancement.

4.2.4 First order correlation functions

This coherence-enhanced imaging uses multiple pulses of light to build up the coherence in the sample and separately records the scattering from each pulse. For this measure, we raise the light intensity such that the peak of the scattering occurs during the second pulse and measure the ratio of the absorption from the second frame compared to that of the first. If the two points are incoherent, the absorption in the second pulse will be virtually identical to the absorption in the first pulse at this detuning. However, if the two points are correlated, the amount of absorption in

the second pulse will exceed that in the first. By varying τ, we are able to measure the interference across the entire width of the cloud. This measure of the correlation function is similar to that measured with the PMT in the thermal cloud, however, due to the collected images of the atoms, we gain unprecedented spatial resolution, integrated out of the system with the previous PMT signal, with which we place a lower bound on the correlation length in the gas. The images of these correlation maps can be found in [40]. We find some distinctive features in the correlation functions in which the ends of the condensate seem to agree with the calculated correlation times due to Doppler dephasing.

This good agreement of the correlation time to the Doppler limit breaks down at the high density centers of the gas. Instead of taking this data to imply that the center of the cloud is less coherent than the rest, we search for an alternate explanation. One such explanation could be the destruction of the spin grating due to atom-atom collisions. The atoms in the EFMs travel through the condensate at v_{rec}, four times larger than the speed of sound in the system. Therefore, there is no significant suppression of collisions due to the superfluid nature of the gas [57]. For the coldest cloud at $T/T_c = 0.3$, the linear (non-collective) per-particle scattering rate for a gas with density n and collisional cross-section σ, is given by $\Gamma_l = n\sigma v_{rec} = 300$ s^{-1}, which is too small to significantly affect the observed correlation times. Therefore, we must consider a collective per-particle scattering rate i.e. collisional superradiance, to determine its effects on grating dephasing.

In general, collective scattering occurs when the number of scatters, N, exceeds the number of modes, M available in which the system may scatter. For this calculation, we assume that the BEC has a constant density n and the number of atoms in a sphere of radius r is just $N = n/(4/3\pi r^3)$. The number of modes available for this system is $M = r^2/k^2$ where $k = 2\pi/(795\ \mathrm{nm}/\sqrt{2})$. The rate at which atom-atom

scattering occurs is

$$\Gamma_{nl} = \epsilon \times \Gamma_l \tag{4.3}$$

$$\epsilon = N/M = \frac{4nr\pi}{3k^2}$$

For this calculation, a self-consistent value of r is chosen, $r = v_{rec}\Gamma_{nl}$, i.e such that an atom propagating at the recoil velocity scatters once in that radius. Thus

$$r = \frac{\Gamma_l N(r) v_{rec}}{M(r)} \tag{4.4}$$

For this system, the effective radius is $r = 4.1$ μm, which give $\Gamma_{nl} = \sqrt{(\Gamma_l v_{rec}\lambda^2 n)/6\pi} \simeq 1/(500\ \mu\text{s})$. This prediction is in good agreement with the observed correlation time at the high density cloud center. As the density decreases, we find that the correlation time increases and the collisional superradiance is suppressed letting the correlation time asymptote to the Doppler dephasing time.

Along with this spatial measurement of the correlation times in the condensate, we attempted to measure the correlation time in the thermal cloud with high spatial resolution. The kinetics mode of the camera does not allow for delay times less than 50 μs, which is the expected correlation time in the thermal cloud. However, we felt that we might be able to make this measurement by imaging two light pulses separated by short delays (τ <50 μs) but imaged on top of one another. We could, through post processing, separating out the two images. In order for this separation process to work, we need reliable single pulse images that would mimic the initial pulse, i.e. images with the same gain. We took a variety of single pulse images and averaged them together to give an "effective" first frame. Next, we subtracted this first pulse from the double pulse images to give us an "effective" second pulse. Similar to the method applied above, we took the ratio of these two pulses and looked for a decay in scattering rate. Unfortunately, where one would expect the thermal cloud to reside, the signal to noise was too low to see any scattering.

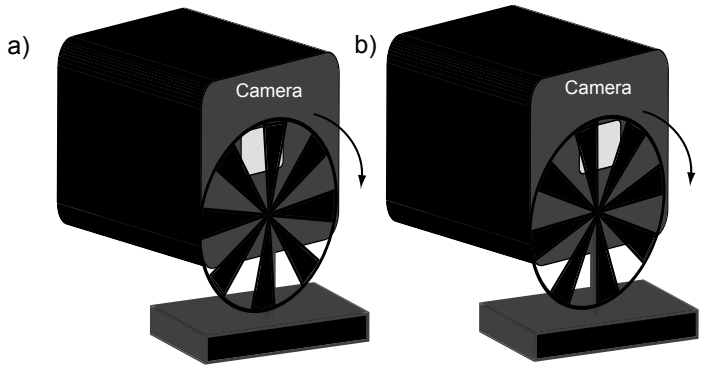

Figure 4.11. Coherence imaging without kinetics mode

4.3 Future outlook and imaging variations

Coherence-enhanced imaging yields information on both the spatial coherence of the ultracold gas and also on extended sample superradiance. However, there are two main drawbacks to widespread use of this method of imaging. First, the kinetics mode camera is expensive($28,000), and second, the spatial structure seen in the images can make data interpretation difficult. With the modifications described below, these two impediments can be overcome.

At the beginning of this experiment, the kinetics mode camera was broken. Thus, we made a de-facto two frame camera from a single frame acquisition camera with the use of an optical chopper wheel (Thorlabs MC1000A). This chopper wheel was placed directly in front of the camera and synchronized with the pulsed imaging light (Fig. 4.11). The bladed wheel, optically blocked one-half of the CCD chip during the first pulse of light and exposed half the chip for imaging. As the wheel moved, the blade blocked the first image and allowed for the second half of the chip to be exposed to the light. Although two pulses of light illuminate the atoms, we are only able to image one light pulse because the chopper blade blocks those pixels that would be used in the imaging word during the first pulse. Although circumventing the need for an expensive camera, this method does not give an accurate count of the total number

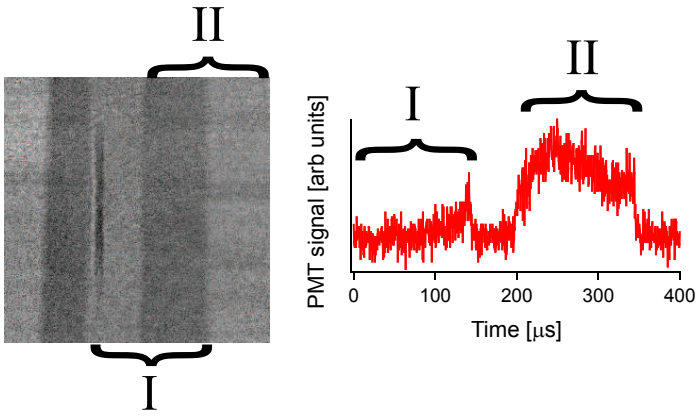

Figure 4.12. Coherence-enhanced image and PMT trace without a kinetics mode camera. During the first light pulse, the chopper-wheel blade blocks the portion of the CCD chip that is indicated by the bracket labeled I. The atoms begin to superradiate, as indicated on the PMT trace. However, no image of this pulse is available because the camera used for this data did not have a kinetics mode setting. After a 50 μs delay, during which time the blade moves to block the region of the CCD chip that is indicated by the bracket labeled II and exposes the portion of the CCD camera to the image. After the wheel moves the second pulse of light illuminates the atoms. During the second pulse, the atoms are exhibiting maximal superradiance and the probe pulse is imaged onto the CCD camera in which enhanced absorption can be seen for the coherent portion of the gas.

of atoms. This inaccuracy arises from the inability to count those photons scattered in the initial pulse (Fig. 4.12). However, with a judicious choice of probe intensity, the scattering from the initial beam can be minimized and the majority of light can be scattered in the second pulse. Second, due to the nature of the moving chopper wheel, only specific harmonics of the rotation frequency could be used limiting the values of the delay τ.

The second hurdle to overcome from this coherence-enhanced imaging method is the significant spatial structure seen in the imaging sequence. Although this has provided interesting evidence for inhomogeneous scattering in extended samples, it can be difficult to remove from the images. One way to overcome this is by using a well controlled two photon Bragg pulse instead of the random superradiance process to create the initial grating. Unlike the first Raman superradiance, the Bragg pulse

sets up a uniform polarization grating through the gas allowing for simultaneous superradiant scattering from the second pulse.

Even with the aforementioned drawbacks to this imaging method, one would argue that the simplicity and added features seen during the superradiant pulse add exciting new prospects for the quantum-optics field. One exciting aspect, recently pointed out [56] is that the fluctuating asymmetries in spatial absorption may lead to further understanding of the initial quantum seed of the superradiant process. With further studies the number of seeded optical modes in this process may be better understood.

Chapter 5

Spontaneous symmetry breaking and defect formation

This chapter describes the spontaneous symmetry breaking and formation of defects in a spinor Bose-Einstein condensate as the system traverses a quantum phase transition. This work was published in:

- *L. E. Sadler, J. M. Higbie, S. Leslie, M. Vengalattore and D. M. Stamper-Kurn, "Spontaneous symmetry breaking in a quenched ferromagnetic spinor Bose-Einstein Condensate, Nature (London) 443 312*

Nature is replete with systems showing symmetries, which include examples of fractals in art, shells on a beach, and the early universe. On the surface, these symmetrical systems are often times aesthetically pleasing but, there exists a deeper mathematical connection to the physical world. Noether [58], in 1905, directly connects the symmetry in a system to a conserved physical quantity. One example is that a rotational symmetry implies a conservation of angular momentum.

A simple example of symmetry breaking can be illustrated by a classical object,

a sharpened pencil. If this object is placed in a gravitational field, balanced on its tip, it has a perfect cylindrical symmetry around its long axis. However, this object is dynamically unstable. Allowing for any slight perturbation to the pencil, when it falls, it will break the previous symmetry. The direction in which the pencil falls is random, leading to a different end state of the pencil after each run of this "experiment" although the same dynamical process occurs in each run. This example, although simple, contains many of the fundamental concepts including the dynamical instability and randomness of outcome that is inherent in a more complicated system.

This chapter describes the dynamics of a spinor Bose-Einstein condensate as it is quenched across a quantum phase transition from a non-magnetic to ferromagnetic state. This system displays spontaneous symmetry breaking through the formation of ferromagnetic domains. We observe with a non-destructive, *in-situ* imaging technique the formation of spin-textures, domains and domain walls, and topological defects-vortices containing non-zero spin current but no net mass current. Specifically, I will describe the physics behind the quantum phase transition in section 5.2, focusing on a mean-field description and explaining previous work in this field. Next, the experimental details are explained in section 5.3. Finally, in sections 5.4 and 5.5, experimental results will be described giving confirmation of the phase transition, yet leaving us with some somewhat puzzling, questions left to be answered.

5.1 Nature of spinor BECs

Most studies of BECs have occurred in atoms with multiple magnetic sublevels [59, 60], but due to the interactions of atoms with the trapping fields, these multiple magnetic sublevels and their interactions are difficult to study [15, 61]. This exclusion of an internal degree of freedom has relegated many studies to *scalar* condensates with a single degree of freedom, the overall condensate phase. However, by simultaneously

trapping multiple internal states of a gas, interesting interactions between particles can occur allowing for an experimental investigation of new types of dynamics in a system [11, 62].

These multicomponent systems were first realized in a two state spinor system consisting of ^{87}Rb gas [63, 64] in which the magnetic trap was constructed such that the magnetic moment of the two species of atoms were identical. The overlap of these two species in a BEC allowed for the study of the interactions of particles in differing states. However, in this system, only two specific spin states could be studied, and the interactions between all magnetic sublevels are excluded.

With the advances in optical trapping [27], the confinement of atoms no longer relies on their magnetic moment and this optical trapping potential allows for simultaneous trapping of all magnetic sublevels. In second quantized notation the Hamiltonian for the system is

$$H = \int d^3\vec{r}\left(\psi^\dagger(\vec{r})\left(\frac{-\hbar^2\nabla^2}{2m}\delta_{ij} + U_{ij}(\vec{r})\right)\psi_j(\vec{r})\right) + \frac{g_{ij,kl}}{2}\int d^3\vec{r_1}d^3\vec{r_2}\left(\psi_i^\dagger(\vec{r_1})\psi_j^\dagger(\vec{r_2})\psi_k(\vec{r_2})\psi_l(\vec{r_1})\delta(\vec{r_1}-\vec{r_2})\right) \tag{5.1}$$

where the indices represent the different components of the gas and repeated indices are summed. U_{ij} is the confining potential for the gas and the interaction term, i.e. the second integral, characterizes both elastic and state changing point-like collisions.

These interactions can be simplified if the system is invariant under rotation. This condition is met in a spinor condensate at zero magnetic field in which simultaneous trapping of a complete magnetic sublevel manifold is realized. Thus, the interaction term can be simplified to

$$V(\vec{r_1}-\vec{r_2}) = \delta(\vec{r_1}-\vec{r_2})\sum_{F_{tot}}^{2F} g_{F_{tot}}\wp_F \tag{5.2}$$

$$g_{F_{tot}} = \frac{4\pi\hbar a_{F_{tot}}}{m}$$

where F_{tot} is the total spin of the system, $a_{F_{tot}}$ is the s-wave scattering length between the pair, and $\wp_F$ is the projection operator for the state [11, 62].

If we consider only a system of F=1 bosons, the symmetry of the system allows only collisions between particles with total spin F_{tot}=0 and F_{tot}=2. In this work, we consider only consider collisions in the system that conserve the total angular momentum. Therefore, only the proceeding collisions are allowed.

$$|m = 0\rangle + |m = 0\rangle \leftrightharpoons |m = +1\rangle + |m = -1\rangle \tag{5.3}$$

and we see that spin mixing can occur. This further simplification can be expressed as

$$V = c_0 + c_2 \vec{F_1} \cdot \vec{F_2} \tag{5.4}$$

where $c_0 = (g_0 + 2g_2)/3$ representing the spin-independent interaction energy per particle and $c_2 = (g_2 - g_0)/3$ representing the spin-dependent interaction energy per particle. Thus, depending on the sign of the difference in scattering lengths, there are two distinct ground state available for the system. If $c_2 > 0$ the system mandates a minimization of $\vec{F_1} \cdot \vec{F_2}$ leading to an anti-ferromagnetic ordering. This system has been realized in ^{23}Na [65, 66, 67], which confirmed its anti-ferromagnetic nature. Conversely, if $c_2 < 0$, the system tries to maximize the spin alignment leading to a ferromagnetic ordering. Previous studies of ^{87}Rb have found ferromagnetic ordering in the condensate [68, 69]. For a condensate with density similar to our experiment, $n \sim 2 \times 10^{14}$ cm^{-3}, the spin-dependent energy of the system is on the order of $|c_2|n = h \times 8$ Hertz. This energy from this interaction preferentially drives the above collision in Eq. 5.3 from left to right through spin-mixing collisions.

5.2 Quantum phase transitions

The symmetric spinor system, presented above, neglects any external fields, e.g. magnetic or electric fields, that may break the symmetry of the state. In particular, magnetic fields are prevalent in most experimental apparatus. This leads to a variety of corrections to the overall Hamiltonian, effecting the energy in the system arising from the linear Zeeman shift, magnetic field gradients, and quadratic Zeeman shift.

First, consider the linear Zeeman shift. Here, the energy per particle for a field with strength B is given by $E = (h \times m_F \times 700 \times B)$ KHz. In order for this energy to be less than the spin energy in the system, $B \lesssim 10\ \mu$G. This level of magnetic bias field is difficult to achieve, often times requiring extensive magnetic shielding and large external coils to cancel any field. However, due to overall conservation of angular momentum and small dipolar relaxation rates, the linear Zeeman shift can be neglected. Second, the effects of magnetic field gradients need to be assessed. The energy due to the gradient at any point z is $E = g\mu_B B' z \langle F \rangle$ Unlike the linear shifts, this effect can not be ignored. Thus, in order for the spin-dependent interaction energy to be the dominant drive for any spin mixing, this gradient must be reduced. Finally, the effects of the quadratic Zeeman shift are needed to fully characterize the system. The energy due to this effect in rubidium is given by $E = q\langle F_z^2 \rangle$ where $q = (h \times B^2 \times 72)$ Hz/G^2. This effect, which increases the energy of the system as the spins of the atoms align, drives spin mixing collisions in Eq. 5.3 to the left, favoring the $|m = 0\rangle$ unmagnetized state,

Assuming that any magnetic field gradient is sufficiently canceled, the true competition for control of spin mixing and ultimately the ground state happens between the spin-dependent interaction energy and the quadratic Zeeman shift. These two ground states, the unmagnetized and ferromagnetic state, are separated by a second-order quantum phase transition occuring when $q = 2|c_2|n$. This phase transition

can be accessed by changing the magnitude of the magnetic bias field across this point. Implicit in this phase transition is the spontaneous symmetry breaking that occurs when the system traverses the quantum critical point in which the system must change from one ground state at high magnetic field with a Z(2)×U(1) group symmetry to a ferromagnetic state with SO_2×U(1) group symmetry [70].

5.3 Experiment

In our lab, we studied the dynamics that are present in the system when the spinor condensate is quenched across this transition. The starting point for this experiment, differing from a typical magnetically trapped BEC experiment, is the complete transfer of 60×10^6 atoms at 2.5 μK from the magnetic trap to an ODT whose basics are described in Chapter 2. From here, we apply a sequence of magnetic fields to prepare and sweep the system through the quantum phase transition. We initially transfer all atoms initially in the $|F = 1, m_F = -1\rangle$ state to the $|m_z = 0\rangle$ magnetic sublevel using a radio-frequency, rapid adiabatic passage at a 2 G bias field directed in the transverse direction. We then apply a 4 G/cm magnetic field gradient to expel any atoms not in the $|m_z = 0\rangle$ state. Subsequent checks using time-of-flight imaging with a magnetic field gradient confirm the purity of the sample. In order to cool the atoms to degeneracy, we evaporatively cool the sample by reducing the the power of the ODT. The final trap is characterized by oscillation frequencies $(\omega_x, \omega_y, \omega_z)$=$2\pi(56, 250, 4.3)$ Hz with a trap depth of $k_B \times 350$ nK.

Once a condensate is formed, we ramp the bias field through the transition over 5 ms to 50 mG, slow enough such that all atoms remain in the $|m_z = 0\rangle$ state. The final state, at the end of the ramp is confirmed yet again with a time-of-flight imaging with a field gradient bounding any population in the $|F = 1, m_F = \pm 1\rangle$ to less than

0.3%. The final magnetic field gradients in the system were nulled to less than 0.2 mG/cm.

The prepared condensate contains $2.1(1)\times10^6$ atoms at 40 nK, has Thomas-Fermi radii $(r_x, r_y, r_z) = (12.8, 2.0, 167)$ μm ,and has a peak density n_0=2.8×10^{14} cm^{-3}. With the above parameters, we can calculate the spin-healing length $\xi_s = \sqrt{\hbar^2/2m|c_2|n_0}$=2.4 μm, classifying the system to be quasi-two-dimensional with respect to the spin dynamics in the system. Similarly, the valid energy scale in the system, the spin-dependent mean-field energy calculated from the parameters of the BEC is $2|c_2|\langle n\rangle_y$=h$\times$16 Hz where $\langle n\rangle_y$ is the averaged density in the $\hat{y}$ direction. This dominates the energy due to the quadratic Zeeman energy q=h$\times$0.2 Hz.

5.4 Spontaneous formation of ferromagnetic domains

The search for dynamics associated with the quenching of the system across the transition occurred in many ways. To begin, we used a similar method to [68, 69] to measure the spin-mixing in our system using a time-of-flight imaging methodology with a magnetic field gradient. The accuracy of this measurement is limited due to the high optical density in the clouds on resonance. However, with this method, we similarly find that the system experiences a spin-mixing dynamics in T_{mix}. From this measurement, we determine after $T_{hold} >> T_{mix}$ that the populations for each spin state, in the $\hat{z}$ basis after long wait times are

$$\begin{aligned} \rho_{-1} &= 1/2 \\ \rho_0 &= 1/\sqrt{2} \\ \rho_{-1} &= 1/2 \end{aligned} \tag{5.5}$$

Unfortunately, with this Stern-Gerlach analysis, we are unable to determine if the

system is ferromagnetic. The populations describe above in Eq. 5.5 could describe the wavefunction

$$\psi_F = \begin{pmatrix} 1/2 \\ 1/\sqrt{2} \\ 1/2 \end{pmatrix} \tag{5.6}$$

which is ferromagnetic and points in the $\hat{x}$ direction, or

$$\psi_p = \begin{pmatrix} 1/2 \\ i/\sqrt{2} \\ 1/2 \end{pmatrix} \tag{5.7}$$

which is polar. Thus, to characterize the nature of the wavefunction, it is necessary to determine coherences between the different spin states. We are able to do this by applying the magnetic sensitive imaging described in Chapter 3 to look for the spontaneous magentization of the system. Simultaneously with this new measurement, we will gain spatial information about the size of any ferromagnetic domains.

For this study, we illuminated the condensate with 24 pulses of light for which the transverse magnetic bias field is at 50 mG, corresponding to a Larmor frequency of 35 kHz. We sample the system with a strobe frequency of 10 kHz. We then image the cloud after adiabatically ramping the field over 5 ms to point in the $+\hat{y}$ followed by a similar image with the field pointing in the -$\hat{y}$. Thus we are able to fully characterize both the transverse and longitudinal magnetization in the sample. Atoms in these images will have different signals depending on their internal state. Atoms remaining in the $|m_z = 0\rangle$ state, should show no Larmor precession whereas atoms that are in either the $|m_F = \pm 1\rangle$ state will exhibit spontaneous precession.

We show multiple-pulse images for various T_{hold} (Fig. 5.1) and find that at short hold times, no Larmor precession is visible. We infer from this that either the atoms have remained in the $|m_z = 0\rangle$ state or that any domains with transverse magnetization that have formed are smaller than the imaging resolution in the system. As we

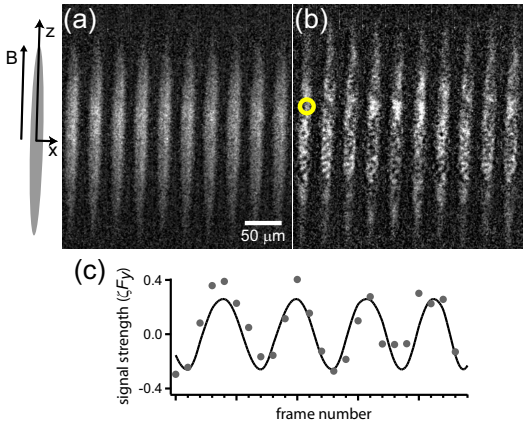

Figure 5.1. Direct imaging of spontaneous magnetization using polarization sensitive imaging. Imaging sequence showing the the magnetization of the gas for a single condensate at (a) $T_{hold} = 36$ ms and for (b) T_{hold}= 216 ms. (c) Plot of the amplitude of the phase contrast system for a single point from (b) indicated by the yellow circle showing the Larmor precession as a function of the frame number. Figure taken from [71]

hold the gas for longer times, we find the system to spontaneously form domains of non-zero, transverse magnetization, bounded by walls of atoms with no magnetization.

For this study, the experiment was run multiple times at each T_{hold}. We find that at each hold time the resulting images have similar overall characteristics, but their details vary. We process these images to extract spatial maps at each point $\vec{\rho}$ of the complex transverse magnetism $F_T(\vec{\rho})= F_x + iF_y$ by extracting the amplitude $A(\vec{\rho})$ and phase $\phi(\vec{\rho})$ of the Larmor signal. We combine these two values to create a single representation of the system in which the amplitude of transverse ferromagnetism is given by the brightness and the phase is given by the hue. At short hold times (Fig. 5.2(a)) we find that on most shots, no significant ferromagnetism occurs. However, due to the non-adiabatic quench of the system, the creation of domains is a random process. Thus, in one of the experimental runs, i.e. second example in Fig. 5.2(a), ferromagnetic domains are already present. Similarly as the evolution of domains

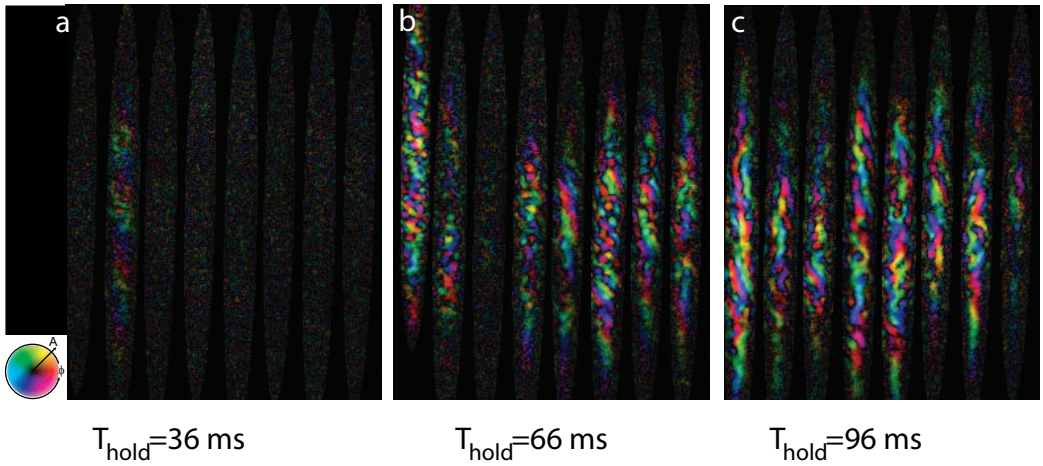

Figure 5.2. *In-situ* images of ferromagnetic domains and domain walls for short T_{hold}. The transverse magnetization density is shown with the magnetization orientation ($\phi = \arg(F_T)$) indicated by hue, and magnitude ($A = \zeta|F_T|$) indicated by brightness. The maximum brightness, shown by the color wheel at left, corresponds to full magnetization of the condensate center. Multiple images, each from a separate experimental run, are shown for T_{hold} for (a) 36 ms (b)66 ms and (c) 96 ms. Regions outside the condensate are indicated in black.

proceeds (Figs. 5.2(b-c)), each set of images show similar qualitative properties with one or two runs that seem to differ.

The development of ferromagnetism in the spinor condensate continues as T_{hold} increases (Fig. 5.3). Within these experiments, there are a variety of features that distinguish different domains (Fig. 5.4). First, large domains, $\sim 50-200$ μm span the longitudinal direction of the condensate in which the phase of the ferromagnet twists by 2π. Second, small domains $\sim 10\mu$m, form in the axial direction in which adjacent domains, separated by unmagnetized domain walls, have opposite phase. Finally, we see polar-core spin vortices (see Sec. 5.5) in over 1/3 of all images. Besides gaining qualitative information about the dynamics of spontaneous ferromagnetism, we are able to quantify the timescale for the onset of ferromagnetism, the degree to which the sample magnetizes, and the size of the axial domains in the system [71]

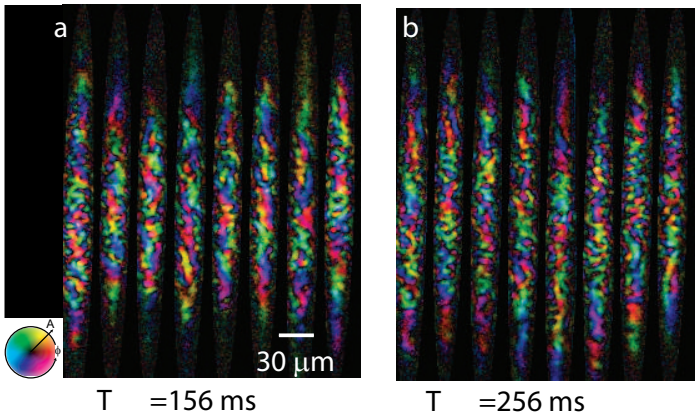

Figure 5.3. *In-situ* images of developed ferromagnetic domains.

5.5 Defect formation

5.5.1 Kibble-Zurek mechanism and the early universe

Often, physical concepts that define one subfield of study cross-over to other subfields due to similar phenomena. This is true with the Kibble mechanism [45] that describes spontaneous symmetry breaking leading to defect formation in the early universe. This theory suggests that systems in which a gauge symmetry has been broken due to a thermal phase transition and where a vacuum expectation value is acquired, should, above some critical temperature, be able to restore its broken symmetry. More specifically, phase fluctuations in the symmetric state abound when the thermal energy of a sample at high temperature allows for a sampling of an entire potential. However, as the temperature decreases, the system looses this energy and a particular phase is chosen freezing out the fluctuations. A key point of the Kibble mechanism states that the system will pick out different phases in different parts of the system that are causally disconnected and thus did not have the ability to interact when the phase transition occurred.

One well know example of symmetry breaking in particle physics is a system

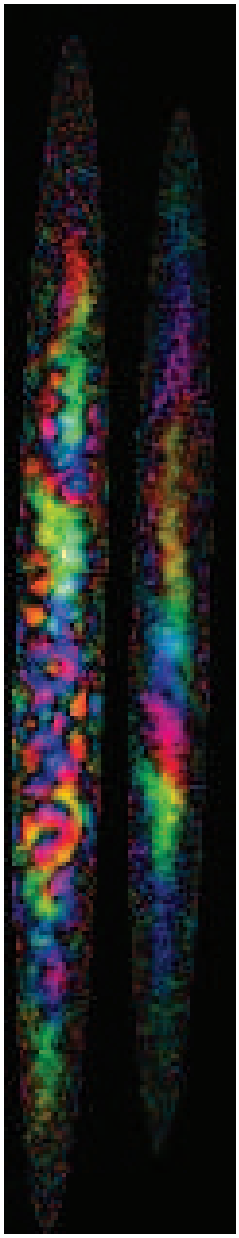

Figure 5.4. Amplitude and phase maps of ferromagnetic domains at 210 ms. The two maps shown here illustrate the large variety of features in the quenched ferromagnet. The image on the left has many small domains that rapidly change phase in the axial direction separated by unmagnetized gas. In comparison, the image on the right has one large domain in which the phase slowly rotates over 200 μm in the longitudinal direction.

that can be describe with a Mexican hat potential. This double well potential in one dimension has a center that is a local maximum whose energy is greater than the available energy once the system cools through the phase transition. During the phase transition, points in this system choose phases at random, either $|\uparrow\rangle$ or $|\downarrow\rangle$. As the these regions of definite phase grow, the separated regions must meet. Due to the continuity required in phase, the system develops a topological defect (in this case a domain wall) between regions in an $|\uparrow\rangle$ versus $|\downarrow\rangle$ state.

This theory has significant ramifications for the early universe. It is believed that the universe went through a thermal phase transition following the big bang and thus, at some point in the early time, broke a previously unbroken symmetry. However, when the symmetry of the universe was broken, topological defects may have formed whose type depend on the initial and final symmetry of the system. Thus, one could detect the domain structure (including domain walls and cosmic strings) of the universe as an experimental signatures of the big bang.

These experimental signals have thus far been undetected (one of the motivations for the theory of inflation), but, as Zurek points out [46], these theories used to describe the big bang may also be applied to systems such as superfluids, i.e. ^{4}He. He proposes that liquid helium, held in a circular container, rapidly quenched through the superfluid phase transition via a change in pressure will exhibit two measurable signals. The first measurable consequence of the quench would be the formation of quantized vortex lines within the fluid. The second, more measurable effect would be a mass superfluid flow in an annulus around the container. Kibble also proposes that when the system is quenched that the system tries to maximize the density of defects.

5.5.2 Topological defects in other systems

Experimental studies of topological defect formation in condensed matter systems have occurred in liquid crystals [72] and superfluid helium [73, 74, 75]. Each system has unique properties that allow for different types of studies. For example, in nematic liquid crystals [72], a material that can be thought of as a fluid with rod-like particles, many phase transitions can occur. On common thermal phase transition occurs when the sample goes from a phase in which the rods are isotropically aligned to a phase in which the rods are ordered. These nematic liquid crystals, due to their symmetry group, show multiple types of topological defects including lines, points, and textures. The time and length scale of defects for this system have previously been studied. Beyond studying the thermal phase transitions in liquid crystals, a more quantum system, i.e. liquid ^{3}He [74], has been used to study the onset of topological defects. In these systems, the liquid helium is quenched through a thermal phase transition locally heating portions of the fluid with nuclear irradiation. They found that vortex cores did form during this transition and were able to measure the density of defects in the system.

In comparison with these previous experiments, the present investigation focuses on a simpler physical system. Due to the weak ferromagnetic interaction energy, the time for thermal equilibration and symmetry breaking is much longer than that needed to bring the system across the symmetry-breaking transition. Furthermore, the present work focuses on a quantum rather than a thermal phase transition. Any temperature dependence of the system, which is difficult to calculate, is frozen and only quantum effects are considered.

5.5.3 Polar-core spin vortices

In the two-dimensional ferromagnetic system, spin-vortices are topological point defects about which the orientation of magnetization winds by $2\pi n$ with n being a non-zero integer. These points are distinguished by the characteristic of their core and by the change in orientation around the point defect. We systematically search for cores in each of our transverse magnetism maps by identifying pixel-by-pixel both "dark" and "bright" pixels. The amplitude of dark pixels is consistent with zero. Conversely, a bright pixel has a well defined Larmor amplitude and phase associated with it. A vortex is defined to by two criteria: 1) the core consists of dark pixels (signifying no transverse magnetism) completely surrounded by bright pixels and having a distance of at least two bright pixels in each direction to another dark pixel and 2) the phase differs around the core by $\pm 2\pi$.

We can estimate the approximate size of the vortex core by using a variational calculation minimizing the total energy in the system. Here, the kinetic energy of the system works to increase the core size and competes with the interaction energy, which tries to minimize the unmagnetized core area. To find the equilibrium size, we choose a variational wavefunction ψ_v

$$\psi_v = \begin{pmatrix} Exp[-i\phi](1 - Exp[-r^2/\xi^2])/2 \\ \sqrt{1 - (1 - Exp[-r^2/\xi^2])^2}/2 \\ Exp[i\phi](1 - Exp[-r^2/\xi^2])/2 \end{pmatrix} \tag{5.8}$$

where ξ is the variational size of the core. This trial wavefunction minimizes the energy of the system when $\xi = .74$ giving us an approximate core size of 1.76 μm, significantly larger than the cores seen in vortices in scalar BECs.

With an understanding of the size of the core, we are able to simulate how this defect will manifest itself in our images. To begin, we create both an amplitude and phase map of a "perfect" vortex in which there is no imaging abberations or shot noise

on the data. The amplitude map is created by producing a defect in the magnetization with an amplitude variation that follows equation 5.8. The phase map is imprinted with a 2π phase winding around the core. Next, these two maps are distorted by a Gaussian blur, to imitate our imaging resolution and obscured by Gaussian noise, which simulates the shot noise. Finally, we apply a second Gaussian blur on the noisy maps as a noise reduction technique (see Sec. 3.3.1).

From here, we employ our vortex-finding algorithm, which systematically searches the amplitude map for vortex core candidates and measures the phase winding around the selected points. For our simulated data, we systematically change the definition of well-defined phase, i.e. a "bright" pixel, by changing the necessary fraction of peak amplitude a pixel is required to have (Fig. 5.5). We are able to measure the efficiency of the vortex finding algorithm at each fraction of peak amplitude by analyzing 100 simulated vortices, each with a differing relative phase. Here, we would like to minimize the required amplitude in order to accurately count those vortices that are present in the data.

However, vortex cores are not the only source of defects in our system. We find domain walls are persistent throughout our data, which, due to noise on our data, could lead to a false identification of a vortex. Thus, we also simulate a domain wall to minimize the amount of false identifications of these vortices. Similar to the creation of simulated vortices, we make phase and amplitude maps for the "perfect" domain wall and then apply the appropriate noise and abberations to the data. Once these false vortex candidates are simulated, we apply the same search algorithm to 100 simulated domain walls (Fig. 5.5). We find that in order to rule out false identification of single domain walls as vortices, we must require a pixel whose phase is well defined to have 1/4 of the peak Larmor amplitude in an image

Spin-vortex defects were observed with high confidence in about one third of all

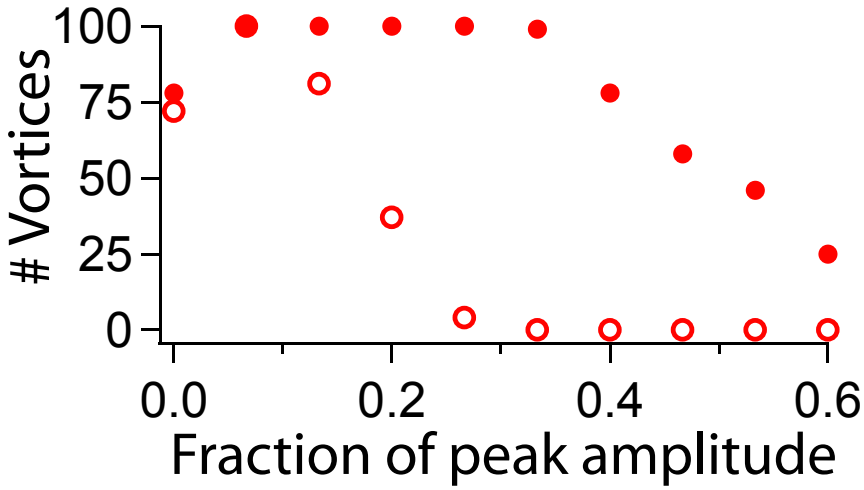

Figure 5.5. Vortex simulations. We show the identification of vortices with our search algorithm as a function of the precession amplitude height required for a pixel to have a well-defined phase (shown as a fraction of the peak precession amplitude). We use 100 simulated vortices (closed circles) and 100 simulated domain walls (open circles) to determine the effectiveness of our search algorithm.

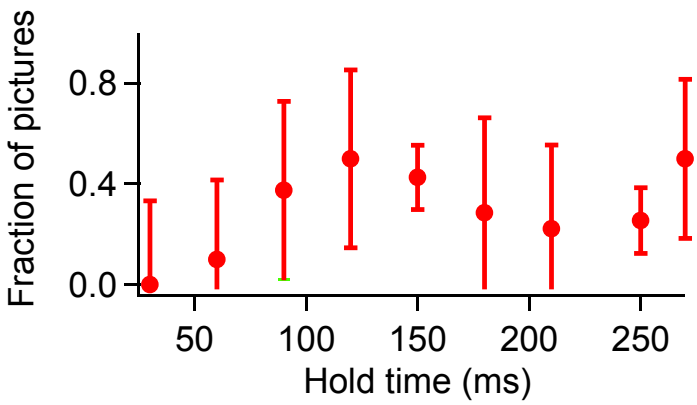

Figure 5.6. Onset of vorticity in a spinor condensate. The number of experimental runs that contain at least one vortex as a function of T_{hold}. The onset of vorticity in the spinor system occurs at the same point as the onset of spontaneous magnetization. The fraction of pictures with at least one vortex saturates to ~ 0.3. The error bars indicate the standard deviation of the number of images that have vortices.

images containing significant ferromagnetism ($T_{\text{hold}} > 90$ ms), with some images containing up to four vortices. The onset of vorticity mirrored that of the onset of the spontaneous magnetization (Fig. 5.6). Due to the small number of images ~ 10 at most times, statistical error dominates the graph and any small variations in number requires a larger sample of images. Some examples of single and multiple vortices can be seen in (Fig. 5.7)

Many types of vortices that can occur in a gas with a multi-component order parameter can be distinguished by the composition of their cores [76]. Based on our measurements of the transverse and longitudinal magnetization at the vortex core, the spin-vortices seen in our experiment appear to have unmagnetized filled cores. This observation supports their characterization as "polar-core" spin-vortices (denoted as $(1, 0, -1)$ vortices in Ref. [76]), for which the superfluid order parameter is a superposition of atoms in the $|m_z = 1\rangle$ state rotating with one quantum of circulation, atoms in the $|m_z = -1\rangle$ state rotating with one quantum of circulation in the opposite sense, and non-rotating atoms in the unmagnetized $|m_z = 0\rangle$ state, which also fill the vortex core. Such a vortex is thus characterized by zero net mass circulation and a spin current with one quantum of circulation. The alternate identification of these vortices as merons [77, 78] is ruled out by the absence of a longitudinal magnetization signal at the vortex core.

The origin for such spin currents is presumably the spinodal decomposition by which ferromagnetism emerges from the unmagnetized cloud. Consider two adjacent domains magnetized in the transverse $\hat{x}$ direction with opposite phase. They will be separated by a domain wall of unmagnetized atoms. However, this wall contains a large amount of energy due to the spin-spin interactions. Thus, it is energetically favorable to magnetize in the orthogonal transverse direction, i.e. $\hat{y}$. The polar core is the remnant of the dynamical instability, an island of m=0 atoms around which the magnetization wraps by 2π (Fig. 5.8).

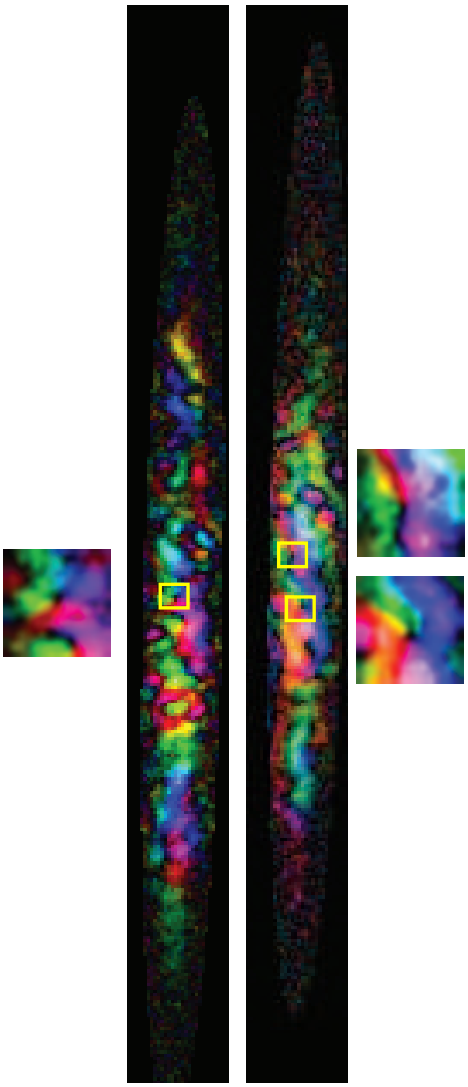

Figure 5.7. Polar-core spin vortices at $T_{\text{hold}} = 150$ ms. Two separate runs of the experiment are shown with the left set of images having one vortex and the image set on the right exhibits two vortices. The smaller images are an enlargement of the vortex region. The yellow boxes on the images indicate the position of the spin vortices.

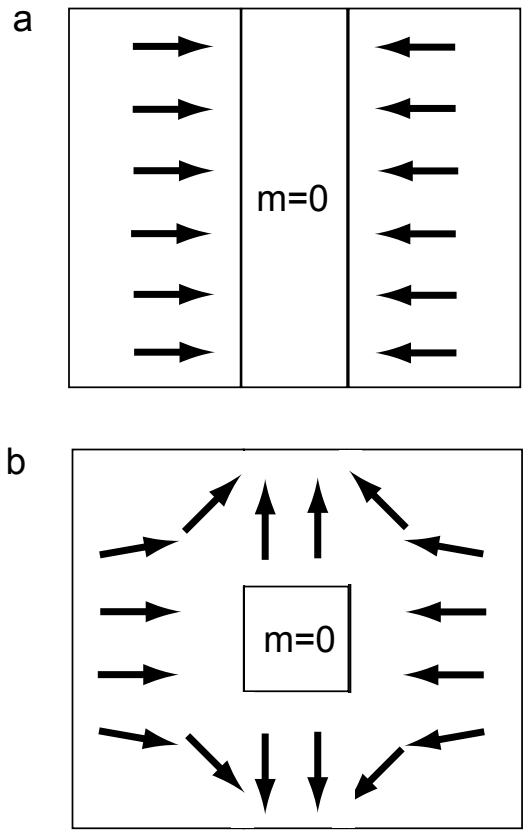

Figure 5.8. Schematic of vortex formation in 2D in the x,y plane. (a) The onset of spontaneous ferromagnetism occurs with the formation of small domains of definite transverse magnetism, opposite in phase, which are separated by a domain wall of m=0 atoms. This configuration is unstable due to the high energy cost of the m=0 atoms. (b) The m=0 atoms in the domain wall will also phase separate in the orthogonal transverse direction leaving a magnetization defect of m=0 atoms in the center with a 2π phase winding around the core. Here the arrows signify the direction of the F=1 spins.

Appendix A

Procedures for cleaning and refilling the recirculating rubidium oven

This Appendix describes the procedure used to clean and replace the rubidium in the recirculating oven. As with any handling of alkali atoms, proper safety procedures (including always using two people) and common sense should be used at all times.

For our recirculating oven with 5 g of rubidium, this cleaning and renewing of the atom source needs to happen about every 7-10 months depending on time in use. The entire process from start to finish takes about six days.

Day One

This is the day we decide we need more Rb. The absorption in the oven is measured and found to have fallen dramatically [13].

- Cool the oven.

- Connect the roughing lines and turbo pump to the oven region, pump out the regions
- If needed, bake the oil trap overnight to get roughing line down to 30 mTorr
- Turn on the Ion gauge in the oven and main chamber (to get a baseline on where we should return).
- Clean tools needed to change oven
  - glove box, hammer, bolts/plate nuts, box wrench, 2 cleaned new copper gasket, container of mineral oil, dry nitrogen, steel try, self closing tweezers, Rb, scissors, clean Al foil
- Cut steel mesh into 3 x 3 inch square and clean using the vacuum cleaning techniques (Table 2.1)
- Turn off vacuum pumps (ion pump, turbo-molecular pump)
- Close block valve between turbo-molecular and roughing pump
- Tee the dry nitrogen line and connect one end to the flood valve on the turbo pump and the other into the glove box.
- When the turbo pump turns off, open the turbo pump vent and allow dry nitrogen to fill the vacuum and glove box.
- Place the glove box over the cool oven such that the elbow is inside.
- Loosen the bolts and remove the plate nuts from the outside while holding onto the elbow
- Remove the elbow, cover the nozzle with Al foil and place elbow inside nitrogen filled glove box. The flow of nitrogen out of the oven should be strong

- Clean out broken glass inside the elbow in the glove box. Using small amounts of methanol, clean out the elbow. This elbow may or may not have rubidium in it, watch for flames. Extinguish flames with the dry nitrogen. Once cleaned and no rubidium remains, pull out of glove box

- With the glove box over the nozzle, pull out the mesh and support cylinder. Drop mesh into mineral oil immediately. Clean the support piece in the glove box with methanol to react any rubidium. Remove support piece from the glove box.

- Remove the nozzle from the vacuum by untightening the bolts. Cover the vacuum end of the oven with Al foil. Put the nozzle in the glove box. React any rubidium with methanol, remove from the glove box

- Move the glove box away from the vacuum system. Cover the surrounding areas with Al foil. Using small metal tools scrape as much rubidium from the cold catcher and surrounding areas into a wide mouth container of mineral oil. Small amounts of methanol can be used on the conflat face to wash the knife edge. Keep the methanol out of the vacuum system to prevent large contamination of the system.

- Check all removed pieces for oil contamination. If any piece is not UHV clean, clean with the appropriate methods (Table 2.1).

- Wrap the new, clean mesh around support

- Put a new gasket in between the nozzle and vacuum chamber; reconnect the nozzle. Place the mesh and support into the nozzle making sure the mesh does not touch the cold cup.

- Put a new gasket in between the nozzle and elbow. Reconnect the elbow.

- Close flood valve
- Turn off the dry nitrogen
- Open block valve to rough pump the vacuum system
- When the pressure $< 10^{-3}$ torr, turn on turbo pump.
- Heat nozzle and elbow over 12 hours to 150 °C

Day two-four

Check the bakeout. The pressure in the oven region should be falling. The bakeout is done when the RGA reads only hydrogen and the pressure $p < 10^{-8}$ torr.

Day five

Once the bakeout is done, the vacuum system is opened again and 5 grams of rubidium is placed in the elbow

Before beginning make sure there is

- UHV cleaned vial of rubidium
- glove box
- hammer
- mineral oil
- Al foil
- Clean copper gasket
- metal dish

To add in the rubidium

- Cool the oven
- Turn off vacuum pumps (turbo-molecular pump)
- Close block valve between turbo-molecular and roughing pump
- Tee the dry nitrogen line and connect one end to the flood valve on the turbo pump and the other into the glove box.
- When the turbo pump turns off, open the turbo pump vent and allow dry nitrogen to fill the vacuum and glove box.
- Place the glove box over the cool oven such that the elbow is inside.
- Loosen the bolts and remove the plate nuts from the outside while holding onto the elbow.
- Remove the elbow, cover the nozzle with Al foil and place elbow inside nitrogen filled glove box. The flow of nitrogen out of the oven should be strong.
- Place rubidium vial on metal dish. With the hammer, remove excess glass without breaking the rubidium filled container, discard glass.
- With the hammer, smash the rubidium on the metal tray until well cracked
- Lift metal tray an scoop glass/rubidium mush into elbow.
- Put clean gasket between nozzle and elbow.
- Re-attach elbow to nozzle
- Close flood valve
- Turn off the dry nitrogen

- Open block valve to rough pump the vacuum system
- When the pressure $< 10^{-3}$ torr, turn on turbo pump.
- Heat nozzle to 60 °C overnight

Day six

Today the mesh needs to be wetted in order for the recirculation to work. Over the day, the bottom of the elbow and nozzle should be raise gently $\sim$ 20 °C/hour keeping a 60°C difference between the nozzle and elbow bottom. A good running temperature $\sim$ 90 °C for the elbow and 150 °C for the nozzle. Once heated measure the atomic flux out of the oven.

Appendix B

Tapered amplifier alignment

This appendix gives a detailed account of how to change the tampered amplifier chip and reshape and realign the beam into the single mode fiber

The tapered amplifier chip (Eagle Yard) amplifies light in a single pass through an active silicon media with $\sim$ 1 A of DC current. In our experiment, 25 mW of light from an injection locked laser at 780 nm seeds the amplifier chip and produces $\sim$ 300 mW of power, which is then shaped, shifted in frequency and inserted into a single mode fiber. The tapered amplifier has two types of emission, spontaneous and stimulated. The spontaneous emission can be at any range of wavelength (700-800 nm) and at 1 A $\sim$ 5 mW in power. This type of emission is used to align the tapered amplifier. The stimulated emission, like any laser, is at the same frequency as the light that is injected.

The output of the taper amplifier is highly anisotropic and astigmatic, having an aspect ratio at the output of 6:1. It is therefore crucial to shape the beam for efficient coupling into the single mode fiber. In the rest of the appendix, I will give some tips and tricks on how to make this process most efficient.

Amplifier installation

The amplifier is mounted on a C-type mount with a small active media on the top. This device is expensive and electrostatically sensitive; all precautions to reduce sparks, i.e. wrist straps and good grounding, should be practiced at all times. The chip mount, described in [13], is home built and comprises of a bar, which heat sinks the chip and acts as an electrical conduit, and two lenses, one on the input, which focus the input light into the active media and one on the output, which focuses the stimulated emission. Each lens is held in a square block that has a hole, exactly the diameter of the lens holder such that the lens holder slip fits into the block. These blocks are glued onto a flex mount, which can be moved to adjust the focus of the lenses.

When mounting the chip, it is imperative that it is in good thermal contact with the mount. The mount is temperature stabilized with a TEC to 21 °C. In order to make good thermal contact a sheet of indium is pressed onto the back of the C mount and then the chip is screwed into the holder. In past designs, we did not use the indium and the tapered amplifier would have a catastrophic failure in which the wire bonds that carry the current to the active media would melt in about 3 months. However, since the implementation of indium in the mount, the tapered amplifier has lasted 2.5 years.

Appendix C

Report on the status of women in the physics department

This document was written in the Fall 2002 semester to access the status of women in the Berkeley physics department. Its motivation began due to a lack of community amongst the women graduate students along with the realization that many most of the graduate students knew at least one or two women who had left the program. This report was presented at a UC Berkeley physics faculty meeting, to the physics department accreditation committee and to the General Accounting Office (GAO) representatives of the United States Congress. Although this chapter does not directly discuss the phenomena of BECs, it show the sociological implications of being a women in the UC Berkeley physics department and discusses relevant issues for women who pursue their Ph.D. in this field.

C.1 Introduction

Over the past semester, the women in the physics department have met in order to discuss the issues that they face in recruitment and retention of women graduate students in the department. The goal of these meetings was to identify if the department had problems with recruitment and/or retention of women graduate students and how to solve these problems if they did exist.

After talking with Anne Takizawa and gaining statistics on the number of women who were admitted to the department vs. the number who accepted the offer (Fig. C.1). We find that there is a significant difference in the amount of women who come to Berkeley versus the amount of men who come to Berkeley.

The women were particularly concerned about the attrition rate of women once they arrived at UC Berkeley. Statistics were gathered on each entering cohort of students: how many women entered in that year and how many women who entered that year left without a Ph.D. These numbers were compared to the same data for men and were found to be significantly higher (Fig. C.2).

Finally, the women were interested in the gender breakdown of physics Ph.D.'s awarded at UC Berkeley compared to the national average and whether there is an upward trend for women in percent of Ph.D.'s granted or if it was stagnant. In Fig. C.3, we see no such increasing trend. Also, we find that UC Berkeley is consistently lower than the national average for granting women Ph.D.'s by about 5% each year.

By looking at the lack of women at the graduate student level, the women wanted to set a goal for gaining women in physics. Last year, in 2002, the Berkeley physics department graduated 100 B.A. in physics, 26 of whom where women. Currently there are 41 women majors out of 202 declared physics majors in the department, 20%. However, there are only 26 women out of 230 or 11% in the graduate program.

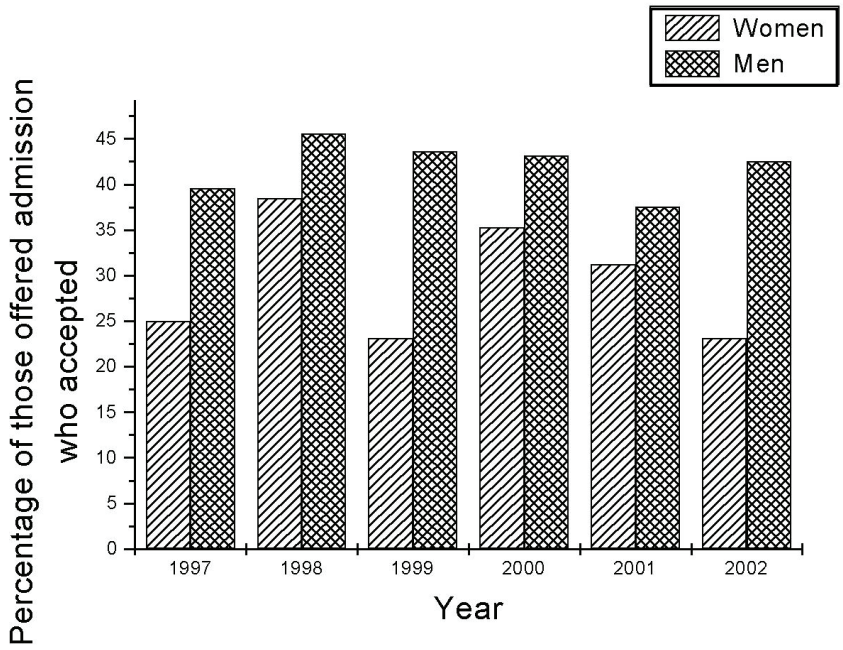

Figure C.1. Percent of those offered admission to UC Berkeley who accepted. A comparison by gender of the ability of UC Berkeley to recruit graduate students over six years. Over this time, the percentage of men who choose to accept the Berkeley offer far exceeds the percentage of women. Some factors that may affect this are overall environment, financial offers, and overall recruitment effort.

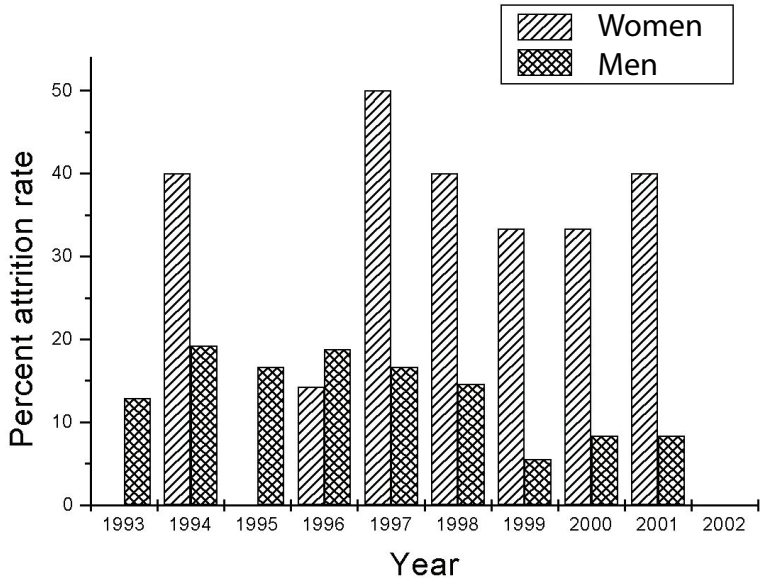

Figure C.2. Percent of students in an entering class, broken down by gender, who left without a Ph.D.

They felt that the number of women graduate students should be as a first, minimum goal, equal to the percentage of women undergraduates.

What follows is a short list identifying basic themes the women graduate students feel are causing the above trend of recruitment and retention problems in the physics department. The first section identifies the positive aspects of the department. The next section looks at the areas that need improvement and finally, the last section discusses many ways to improve the physics department, not just for women, but for every member. The following is not complete, but is a beginning to achieve the goals set forth in the previous paragraph.

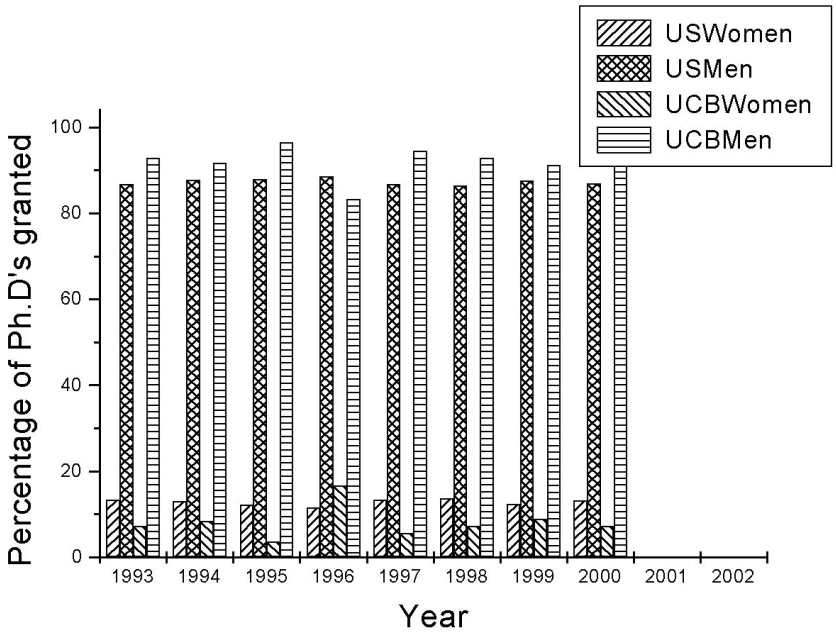

Figure C.3. Comparison of the number of Ph.D.'s granted to women and men at in physics at UC Berkeley vs. nationally. As can be seen, UC Berkeley's graduating class has consistently fewer women than the national average. Source AIP enrollment and degree reports.

C.2 Positive aspects in the physics department

The women felt that there were many positive aspects in the physics department that created a rich and supportive atmosphere for their education. These areas are

- TA offices
- Staff
- Machine shop
- Electronics shop

During the first year, most students found that the TA offices were the center of camaraderie. The office provides a place to gather, talk, discuss, do homework, and have a connection to the department. The staff, especially Anne, Donna and Claudia, was recognized as being a large positive part of the women's every day. They felt that they cared about the progress of the students and that they would make an extra effort to help out when they could. Anne was particularly mentioned on how hard she worked in order to get students tutors for the prelims.

The two technical shops in the department were also mentioned as important supportive tools to the women. Joseph, the machinist in the graduate student shop, was commended for his ability to help with designs and answer questions. His machining class is seen as a big benefit to many women who have little or no machining background. The class allows for an intensive catch up period so that they can succeed in their own experiments. The rest of the shop was also considered a large asset to many of the women as a good resource to guide in the development of large machinery in their labs. The electronics shop was given high marks. John Davis was seen as an integral part in many experimental designs. The students felt that he treated them with respect and was able to impart a large amount of electronics knowledge to

the students. His electronics course during the summer gained the highest marks for usefulness and knowledge gained.

C.3 Areas for improvement

At the women's meeting, four main categories were discussed, which were seen as needing improvement. These areas are:

- Lack of women faculty and women graduate students
- Advising
- Prelims
- Professional Development

C.3.1 Women Faculty and graduate Students

The physics department (both at UC Berkeley and nationally) does not have a critical mass of women. The students felt that this was the most pressing issue. The lack of critical mass makes many women feel invisible and trivialized. Their concerns are often overlooked and not addressed.

The lack of women at the graduate level leads to a feeling of loneliness. With only one or two women around in the TA office, women find that the topics of conversations in the first year offices become inappropriate for a workplace environment. With a larger visibility of women in the offices, many of these issues would not surface.

The lack of women at the faculty level leaves a large void in the department for role models for the women graduate students. They feel that this lack of women professors discourages them from think about academia as a career. It is a message

to the women that they are unable to make it into the professorial role and many just leave before achieving a Ph.D. or soon after gaining one.

Along the same lines of gaining more women faculty and students, it has been noticed the lack of women colloquia speakers and honored lectureships (i.e. Segre or Oppenheimer lecturer). Women who speak in front of the department change perceptions of a qualified scientist. They allow for networking with the entire faculty and give role models to female students.

C.3.2 Advising

The second issue that the students talked about at length was the lack of advising from faculty in the department. This has two broad areas: 1) advising during the first one to two years before gaining a research advisor and 2) guidance from a research advisor.

The first one or two years of graduate school can be difficult. This is the time when most women decide that they do not want their Ph.D. Most women do not remember who their incoming "advisor" was nor can they remember ever talking with him/her. They felt that they had to make choices on classes (whether to jump into the 221 and 209 classes or 137 and 110), which they had no good basis to make. They also felt that they had no person to talk to about different physics field's career paths that subsequently went along with these choices. Also, many women felt that they never were advised on the option of going into theory, and that this advice could have changed the outcome of many perceptions of physics.

The second area, lack of guidance from a research advisor comes in two distinct forms, 1) actual technical advising and 2) completion of the Ph.D. The women felt that technical advising, i.e. explaining how a lock-in amplifier works, when they began in their labs was severely lacking. Many felt that they were often thrown into

a lab and told to get a particular piece of equipment to work and given no other guidance than this. This state of utter confusion left many students feeling stupid and questioning their ability to be good scientists. In large collaborations, many students feel that they get lost and that their development as students is a far second to gaining results. The second part of advising for students as they traveled closer to graduation was the lack of advice for completion. Many women felt that the time to finishing the experiment Ph.D. is growing due to the lack of advising during the last years when they are ever so close, but not done, with their project. This is one of the major drawbacks women who have B.A. see when they enter the field. They feel that this process is too lengthy and chose another life path.

C.3.3 Prelims

The prelims, as always, are a controversial subject in the department. The women felt that the actual outcome of the prelims do not mesh with the stated goals of the exam. When entering as a first year, it is explained that the prelims are an exam that tests your basic knowledge of general physics. That the exam will cover undergraduate physics. Many tests go beyond the scope of undergraduate physics. Also, it was felt when results were reported that the ranking of students within the class was humiliating and unnecessary. The reality of the exam is that it caused most students to lower their self-esteem and question their ability to do physics. This is a major reason why many women decide not to enroll at Berkeley and why many leave.

C.3.4 Professional development

The last area that the women discussed was professional development. One of the major issues that women see as a deterrent from physics is the lack of job opportunities in their future. There are few opportunities to gain insight on how to apply for a job,

learn how to create their own research project needed to give successful job talks and how to choose the most successful post-doc or job that will propel them to success.

C.4 Ideas to improve the atmosphere in the physics department

After identifying many issues that were important to the graduate women in the department, the students brainstormed many ideas on how to improve the environment with the goals of recruiting and retaining more women. The following is a short list of ideas that were brought forward.

C.4.1 Hire more women faculty

Although this is a simple statement to write, it is more difficult to complete. There were some good ideas presented to help both find and recruit women. First, there are many women specific job-posting sites that can be used to target qualified women. WIPHYS, a posting site from the committee for the status on women in physics by the APS is one place to start. This can be found on their web site or information about them can be gained by emailing women@aps.org.

The hiring process should also be made more transparent in the department. One-way to help recruit women candidates is to allow them to meet with other women faculty and, due to the lack of women faculty with the women graduate students. This allows the prospective candidate a feeling that there is a support network in the department and that they will not be isolated. Also, the subcommittees that review applications should include students (not only women) such that other views can be heard when deciding whom to bring as a

final candidate to the entire faculty. Other ways that can be used to increase women faculty can be found in an article written by Howard Georgi of Harvard at http://schwinger.harvard.edu/ georgi/women/backpage.htm, which is an article found in the January 2000 Edition of the APS News Online.

C.4.2 Invite women as colloquia speakers and distinguished lecturers

The invitation of women as colloquia speakers can be a goal of the department. The APS compiles a speakers list of women by state and field on their website. Departments also qualify for $500 reimbursement for travel expenses for one speaker if more than two speakers are invited within one academic year.

Recruiting women to give talks in the field specific seminars would also gain visibility for women in that field. Women post-docs could be invited early in their work as a first introduction with the thought of recruitment in later years.

Finally, it is important to invite women to give the distinguished lectures (i.e. Regents, Oppenhiemer, Segre, Hitchcock). These lectureships are highly thought of and introduce the public to a new image of outstanding scientists being women.

Some other women who have been suggested for potential colloquia, lecture series or field specific seminars are: Marjorie Olmstead (University of Washington), Margaret Murname (JILA), Shirley Chiang (Davis), Persis Drell (Cornell), Meg Urry (head of the IUPAP Conference) and Cherry Murray (winner of the Marie Geoppert Mayer award).

C.4.3 Institute a comprehensive advising system in the first years

The advising system to incoming graduate students needs to be improved. Instead of each student choosing their own advisor, each student should be assigned to an advisor who is familiar with the different options for the first years in the department. There should be an initial advising session where the student and the professor examine the past work of the student and decide if they are prepared for the first year graduate classes. The overwhelming opinion about being told that the student is unprepared is that they would rather be advised to take the undergraduate class and succeed then drop out and fail by being pushed beyond what they are prepared for by their undergraduate classes. The advisor should also be prepared to talk to the student about interests and different research options trying to help the student refine their interests and guide them onto the path that will make them most successful.

C.4.4 Give faculty research advisors the ability to share good advising techniques

Encourage faculty to advise their students both in the laboratory and in career goals. Also, have department oversight on lengths of Ph.D.'s and identify ways to shorten the process without jeopardizing graduate education.

C.4.5 Allow students to take the machine shop course and electronics course during their first year

By allowing first year students without an advisor to gain valuable experimental knowledge before going into an intense laboratory setting, the student will gain self esteem and be better trained and seen as a more valuable asset to the hiring professor.

C.4.6 Prelims

The prelim exam should have a stated goal and the test should then meet that goal. This can be achieved by allowing two students to sit on the exam committee and access if the exam really covers undergraduate course work or is outside the scope of the stated goals. Also, when students receive their scores, it is not necessary to rank the student against the rest of the class. The students score, mean, standard deviation, and whether they passed or not is the only information that is needed.

C.4.7 Professional development

There are two separate ways to increase the professional development of graduate students as a whole. The first way could be to have and publicize books in the physics library on career building, making choices between academia and industry, how to develop a CV, how to balance science and family, and other such topics.

The second very popular suggestion was to bring in panels of speakers to talk about many issues. This has been done in a limited scope in the last couple of years, but there could be more. For example, a panel on how to bargain for the best post-doc would be useful. Also, a series on how to start your own research group/set up a laboratory would take some of the mystery out of joining academia and encourage more women to go down this path. Other useful topics could include: How to get the

best deal as an assistant professor/staff scientist/industry worker (a.k.a. how to get the most lab space, set up, benefits, salary), how to create your own research path and development into a PI, and how to network.

C.4.8 Graduate student lounge

One of the most enjoyable parts of the physics department is having TA offices the first year. However, after that year, many graduate students are spread around Berkeley, either at LBNL, Space Sciences, Birge, Le Conte, or other buildings on campus. It is necessary to have a full graduate student lounge. The existing graduate student lounge is not used. It is uncomfortable, has no window, dreary, dirty and most students don't know where it is or don't have keys. However, a clean, well-lit room that encourages socialization and a feeling of comfort would allow graduate students, especially ones without an office on campus to have a place to be. This lounge should have a clean refrigerator, microwave, window, tables, chairs, and a couch (although a couch too small to sleep on). This graduate student lounge is even more important now since the SURGE retrofit moved the TA offices out of LeConte therefore making the graduate students more spread out.

C.4.9 Women's bathrooms

There is a lack of women's bathrooms in the Birge/LeConte physics complex. Birge is lacking a women's restroom on the 3rd floor and LeConte has no restrooms for women on the ground or 2nd floor. However, there are men's restrooms on every floor. This is important to point out especially when the new physics building is designed, there needs to be equal men's and women's bathrooms.

C.5 Conclusion

The above discussion about how to improve the physics department, increase recruitment and decrease attrition is not completely inclusive. This should be considered a working list and a dialogue between both faculty and students should continue.

Bibliography

[1] P. Kapitza. Viscosity of liquid helium below the λ-point. *Nature*, 141:74, 1938.

[2] D. D. Osheroff, R. C. Richardson, and D. M. Lee. Evidence for a new phase of solid he3. *Phys. Rev. Lett.*, 28:885, 1972.

[3] J. L. Lin and J. P. Wolfe. Bose-einstein condensation of paraexcitons in stressed cu2o. *Phys. Rev. Lett.*, 71:1222, 1993.

[4] S. Demokritov, V. Demidov, O. Dzyapko, G. Melkov, A. Serga, B. Hillebrands, and A. Slavin. Bose-einstein condensation of quasi-equilibrium magnons at room temperature under pumping. *Nature*, 443:430, 2006.

[5] J. Kasprzak, M. Richard, S. Kundermann, A. Bass, J. Jeambrun, J. Keeling, F. M. Marchetti, M. Szymaska, R Andr, J. Staehli, V. Savona, P. Littlewood, B Deveaud, and L. Dang. Bose-einstein condensation of exciton polaritons. *Nature*, 443:409, 2006.

[6] M. H. Anderson, J. R. Ensher, M. R. Matthews, C. E. Wieman, and E. A. Cornell. Observation of bose-einstein condensation in a dilute atomic vapor. *Science*, 269:198, 1995.

[7] K. B. Davis, M.-O. Mewes, M. R. Andrews, N. J. van Druten, D. S. Durfee, D. M. Kurn, and W. Ketterle. Bose-einstein condensation in a gas of sodium atoms. *Phys. Rev. Lett.*, 75:3969, 1995.

[8] F. Dalfovo, S. Giorgini, L. P. Pitaevskii, and S. Stringari. Theory of bose–einstein condensation in trapped gases. *Rev. Mod. Phys.*, 71(3):463, 1999.

[9] S. N. Bose. Plancks gesetz und lichtquantenhypothese. *Zeitschrift für Physik*, 26:178, 1924.

[10] A. Einstein. Quantentheorie des einatomigen idealen gases. *Sitzungsberichte der preussischen Akademie der Wissenschaften*, (Bericht 22):261–267, 1924.

[11] T.-L. Ho. Spinor bose condensates in optical traps. *Phys. Rev. Lett.*, 81:742, 1998.

[12] M. G. Moore and P. Meystre. Theory of superradiant scattering of laser light from bose-einstein condensates. *Phys. Rev. Lett.*, 83:5202, 1999.

[13] J. Higbie. *Thesis*. PhD thesis, University of California, Berkeley, 2005.

[14] J. Dalibard and C. Cohen-Tannoudji. Laser cooling below the doppler limit by polarization gradients: simple theoretical models. *J. Opt. Sci. Am. B*, 6:2023, 1989.

[15] D. E. Pritchard. Cooling neutral atoms in a magnetic trap for precision spectroscopy. *Phys. Rev. Lett.*, 51:1336, 1983.

[16] W. Ketterle and N. J. van Druten. Evaporative cooling of trapped atoms. In B. Bederson and H. Walther, editors, *Advances in Atomic, Molecular, and Optical Physics*, volume 37, pages 181 – 236. Academic Press, San Diego, 1996.

[17] Melissa Lambropoulos and S. E. Moody. Design of a three-stage alkali beam source. *Review of Scientific Instruments*, 48(2):131–134, 1977.

[18] R. D. Swenumson and U. Even. Continuous flow reflux oven as the source of an effusive molecular cs beam. *Review of Scientific Instruments*, 52(4):559–561, 1981.

[19] L. V. Hau, J. A. Golovchenko, and M. M. Burns. A new atomic beam source: the "candlestick". *Reviews of Scientific Instruments*, 65:3746, 1994.

[20] M. R. Walkiewicz, P. J. Fox, and R. E. Scholten. Candlestick rubidium beam source. *Review of Scientific Instruments*, 71:3342, 2000.

[21] G. M. Grover, T. P. Cotter, and G. F. Erickson. Structures of very high thermal conductance. *Journal of Applied Physics*, 35(6):1990–1991, 1964.

[22] V. Savalli. *Etude haute rsolution de la spcularit d'un miroir atomique onde vanescente*. Ph.d., Universit Pierre et Marie Curie, 2000.

[23] Kevin L. Moore, Thomas P. Purdy, Kater W. Murch, Sabrina Leslie, Subhadeep Gupta, and Dan M. Stamper-Kurn. Collimated, single-pass atom source from a pulsed alkali metal dispenser for laser-cooling experiments. *Review of Scientific Instruments*, 76(2):023106, 2005.

[24] Outgassing data for selecting spacecraft materials online. http://outgassing.nasa.gov/, 2006.

[25] Y. Tito Sasaki. A survey of vacuum material cleaning procedures: A subcommittee report of the american vacuum society recommended practices committee. *Journal of Vacuum Science and Technology A: Vacuum, Surfaces, and Films*, 9(3):2025–2035, 1991.

[26] A. Ashkin. Acceleration and trapping of particles by radiation pressure. *Phys. Rev. Lett.*, 24:156–159, 1970.

[27] D. M. Stamper-Kurn, M. R. Andrews, A. P. Chikkatur, S. Inouye, H.-J. Miesner, J. Stenger, and W. Ketterle. Optical confinement of a bose-einstein condensate. *Phys. Rev. Lett.*, 80:2072–2075, 1998.

[28] D. M. Stamper-Kurn and W. Ketterle. Spinor condensates and light scattering from bose-einstein condensates. In R. Kaiser, C. Westbrook, and F. David, editors, *Coherent Matter Waves*, pages 137 – 218. Springer-Verlag, New York, 2001.

[29] C. A. Regal, M. Greiner, and D. S. Jin. Observation of resonance condensation of fermionic atom pairs. *Phys. Rev. Lett.*, 92:040403, 2004.

[30] M. W. Zwierlein, C. A. Stan, C. H. Schunck, S. M. F. Raupach, A. J. Kerman, and W. Ketterle. Condensation of pairs of fermionic atoms near a feshbach resonance. *Phys. Rev. Lett.*, 92:120403, 2004.

[31] I. Bloch, T. W. Hänsch, and T. Esslinger. Measurement of the spatial coherence of a trapped bose gas at the phase transition. *Nature*, 403:166, 1999.

[32] M. D. Barrett, J. A. Sauer, and M. S. Chapman. All-optical formation of an atomic bose-einstein condensate. *Phys. Rev. Lett.*, 87:010404, 2001.

[33] R. Grimm, M. Weidemüller, and Y. Ovchinnikov. Optical dipole traps for neutral atoms. Technical report, 1999.

[34] K. W. Madison, F. Chevy, W. Wohlleben, and J. Dalibard. Vortex formation in a stirred bose-einstein condensate. *Phys. Rev. Lett.*, 84:806, 2000.

[35] D. M. Stamper-Kurn. *Peeking and poking at a new quantum fluid: studies of gaseous Bose-Einstein condensates in magnetic and optical traps*. Ph.d., Massachusetts Institute of Technology, 2000.

[36] H.-J. Miesner, D. M. Stamper-Kurn, M. R. Andrews, D. S. Durfee, S. Inouye, and W. Ketterle. Bosonic stimulation in the formation of a bose-einstein condensate. *Science*, 279:1005–1007, 1998.

[37] D. M. Stamper-Kurn, H.-J. Miesner, S. Inouye, M. R. Andrews, and W. Ketterle. Collisionless and hydrodynamic excitations of a bose-einstein condensate. *Phys. Rev. Lett.*, 81:500–503, 1998.

[38] Priceton Instruments. Key considerations for uv and nir applications nir. website, Princeton Instruments, 2006.

[39] W. Ketterle, D. S. Durfee, and D. M. Stamper-Kurn. Making, probing and understanding bose-einstein condensates. In M. Inguscio, S. Stringari, and C.E. Wieman, editors, *Bose-Einstein condensation in atomic gases*, Proceedings of the International School of Physics "Enrico Fermi," Course CXL, pages 67–176. IOS Press, Amsterdam, 1999.

[40] L. E. Sadler, J. M. Higbie, S. R. Leslie, M. Vengalatorre, and D. M. Stamper-Kurn.

[41] F. Zernike. *Z. Tech. Phys*, 16:454, 1935.

[42] J. M. Higbie, L. E. Sadler, S. Inouye, A. P. Chikkatur, S. R. Leslie, K. L. Moore, V. Savalli, and D. M. Stamper-Kurn. Direct, non-destructive imaging of magnetization in a spin-1 bose gas. *Phys. Rev. Lett.*, 95:050401, 2005.

[43] I. Carusotto and E. J. Mueller. Imaging of spinor gases. *J. Phys. B*, 37:S115, 2004.

[44] W. H. Zurek, U. Dorner, and P. Zoller. Dynamics of a quantum phase transition. *Phys. Rev. Lett.*, 95:105701–4, 2005.

[45] T. W. B. Kibble. Topology of cosmic domains and strings. *Journal of Physics A: Mathematics and General*, 9:1387 – 1398, 1976.

[46] W. H. Zurek. Cosmological experiments in superfluid helium? *Nature*, 317:505 – 508, 1985.

[47] R. H. Dicke. Coherence in spontaneous radiation processes. *Phys. Rev.*, 93(1):99, 1954.

[48] Reinhold Florian, Lothar O. Schwan, and Dankward Schmid. Time-resolving experiments on dicke superfluorescence of o_2^- centers in kcl. two-color superfluorescence. *Phys. Rev. A*, 29(5):2709–2715, May 1984.

[49] M. Dreher, E. Takahashi, J. Meyer ter Vehn, and K.-J. Witte. Observation of superradiant amplification of ultrashort laser pulses in a plasma. *Phys. Rev. Lett.*, 93:095001, 2004.

[50] N. Skribanowitz, I. P. Herman, J. C. MacGillivray, and M. S. Feld. Observation of dicke superradiance in optically pumped hf gas. *Phys. Rev. Lett.*, 30(8):309–312, Feb 1973.

[51] S. Inouye, A. P. Chikkatur, D. M. Stamper-Kurn, J. Stenger, and W. Ketterle. Superradiant rayleigh scattering from a bose–einstein condensate. *Science*, 285(July 23):571, 1999.

[52] D. Schneble, G. K. Campbell, E. W. Streed, M. Boyd, D. E. Pritchard, and W. Ketterle. Raman amplification of matter waves. *Phys. Rev. A*, 69:041601(R), 2004.

[53] Dominik Schneble, Yoshio Torii, Micah Boyd, Erik W. Streed, David E. Pritchard, and Wolfgang Ketterle. The Onset of Matter-Wave Amplification in a Superradiant Bose-Einstein Condensate. *Science*, 300(5618):475–478, 2003.

[54] Y. Yoshikawa, Y. Torii, and T. Kuga. Superradiant light scattering from thermal atomic vapors. *Phys. Rev. Lett.*, 94:083602, 2005.

[55] J. C. MacGillivray and M. S. Feld. Theory of superradiance in an extended, optically thick medium. *Phys. Rev. A*, 14:1169–1189, 1976.

[56] H. Uys and P. Meystre, October 2006. arXiv:cond-mat/0602343 v3 17 October 2006.

[57] A. C. Chikkatur, A. Görlitz, D. M. Stamper-Kurn, S. Inouye, S. Gupta, and W. Ketterle. Suppression and enhancement of impurity scattering in a bose-einstein condensate. *Phys. Rev. Lett.*, 85:483, 2000.

[58] E. Noether. Abstrakter aufbau der idealtheorie in algebraischen zahl- und funktionenkrpern. *Mathematische Annalen*, 96:26, 1905.

[59] E. A. Cornell and C. E. Wieman. Nobel lecture: Bose-einstein condensation in a dilute gas, the first 70 years and some recent experiments. *Rev. Mod. Phys.*, 74(3):875–893, 2002.

[60] Wolfgang Ketterle. Nobel lecture: When atoms behave as waves: Bose-einstein condensation and the atom laser. *Rev. Mod. Phys.*, 74(4):1131–1151, 2002.

[61] C. V. Heer. Feasibility of containment of quantum magnetic dipoles. *The Review of Scientific Instruments*, 34:532, 1963.

[62] T. Ohmi and K. Machida. Bose-einstein condensation with internal degrees of freedom in alkali atom gases. *J. Phys. Soc. Jpn.*, 67:1822, 1998.

[63] C. J. Myatt, E. A. Burt, R. W. Ghrist, E. A. Cornell, and C. E. Wieman. Production of two overlapping bose-einstein condensates by sympathetic cooling. *Phys. Rev. Lett.*, 78:586, 1997.

[64] D. S. Hall, M. R. Matthews, C. E. Wieman, and E. A. Cornell. Measurements of relative phase in two-component bose-einstein condensates. *Phys. Rev. Lett.*, 81:1543, 1998.

[65] H.-J. Miesner, D. M. Stamper-Kurn, J. Stenger, S. Inouye, A. P. Chikktur, and W. Ketterle. Observation of metastable states in spinor bose-einstein condensates. *Phys. Rev. Lett.*, 82:2228–2231, 1999.

[66] J. Stenger, S. Inouye, D. M. Stamper-Kurn, H.-J. Miesner, A. P. Chikkatur, and W. Ketterle. Spin domains in ground state spinor bose-einstein condensates. *Nature*, 396:345, 1998.

[67] D. M. Stamper-Kurn, H.-J. Miesner, A. P. Chikkatur, S. Inouye, J. Stenger, and W. Ketterle. Quantum tunneling across spin domains in a bose-einstein condensate. *Phys. Rev. Lett.*, 83:661, 1999.

[68] M.-S. Chang, C. D. Hamley, M. D. Barrett, J. A. Sauer, K. M. Fortier, W. Zhang, L. You, and M. S. Chapman. Observation of spinor dynamics in optically trapped rb bose-einstein condensates. *Phys. Rev. Lett.*, 92:140403, 2004.

[69] H. Schmaljohann, M. Erhard, J. Kronjäger, M. Kottke, S. v. Staa, L. Cacciapuoti, J. J. Arlt, K. Bongs, and K. Sengstock. Dynamics of f = 2 spinor bose-einstein condensates. *Phys. Rev. Lett.*, 92:040402, 2004.

[70] Subroto Mukerjee, Cenke Xu, and J. E. Moore. Topological defects and the superfluid transition of the $s = 1$ spinor condensate in two dimensions. *Phys. Rev. Lett.*, 97(12):120406, 2006.

[71] L. E. Sadler, J. M. Higbie, S. R. Leslie, M. Vengalatorre, and D.M. Stamper-Kurn. Spontaneous symmetry breaking in a quenched ferromagnetic spinor bose-einstein condensate. *Nature*, 404:256, 2000.

[72] I. Chuang, R. Durrer, N. Turok, and B. Yurke. Cosmology in the laboratory: defect dynamics in liquid crystals. *Science*, 251:1336 – 1342, 1991.

[73] P. C. Hendry et al. Generation of defects in superfluid ^{4} he as an analogue of the formation of cosmic strings. *Nature*, 368:315 – 317, 1994.

[74] V. M. H. Ruutu et al. Vortex formation in neutron-irradiated superfluid he-3 as an analogue of cosmological defect formation. *Nature*, 382:334 – 336, 1996.

[75] C. Bauerle et al. Laboratory simulation of cosmic string formation in the early universe using superfluid he-3. *Nature*, 382:332 – 334, 1996.

[76] T. Isoshima, K. Machida, and T. Ohmi. Quantum vortex in a spinor bose-einstein condensate. *Journal of the Physical Society of Japan*, 70:1604 – 1610, 2001.

[77] N. D. Mermin and T.-L. Ho. Circulation and angular momentum in the a phase of superfluid helium-3. *Phys. Rev. Lett.*, 36:594 – 597, 1976.

[78] H. Saito, Y. Kawaguchi, and M. Ueda. Breaking of chiral symmetry and spontaneous rotation in a spinor bose-einstein condensate. *Phys. Rev. Lett.*, 96:065302–4, 2006.